

Lecture Notes on High Energy Cosmic Rays

prepared for the 17.th Jyväskylä Summer School, August 2007

M. Kachelrieß

Institutt for fysikk, NTNU, Trondheim, Norway

Abstract: I give a concise introduction into high energy cosmic ray physics, including also few related aspects of high energy gamma-ray and neutrino astrophysics. The main emphasis is placed on astrophysical questions, and the level of the presentation is kept basic.

Contents

1	Introduction	5
1.1	Preludes	5
1.2	Historical remarks	7
2	Basic notations of particle physics	9
2.1	Relativistic kinematic and cross sections	9
2.1.1	Kinematics	9
2.1.2	Cross section, interaction depth, and slant depth	10
2.2	Particles and interactions	11
2.2.1	Our particle inventory	11
2.2.2	Comparison of electromagnetic, weak and strong interactions	11
2.3	Exercises	13
3	Galactic cosmic rays	15
3.1	Basic observations	15
3.1.1	Cosmic ray intensity and composition	15
3.1.2	Anisotropies and deflections in regular magnetic fields	17
3.2	Propagation of Galactic cosmic rays	20
3.3	Exercises	25
4	Sources and acceleration of high energy cosmic rays	27
4.1	Sources of high energy cosmic rays	27
4.1.1	General arguments	27
4.1.2	Specific sources	28
4.2	Acceleration of cosmic rays	32
4.2.1	Second order Fermi acceleration	32
4.2.2	Shock or first order Fermi acceleration	33
5	Gamma-ray astronomy	38
5.1	Experiments and detection methods	38
5.2	Electromagnetic processes	38
5.2.1	Synchrotron radiation	38
5.2.2	(Inverse) Compton scattering	40
5.3	Hadronic processes	40
5.4	Source models	41
5.5	Electromagnetic cascades	42
5.5.1	Cascades in the atmosphere	43
5.5.2	Cascades on diffuse photon backgrounds	44
5.6	Exercises	45

6	Extragalactic cosmic rays	47
6.1	Propagation of extragalactic particles	47
6.1.1	Energy losses of protons and nuclei	47
6.1.2	Galactic and extragalactic magnetic fields	49
6.2	The dip and the Galactic–extragalactic transition	50
6.3	Extensive air showers initiated by hadrons	51
6.4	Astronomy with charged particles	53
6.4.1	Clustering on medium and small scales	55
6.4.2	Correlations with astrophysical sources	57
7	High energy neutrino astrophysics	58
7.1	Connecting neutrino, γ -ray and cosmic ray fluxes	58
7.2	Neutrino interactions, masses and mixing	61
7.3	Atmospheric neutrino oscillations	64
7.4	High energy neutrino scattering	65
7.5	Astrophysical sources of high energy neutrinos	66
7.6	Exercises	69
8	Cosmic rays as tool for particle physics	70
8.1	Air shower and new particle physics	70
8.2	Relics from the early universe as cosmic rays sources	71
8.2.1	WIMPs as thermal relics	72
8.2.2	SHDM as inflationary relic	74
8.3	Indirect detection of dark matter	74
8.3.1	Dark matter in the Galactic halo	74
8.3.2	Neutrinos from dark matter annihilations in the Sun and the Earth .	76
8.4	Summary of possible and suggested signals for DM	77
	Epilogue	79

1 Introduction

1.1 Preludes

What do we want to discuss?

The term cosmic rays may be defined either as all radiation consisting of relativistic particles impinging on the Earth’s atmosphere from outer space or, more narrowly, including only charged particles. We shall follow generally the latter definition, but discuss also high energy gamma rays and neutrinos, since (i) they can be created as secondaries of high energy cosmic rays and (ii) they may help us to learn more about the charged component and their sources (“multi-messenger approach”). The qualification high energy (or relativistic) means that we do not consider cosmic rays below a few GeV that may be produced or are influenced by the Sun and its wind. The cosmic ray spectrum, a nearly featureless power-law extending over eleven decades in energy up to a few $\times 10^{20}$ eV, is shown in Fig. 1.1.

We cover mainly astrophysical aspects (What are the sources? How do they accelerate cosmic rays? What happens during the journey of cosmic rays to the Earth?), but discuss also briefly their interactions in the atmosphere and the experimental methods used to detect them. In the final chapter we review connections between cosmic ray physics and searches for physics beyond the standard model.

The level of the presentation is as basic as possible, preferring “back on the envelope calculations”, and the material covered corresponds roughly to 20 hours of lectures.

Where are we?

Our standard length unit is the parsec, the distance from the Earth to a star that has a parallax¹ of one arcsecond. Since one arcsecond is $1/(360 \times 60 \times 60) = 1/206265$ fraction of 2π , a parsec corresponds to $206,265 \text{ AU} = 3.086 \times 10^{18} \text{ cm} = 3.26 \text{ yr} = 1 \text{ pc}$.

A schematic picture of our home galaxy, the Milky Way, is shown in Fig. 1.2. Most stars are concentrated in the galactic disc of height $h \approx 300 \text{ pc}$ in the form of spiral arms. The disc is filled with warm atomic gas that consists to 90% of H and to 10% of He and has an average density $n \sim 1/\text{cm}^3$. It contains also an ordered magnetic field with strength $B \sim 3\mu\text{G}$. The energy when the Larmor radius

$$R_L = \frac{cp}{ZeB} \approx 100 \text{ pc} \frac{3\mu\text{G}}{B} \frac{E}{Z \times 10^{18} \text{ eV}} \quad (1.1)$$

of a particle with charge Ze and momentum p equals the height of the Galactic disc marks approximately the transition between diffusive and rectilinear propagation of cosmic rays. We can hope to perform “charged-particle astronomy” only for energies well above this transition.

¹Relatively nearby stars are seen at slightly different positions on the celestial sphere (i.e. the background of stars that are “infinitely” far away) as the Earth moves around the Sun. Half of this angular difference is called the parallax angle or simply the parallax p . Thus $p \approx \tan p = \text{AU}/d$, where 1 AU denotes the mean distance between the Earth and the Sun.

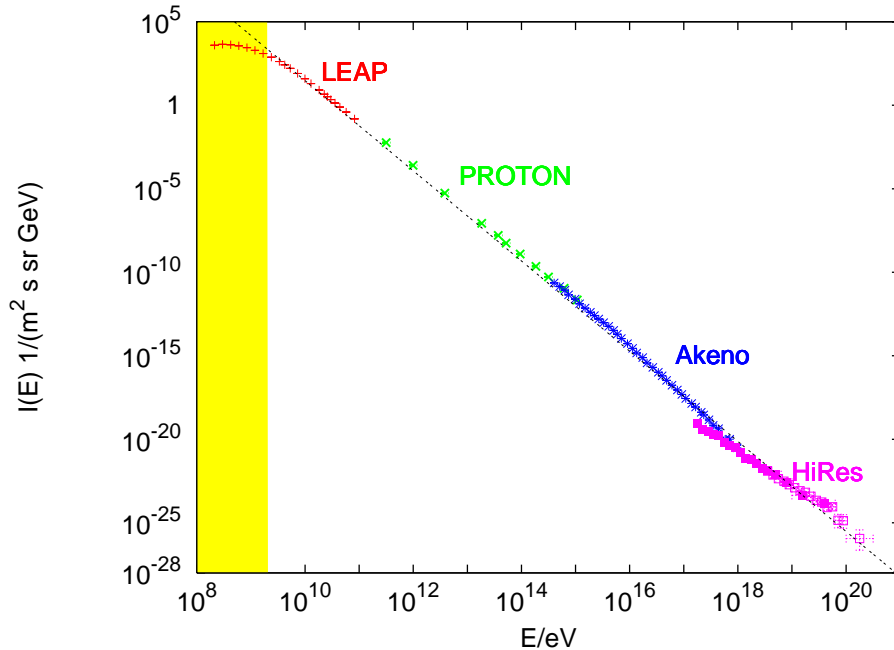


Figure 1.1: The cosmic ray spectrum $I(E)$ as function of kinetic energy E , compiled using results from the LEAP, proton, Akeno, and HiRes experiments [1]. The energy region influenced by the Sun is marked yellow and an $1/E^{2.7}$ power-law is also shown.

This is one of the reasons why we are especially interested in cosmic rays of the highest energies.

A halo extends with $n \sim 0.01/\text{cm}^3$ and a turbulent magnetic field probably up to distances $\sim (10 - 15)$ kpc above the disc. The average strength of this turbulent magnetic field is not well restricted and may reach up to $B \lesssim 10 \mu\text{G}$. The whole visible part of the galaxy is embedded in a much larger dark matter halo, which comprises 90% of the total mass of the Milky Way. The center of the Milky Way contains, as probably most other galaxies, a supermassive black hole (SMBH) with mass $\sim 10^6 M_\odot$.

The Milky Way is a member of the Local Group, a rather small cluster of galaxies with the Andromeda galaxy as the other prominent member. Its diameter is ~ 2 Mpc. The distance to the nearest galaxy cluster, the Virgo cluster, is 18 Mpc, i.e. approximately equal to the mean free path of cosmic rays with the highest observed energies, $E \sim 10^{20}$ eV.

A naive estimate for the size R of the observable Universe can be obtained from the observed recession velocity $v = H_0 d$ of galaxies at the distance d . Using for the Hubble parameter $H_0 = 70 \text{ km s}^{-1} \text{ Mpc}^{-1}$, it follows $R = c/H_0 \sim 4300$ Mpc. For comparison, the cosmic ray horizon reaches Gpc scale at $E = 10^{19}$ eV.

We shall use mostly natural units with $\hbar = c = k_B = 1$, but keep often explicitly the speed of light c in formulas within a more astrophysical context.

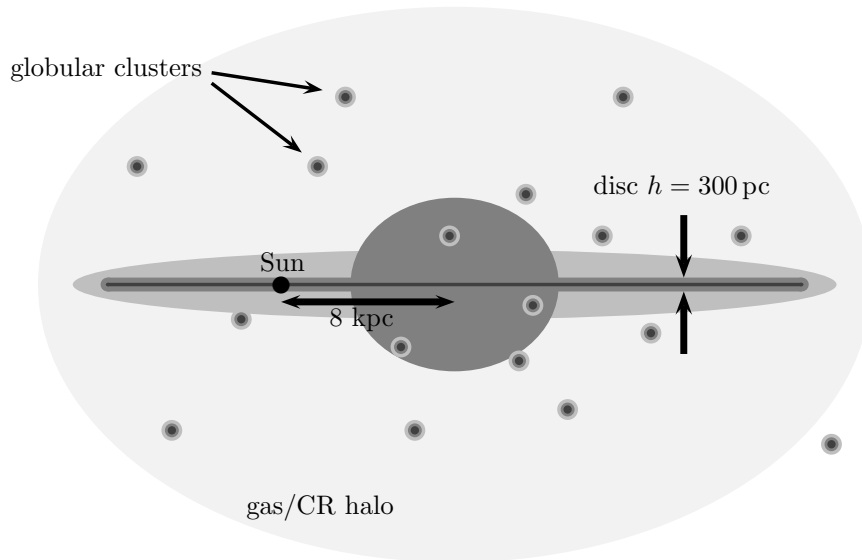


Figure 1.2: Schematic picture of the Milky Way with a gas and dust disc, an extended halo of gas and cosmic rays, surrounded by globular clusters. Everything is immersed in a halo of dark matter.

1.2 Historical remarks

- 1912: Victor Hess discovered on a balloon flight that ionizing radiation increases with altitude. As he wrote “The results of the present observations are most easily explained by the assumption that radiation with very high penetrating power enters the atmosphere from above; even in its lower layers, this radiation produces part of the ionization observed in closed vessels. . . Since there was neither a decrease at night or during solar eclipse, the Sun can hardly be considered as the source. . .” [2].
- 1929: Skobelzyn observed first cosmic rays with a cloud chamber. Bothe and Kolhörster showed that the tracks are curved by a magnetic field. This proved that the observed cosmic rays on ground are charged particles—now we know that these are mainly muons produced as secondaries in cosmic ray interactions in the higher atmosphere.
- 28/29: Clay observed the “latitude effect”: The cosmic ray intensity depends on the (geomagnetic) latitude. Bothe and Kolhörster provided first the correct interpretation of this effect as an anisotropy induced by the magnetic field of the Earth, providing in turn evidence that (the primary) cosmic rays are charged.
- 1932: Anderson discovered the positron in cosmic rays. This was just the start for a series of new particles detected in cosmic rays: The muon 1936 again by Andersen, charged pions in 1947, and strange particles 1947–50.
- 1932: Raged debate in the US about sources and primary type of the new radiation. Millikan and Compton favored gamma rays and coined therefore the name “cosmic rays.”
- 1934: The sign of the east-west asymmetry showed that the cosmic ray primaries are positively charged particles.
- 34/38: Rossi and independently Auger discovered through coincidence measurements “extensive air showers,” showers of secondary particles caused by the collision of high energy cosmic rays with air nuclei.

- 1934: Bethe and Heitler developed the electromagnetic cascade theory; the observed particles on ground are secondaries.
- 1947: Zatsepin discovered the scaling of hadronic interactions studying the evolution of extensive air showers.
- 1949: Fermi proposed that cosmic rays are accelerated by bouncing off moving magnetic clouds in the Galaxy.
- 52-54: The first human accelerators reaching $p \gtrsim 1$ GeV were built. As a consequence, cosmic ray and high energy physics started to decouple, and cosmic ray physicists focused with time more on astrophysical questions.
- 1954: First measurements of high energy cosmic rays via sampling of extensive air showers done at the Harvard College Observatory.
- 1972: The launch of the SAS-2 satellite marked the start of high energy gamma astronomy.
- 1976: Start of the first prototype of a large-scale underwater detector for high energy neutrino astronomy, DUMAND in Hawaii.
- 1998: The Superkamiokande experiment found the first convincing evidence that neutrinos are massive observing flavor oscillations of atmospheric neutrinos.
- 2007: Completion of the Pierre Auger Observatory in Argentina, the first combination of a ground array and fluorescence telescopes in the same experiment. With its size of $A \approx 3000 \text{ km}^2$, it is a factor 30 larger than previous experiments.

2 Basic notations of particle physics

2.1 Relativistic kinematic and cross sections

2.1.1 Kinematics

The description of scattering reactions is simplified, if Lorentz invariant quantities are used. Consider for instance the squared center-of-mass energy $s = (p_a + p_b)^2 = (p_c + p_d)^2$ with four-momenta $p_i = (E_i, \mathbf{p}_i)$ in the $2 \rightarrow 2$ scattering $a + b \rightarrow c + d$,

$$s = (p_a + p_b)^2 = m_a^2 + m_b^2 + 2(E_a E_b - \mathbf{p}_a \mathbf{p}_b) = m_a^2 + m_b^2 + 2E_a E_b (1 - \beta_a \beta_b \cos \vartheta), \quad (2.1)$$

where $\beta_i = v_i = p_i/E_i$. We are interested often in the threshold energy $s_{\min}^{1/2}$ of a certain process. An important example for cosmic ray physics is the reaction $p + \gamma \rightarrow p + \pi^0$. If in this process the proton is at rest, then

$$s = m_p^2 + 2E_\gamma m_p \geq (m_p + m_\pi)^2 = m_p^2 + 2m_p m_\pi + m_\pi^2 \quad (2.2)$$

or

$$E_\gamma \geq m_\pi + \frac{m_\pi^2}{2m_p} \approx 145 \text{ MeV}. \quad (2.3)$$

Thus the photo-production of pions on protons at rest is only possible for $E_\gamma \geq 145 \text{ MeV}$. Photons with lower energy do not interact via this reaction, while higher energetic ones do. We will consider this process later again, but then as the scattering of ultrahigh energy protons on low energy photons, that is an important example for the transition from a transparent Universe at low energies to an opaque one at high energies.

Ex.: Calculate the minimal energy of a proton able to produce anti-protons scattering on another proton at rest.

Because of baryon number conservation, anti-proton production is first possible in $pp \rightarrow ppp\bar{p}$ with $s = 2m_p^2 + 2E_p m_p \geq 16m_p^2$ or $E_p \geq 7m_p$. Furthermore, the cross section of this reaction is small close to the threshold. Hence the anti-proton flux at small energies should be strongly suppressed, if anti-protons are only produced as secondaries in cosmic ray interactions.

The second important quantity characterizing a scattering process is the four-momentum transfer $t = (p_a - p_c)^2 = (p_b - p_d)^2$. As an example, we consider electron-proton scattering $e^- + p \rightarrow e^- + p$. Then

$$t = (p_e - p'_e)^2 = 2m_e^2 - 2E_e E'_e (1 - \beta_e \beta'_e \cos \vartheta). \quad (2.4)$$

For high energies, $\beta_e, \beta'_e \rightarrow 1$, and

$$t \approx -2E_e E'_e (1 - \cos \vartheta) = -4E_e E'_e \sin^2 \vartheta / 2. \quad (2.5)$$

Because of four-momentum conservation, the variable t corresponds to the squared momentum Q of the exchanged virtual photon, $t = Q^2 = (p_e - p'_e)^2 < 0$. Thus a virtual particle does

not fulfill the relativistic energy-momentum relation. The energy-time uncertainty relation $\Delta E \Delta t \gtrsim 1$ allows such a violation, if the virtual particle is exchanged only during a short enough time. Note also that the angular dependence of Rutherford scattering, $d\sigma/d\Omega \propto 1/\sin^4 \vartheta/2$ is obtained if $d\sigma/d\Omega \propto 1/t^2$.

In the reaction $e^- + p \rightarrow e^- + p$ the scattering happens most likely at small angles ϑ and small four-momentum transfer t . (Note that this does not imply small energy transfer in the lab system.) In a collider experiment, this kinematical region is difficult to observe because of the beam pipe. Moreover, the search for physics beyond the standard model as one of the most important problems in high energy physics is often performed as search for new, heavy particles. The production of particles with mass M requires typically $|t| \gtrsim M^2$ and is therefore rare. On the other hand, for the description of cosmic ray interactions in the atmosphere we are interested mainly in the most common interactions. This is one of the reasons why high energy particle physics with accelerators and with cosmic rays are focusing partly on different aspects of high energy interactions.

2.1.2 Cross section, interaction depth, and slant depth

Consider a cylinder of length l and area A filled with N scattering centers each with cross section σ . Their number density n is $n = N/(Al)$. Let us assume first that $N\sigma \ll A$. Then the fraction of incoming particles absorbed in the cylinder is simply

$$\frac{N\sigma}{A} = nl\sigma \equiv \tau \quad (2.6)$$

and defines the optical or interaction depth $\tau \equiv nl\sigma$. Our assumption $N\sigma \ll A$ corresponds to $\tau \ll 1$, an “(optical) thin” or transparent source in contrast to an “(optical) thick” source with $\tau \gg 1$. In general, we have to calculate how much radiation is absorbed passing the infinitesimal distance dl ,

$$dI = -I d\tau = -In\sigma dl. \quad (2.7)$$

Integrating gives

$$I = I_0 \exp(-\tau) \quad \text{or} \quad I(l) = I_0 \exp\left(-\int_0^l dl n\sigma\right). \quad (2.8)$$

In cosmic ray physics, one introduces often the interaction length $\lambda_i = m/\sigma_i$ measured in g/cm^2 and replaces the path length l by the slant depth X ,

$$X(l) = \int_0^l dl \rho(l') \quad \text{or} \quad X(h) = \int_h^\infty dh \rho(h'). \quad (2.9)$$

Hence, X measures the weight per area of the material crossed. The version on the RHS of Eq. (2.9) is appropriate in the case of the Earth atmosphere, where $X = 0$ corresponds to $h \rightarrow \infty$, while X measured from the zenith is numerically equal to $1030 \text{ g}/\text{cm}^2$ at sea level. The advantage of X is obviously to hide the integration in X ,

$$\tau = \int_0^X \frac{dX'}{\lambda} = \frac{X}{\lambda}. \quad (2.10)$$

particle	main decay mode	life-time $t_{1/2}$	range $ct_{1/2}$
γ	–	∞	∞
e^-	–	∞	∞
p	–	∞	∞
n	$n \rightarrow p + e^- + \bar{\nu}_e$	886s	2.65×10^{13} cm
μ^-	$\mu^- \rightarrow e^- + \bar{\nu}_e + \nu_\mu$	$t_{1/2} \sim 2.20 \times 10^{-6}$ s	659 m
π^-	$\pi^- \rightarrow \mu^- + \bar{\nu}_\mu$	$t_{1/2} \sim 2.60 \times 10^{-8}$ s	780 cm
π^0	$\pi^0 \rightarrow 2\gamma$	$t_{1/2} \sim 8.4 \times 10^{-17}$ s	25.1 nm
ν	–	∞	∞

Table 2.1: The known particles around 1950 together with their main decay mode, their life-time and range.

2.2 Particles and interactions

2.2.1 Our particle inventory

The particles known around 1950 are shown in Table 2.1 together with their main decay mode and their life-time $t_{1/2}$ and range $ct_{1/2}$. Some immediate consequences of the life-times given are:

- Neutrons with $\Gamma = E/m_n \gtrsim 10^9$ or $E \gtrsim 10^{18}$ eV are stable on galactic scales (~ 10 kpc). A source of neutrons with $E \gtrsim 10^{18}$ eV in our galaxy would provide neutral, strong interacting primaries, while at lower energies it would be visible as a $\bar{\nu}_e$ source from neutron decay on the flight.
- In the atmosphere, only low energy charged pions will decay and produce neutrinos, whilst at high energies charged pions mainly scatter. Similarly, most high energy muons do not decay within the extension of the atmosphere, ~ 15 km. Thus the neutrino flux produced by cosmic rays in the atmosphere should be a steeper function of energy than the cosmic ray flux. This opens the possibility to perform high energy neutrino astronomy at energies $E \gg$ TeV, for which the background of atmospheric neutrinos becomes negligible.
- The long muon range can be used to enlarge the effective volume of a neutrino detector, observing also muons produced outside the proper detector volume.

2.2.2 Comparison of electromagnetic, weak and strong interactions

The energy-time uncertainty relation $\Delta E \Delta t \gtrsim 1$ restricts the emission of a heavy particle with mass M by a lighter one to times $\Delta t \lesssim 1/M$. Thus the range Δt of an interaction over which a massive particle can be exchanged should be limited by $1/M$.

This idea leads to the generalization of the Coulomb potential to the Yukawa potential,

$$V(r) = g^2 \frac{\exp(-Mr)}{r} \rightarrow \frac{g^2}{r} \quad \text{for } M \rightarrow 0. \quad (2.11)$$

In non-relativistic quantum mechanics, the connection between the cross section σ and the potential V is given via the scattering amplitude $f(\vartheta)$,

$$\sigma = \int d\Omega \frac{d\sigma}{d\Omega} = \int d\Omega |f(\vartheta)|^2. \quad (2.12)$$

In the so-called Born approximation, this scattering amplitude $f(\vartheta)$ is the Fourier transform of the potential,

$$f(q) = -\frac{m}{2q\hbar^2} \int d^3q \exp(-i(\mathbf{q}\mathbf{r}))V(r), \quad (2.13)$$

where $\mathbf{q} = \mathbf{p} - \mathbf{p}'$ or $q = 2p \sin \vartheta/2$.

Performing the integral for the Yukawa potential one obtains

$$\frac{d\sigma}{d\Omega} \propto \frac{g^4}{(q^2 + M^2)^2}. \quad (2.14)$$

This result explains the difference in strength between electromagnetic and weak interactions, although their coupling constants have roughly the same size, $g \approx e$. Photons are massless and thus

$$\frac{d\sigma}{d\Omega} \propto \frac{e^4}{q^4}, \quad (2.15)$$

while the bosons exchanged in weak interactions are heavy. If $s \ll M^2$, then also $|t| \ll M^2$ and $q^2 \ll M^2$, and thus the exchange of massive gauge bosons results in

$$\frac{d\sigma}{d\Omega} \propto \frac{g^4}{M^4} \propto G_F^2, \quad \text{with} \quad G_F \equiv \frac{\sqrt{2}g^2}{8M_W^2}. \quad (2.16)$$

The masses of the W and Z bosons that intermediate weak interactions have been measured at accelerators as $M_Z = 91.2 \text{ GeV}$ and $M_W = 80.4 \text{ GeV}$.

The total cross section σ is obtained by integrating over $d\Omega \propto d(\cos \vartheta) \propto dt$. We expect from dimensional analysis that $\sigma \sim G_F^2 (\text{energy})^2$ and often the result can be estimated. For instance, for the scattering of a high-energy neutrino on a nucleon at rest the integration gives an additional factor $s \approx 2m_N E_\nu$, and the cross section is numerically for $s \ll m_W^2$

$$\sigma_{\nu N} \sim G_F^2 s \approx 10^{-37} \text{ cm}^2 \left(\frac{E_\nu}{100 \text{ GeV}} \right). \quad (2.17)$$

Finally, we consider strong interactions. The largest contribution to the proton-proton cross section should result from the exchange of the lightest, strongly interacting particle, the pion. Integrating gives

$$\sigma \sim \frac{g_\pi^4}{(4\pi)^2} \int_{-s}^0 \frac{dt}{(t - m_\pi^2)^2} = \alpha_\pi^2 \frac{s}{m_\pi^2(s - m_\pi^2)} \rightarrow \frac{\alpha_\pi^2}{m_\pi^2} \approx 20\alpha_s^2 \text{ mbarn} \quad (2.18)$$

compared to the measured value $\sigma \approx 50 \text{ mbarn}$. Hence the proton-pion coupling $\alpha_\pi = g_\pi^2/(4\pi)$ is of order one and perturbation theory for strong interactions seems to make no sense. However, coupling constants are—despite the name—in generally not constant but depend on the scale Q^2 probed. In the case of strong interactions, the coupling becomes smaller for large Q^2 , a phenomenon called “asymptotic freedom.” As a consequence, perturbation theory can be used in QCD, however only in a restricted kinematical range, $Q^2 \gtrsim \text{few} \times \text{GeV}^2$. Unfortunately, for cosmic ray interactions most important is the regime of small momentum-transfer that is not (yet) accessible to predictions from first principles and requires therefore the use of phenomenological models.

We have argued that the exchange of the lightest (relevant) particle dominates the total cross section. But what happens, when an infinite number of particles can be transmitted,

hadron	valence quarks	hadron	valence quarks
p	uud	Λ	uds
n	udd	K^+	$u\bar{s}$
π^+	$u\bar{d}$	K^0	$d\bar{s}$
π^0	$(u\bar{u} + d\bar{d})/\sqrt{2}$		

Table 2.2: Valence quark content of hadrons

with increasing multiplicity for increasing mass? This is the case of hadrons for which a zoo of resonances exists, cf. the Chew-Frautschi plot in Fig. 2.1. For instance, the vector mesons A_2, ρ_3, \dots can be viewed as $J = 2, 3, \dots$ excitations of the ρ meson with spin $J = 1$. After summing up the infinite number of exchanged hadrons per trajectory, one can replace them by a single “effective particle” (called “reggeons”). The high energy behavior of hadronic cross sections is modeled as an exchange of these reggeons, with their properties read off from Chew-Frautschi plots as in Fig. 2.1.

Quark model and hadronization For $q \gtrsim 1/m_p$, the scattering amplitude for e.g. electron-proton scattering should reflect the proton size 10^{-13} cm. However, a form factor typical for scattering on point-like particles was found experimentally. This led to the parton model: Protons (as all hadrons) consist of point-like constituents, quarks and gluons. The valence quark content of some hadrons is given in Tab. 2.2. At high momentum transfer, a probe scatters on partons independently (“spectator model”). Hence, the parton model predicts e.g. for the ratio of pion-proton and proton-proton cross sections

$$\frac{\sigma_{\pi p}}{\sigma_{pp}} = \frac{2}{3}, \quad (2.19)$$

in good agreement with experiment.

Which kind of hadrons are mainly produced in the process $e^+e^- \rightarrow q\bar{q} \rightarrow$ hadrons? Mainly mesons ($q\bar{q}$) with only $\sim 5\%$ of nucleons (qqq), because it is easier to combine two quarks into a colorless, light meson than three quarks into a colorless, rather heavy baryon. Out of the mesons, 90% are pions while the remaining ones are mainly kaons. While 1/3 of pions are neutral ones and produce photons, the other 2/3 are charged and produce neutrinos. Hence photon and neutrino fluxes produced by hadronization are closely connected.

2.3 Exercises

1. Derive the connection between $d\sigma/d\Omega$ and $d\sigma/dt$ and the integration limits in t for a general $2 \rightarrow 2$ scattering process.
2. Find the minimal energy E_{th} of a proton scattering on a photon with the typical energy of the cosmic microwave background ($T \approx 2.7$ K) for the process $p + \gamma \rightarrow p + \pi^0$. Guess the cross section of this reaction, check it against the curve at <http://pdg.lbl.gov>, and estimate the mean free path of a proton with $E \gg E_{\text{th}}$.
3. Consider the 2-particle decay $\pi^0 \rightarrow 2\gamma$. What are the minimal and maximal photon energies, if the pion moves with velocity v ? What is the shape of the photon spectrum dN/dE ?

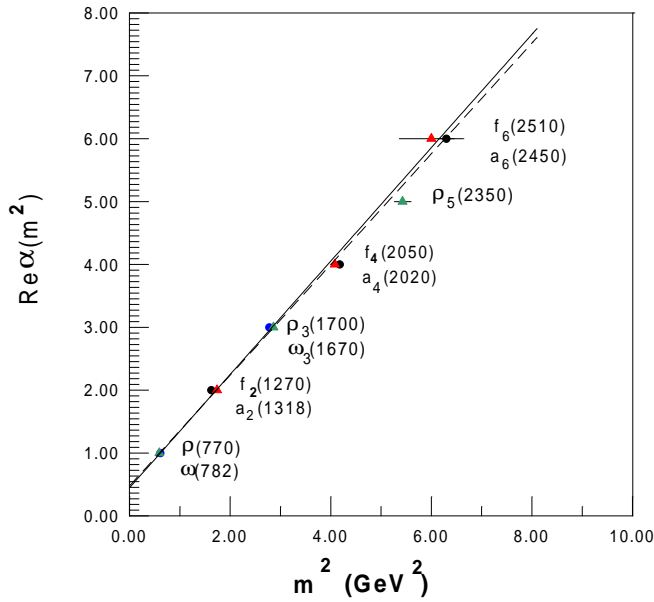


Figure 2.1: Chew-Frautschi plot, i.e. the spin against the squared mass, for the trajectories of the ω , ρ , f_2 , and a_2 mesons, from Ref. [3].

3 Galactic cosmic rays

3.1 Basic observations

3.1.1 Cosmic ray intensity and composition

The integral intensity $I(> E)$ of cosmic rays is defined as the number of particles with energy $> E$ crossing an unit area per unit time and unit solid angle. Thus its units are $[I] = \text{cm}^{-2}\text{s}^{-1}\text{sr}^{-1}$. The (differential) intensity $I(E)$ and the integral intensity are connected by

$$I(> E) = \int_E^\infty dE' I(E'). \quad (3.1)$$

The particle flux \mathcal{F} from one hemisphere through a planar detector is

$$\mathcal{F}(E) = \int d\Omega I(E) \cos \vartheta = I(E) \int_0^{2\pi} d\phi \int_0^{\pi/2} d\vartheta \sin \vartheta \cos \vartheta = \pi I(E) \int_0^{\pi/2} d\vartheta \sin 2\vartheta = \pi I(E), \quad (3.2)$$

where we have assumed that the intensity is isotropic. The (differential) number density of cosmic rays with velocity v is

$$n(E) = \frac{4\pi}{v} I(E). \quad (3.3)$$

More generally, the intensity I may depend both on the position \mathbf{x} of the detector and on its orientation ϕ, ϑ . We can connect I to the phase space distribution $f(\mathbf{x}, \mathbf{p})$ of cosmic rays by comparing $dN = f(\mathbf{x}, \mathbf{p}) d^3x d^3p$ with the definition $I = dN/(dA dt d\Omega dE)$,

$$I(\mathbf{x}, p, \vartheta, \phi) = vp^2 \frac{dp}{dE} f(\mathbf{x}, \mathbf{p}) = p^2 f(\mathbf{x}, \mathbf{p}). \quad (3.4)$$

Figure 3.1 shows $I(E)$ separately for some important elements. First, one recognizes that the main component of cosmic rays are protons, with additionally around 10% of helium and an even smaller admixture of heavier elements.

The relative abundance of elements measured in cosmic rays (dark, filled circles) is compared to the one in solar system (blue, open circles) in Fig. 3.2. Both curves show the odd even effect, i.e. the tighter bound nuclei with an even numbers of protons and neutrons are more abundant. The main difference of the two curves is that the Li-Be-B group ($Z = 3 - 5$) and the Sc-Ti-V-Cr-Mn

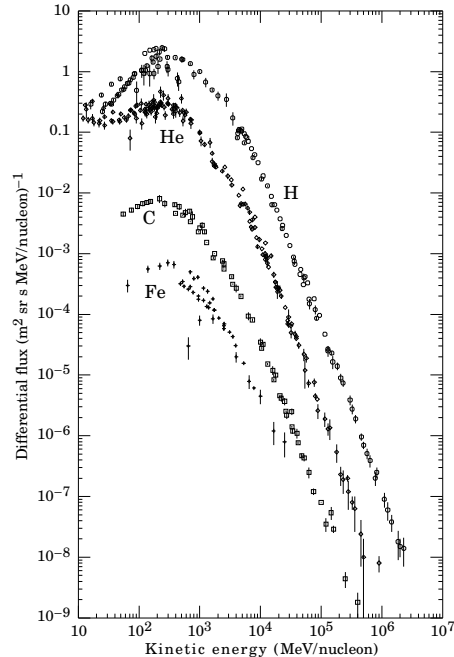


Figure 3.1: Cosmic rays intensity for several elements, from Ref. [4].

($Z = 21 - 25$) group are much more abundant in cosmic rays than in the solar system. We explain this later as a propagation effect: The elements from the Li-Be-B group are produced as secondaries in cosmic rays interactions in the Galaxy.

Second, the spectra shown in Fig. 3.1 are above a few GeV power-laws, practically without any spectral features. The total cosmic ray spectrum is

$$I(E) \sim 1.8E^{-\alpha} \frac{\text{particles}}{\text{cm}^2 \text{ s st GeV}} \quad (3.5)$$

in the energy range from a few GeV to 100 TeV with $\alpha \approx 2.7$. Around 10^{15} eV (the “knee”), the slope steepens from $\alpha \approx 2.7$ to $\alpha \approx 3.0$. The spectrum above 10^{18} eV will be discussed in Chapter 6.

The power-law form of the cosmic ray spectrum indicates that they are produced via non-thermal processes, in contrast to all other radiation sources like e.g. stars or (super-) novae known until the 1950’s.

Third, small differences in the exponent α of the power-law for different elements are visible: The relative contribution of heavy elements increases with energy.

The kinetic energy density of cosmic rays is

$$\rho_{\text{CR}} = \int dE E_k n(E) = 4\pi \int dE \frac{E_k}{v} I(E). \quad (3.6)$$

Extrapolated outside the reach of the solar wind, it is

$$\rho_{\text{CR}} \approx 0.8 \text{ eV/cm}^3 \quad (3.7)$$

compared to the average energy density $\rho_b \approx 100 \text{ eV/cm}^3$ of baryons in the Universe, of star light $\rho_{\text{light}} \approx 5 \text{ eV/cm}^3$ in the disc, and in magnetic fields $\rho_{\text{mag}} = 0.5 \text{ eV/cm}^3$ for $B = 6 \mu\text{G}$. If the local value of ρ_{CR} would be representative for the Universe, 1% of the energy of all baryons would be in the form of relativistic particles. This is rather unlikely and suggests that cosmic rays are accumulated in the Galaxy.

Solar modulations When cosmic rays enter our Solar System, they must overcome the outward-flowing solar wind. This wind impedes and slows the incoming cosmic rays, reducing their energy and preventing the lowest energy ones from reaching the Earth. This effect is known as solar modulation. The Sun has an 11-year activity cycle which is reflected in the ability of the solar wind to modulate cosmic rays. As a result, the cosmic ray intensity at Earth is anti-correlated with the level of solar activity, i.e., when solar activity is high and there are lots of sunspots, the cosmic ray intensity at Earth is low, and vice versa.

Since the number of cosmic rays increases with decreasing energy, most cosmic rays are not visible to us. This suppression effect at energies below a few GeV is clearly visible in Fig. 3.3, where the intensity of oxygen is shown for three different periods.

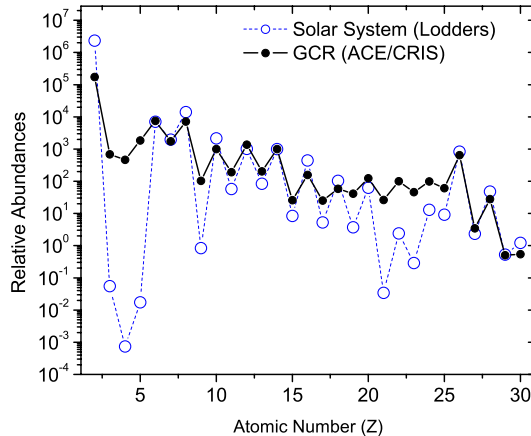


Figure 3.2: Abundance of elements measured in cosmic rays compared to the solar system abundance, from Ref. [5].

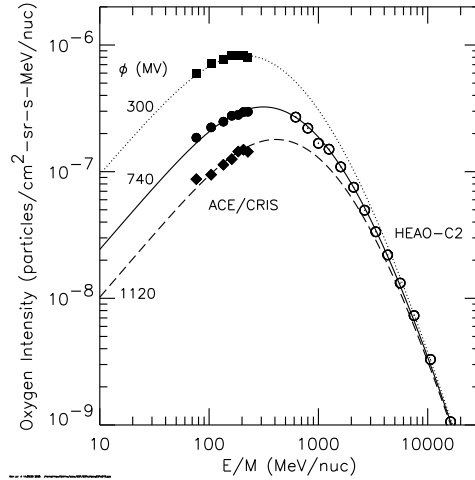


Figure 3.3: Oxygen cosmic ray intensity during three different periods: Sept. 1997 (squares), Feb 2000 (circles), Jan. 2001 (diamonds), from Ref. [6].

3.1.2 Anisotropies and deflections in regular magnetic fields

Experimental results on dipole anisotropies

Above 100 GeV, when the influence of the Sun becomes negligible, the cosmic ray flux is consistent with isotropy. At higher energies, when cosmic rays drift slowly out the galaxy, one expects to detect first anisotropies on large angular scales. Such anisotropies can be characterized in first approximation by a pure dipole, $I = I_0 + I_1 \cos \vartheta$,

$$\delta = \frac{I_{\max} - I_{\min}}{I_{\max} + I_{\min}} = \frac{I_1}{I_0}. \quad (3.8)$$

Most experimental detections or limits for δ at energies $E \lesssim 10^{15}$ eV are in the range $10^{-4} \lesssim \delta \lesssim 10^{-3}$, cf. Fig. 3.4. Many experimental searches are using that the experimental exposure of a cosmic ray experiment taking continuously data is uniform in right ascension¹. Then one performs an one-dimensional harmonic analysis: One sums

$$a_k = \frac{2}{n} \sum_{a=1}^n \cos(k\phi_i) \quad \text{and} \quad b_k = \frac{2}{n} \sum_{a=1}^n \sin(k\phi_i) \quad (3.9)$$

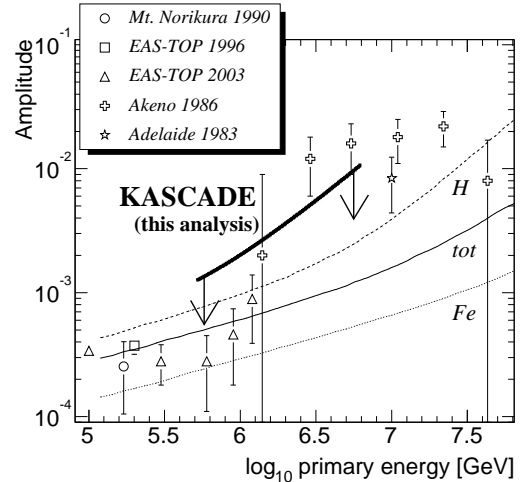


Figure 3.4: Experimental limits on the anisotropy of cosmic rays, from Ref. [7].

¹In the equatorial coordinate system one projects the usual geographical latitude and longitude on the celestial sphere. The right ascension measures the angle east from the vernal equinox point to an object projected on the celestial equator.

over the n data points. The amplitude r_k and phase ϕ_k of the k .th harmonic are given by

$$r_k = \sqrt{a_k^2 + b_k^2} \quad \text{and} \quad \phi_k = \arctan(b_k/a_k) \quad (3.10)$$

with the chance probability

$$p_{\text{ch}} = \exp\left(-nr_k^2/4\right) \quad (3.11)$$

to observe a larger value of r_k in an isotropic distribution.

Generalized Liouville theorem We measure cosmic rays after they traversed the magnetic field of the Earth and of the Milky Way, and possibly extragalactic magnetic fields. It is therefore important to separate between genuine anisotropies and those eventually induced by the cosmic ray propagation in magnetic fields.

We want to show now that the intensity I is constant along any possible cosmic ray trajectory. Let us consider the evolution of the phase space distribution $f(\mathbf{x}, \mathbf{p})$ from the time t to $t + dt$. The number dN of particles around the point \mathbf{x}', \mathbf{p}' at $t' = t + dt$ is

$$f(\mathbf{x}', \mathbf{p}') d^3x' d^3p'. \quad (3.12)$$

This number remains constant, if the Jacobian of the transformation $\mathbf{x}, \mathbf{p} \rightarrow \mathbf{x}', \mathbf{p}'$ is one,

$$J = \frac{\partial(\mathbf{x}', \mathbf{p}')}{\partial(\mathbf{x}, \mathbf{p})} = 1. \quad (3.13)$$

It is sufficient to show that the time-derivative $dJ/dt = 0$, i.e. that in the expansion of J the first-order terms dt vanish. From $\mathbf{x}' = \mathbf{x} + \mathbf{v}dt$ and $\mathbf{p}' = \mathbf{p} + \mathbf{F}dt$, the diagonal of J follows as

$$1, 1, 1, 1 + \frac{\partial F_x}{\partial p_x} dt, 1 + \frac{\partial F_y}{\partial p_y} dt, 1 + \frac{\partial F_z}{\partial p_z} dt, \quad (3.14)$$

while the off-diagonal elements are of order $\mathcal{O}(dt)$. The expansion of dJ to first-order in dt is thus

$$J = 1 + \left(\frac{\partial F_x}{\partial p_x} + \frac{\partial F_y}{\partial p_y} + \frac{\partial F_z}{\partial p_z} \right) dt + \dots \quad (3.15)$$

Thus the phase space distribution $f(\mathbf{x}, \mathbf{p})$ is constant along a trajectory, if $\nabla_p \mathbf{F} = 0$, which is fulfilled in an electromagnetic field. Moreover, $p = |\mathbf{p}|$ is constant in a pure magnetic field and hence also $p^2 f(\mathbf{x}, p)$. With Eq. (3.4) it follows that also the intensity I is constant along any possible cosmic ray trajectory.

Finally, we remark that the Liouville theorem does not imply that magnetic fields can not enhance existing anisotropies. In fact, they can act as magnetic lenses, enhancing or decreasing the flux received from *point* sources similar as gravitational lenses.

Latitude and east-west effect An isotropic cosmic ray flux remains isotropic propagating through a magnetic field as long as the phase space is simply connected. In other words, a necessary condition is that all trajectories starting from the point considered on Earth (after reversing the charge of the particle) reach $r = \infty$. At low enough energies, this condition may be violated, because trajectories can be deflected back to the Earth or stay within a finite distance r , cf. Fig. 3.5. In this case, the magnetic field does induce anisotropies in the observed flux.

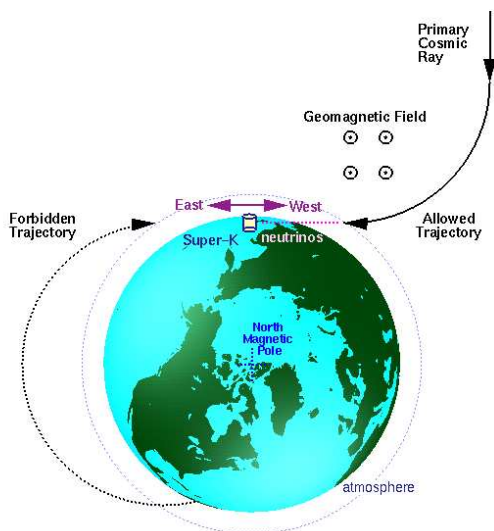


Figure 3.5: A sketch of the east-west effect [8].

Consider a particle of charge Ze with orbit in the equatorial plane of a dipole with magnetic moment M (as a good model for the geomagnetic field). Equating the centrifugal and the Lorentz force gives

$$Ze|\mathbf{v} \times \mathbf{B}| = \frac{mv^2}{r} \quad (3.16)$$

with $B = \mu_0/(4\pi)M/r^3$. The radius of the orbit is

$$r = \left(\frac{\mu_0}{4\pi} \frac{ZeM}{p} \right)^{1/2}. \quad (3.17)$$

Setting $r = R_{\oplus}$ and using $M = 8 \times 10^{22}$ Am as magnetic moment of the Earth, it follows

$$\frac{p}{Z} = \frac{\mu_0}{4\pi} \frac{eM}{R_{\oplus}^2} \approx 59.6 \text{ GeV}. \quad (3.18)$$

This is the minimal momentum of a proton able to reach the Earth from the east, if its orbit is exactly in the (magnetic) equatorial plane. The sign of this east-west asymmetry was used by Rossi and others to show that the cosmic ray primaries are positively charged. Towards the poles, the influence of the dipole field becomes weaker ($\mathbf{v} \times \mathbf{B}$), and the cutoff momentum becomes thus smaller. Thus the integrated cosmic ray intensity increases with latitude for charged particles (“latitude effect”).

Compton-Getting effect Compton and Getting first discussed that a relative motion of observer and cosmic ray sources results in an anisotropic cosmic ray flux, using this effect as signature for the Galactic origin of cosmic rays with $E \gtrsim 0.1$ GeV.

Lorentz invariance² requires that the phase space distribution function f in the frame of the observer, $f'(\mathbf{r}', \mathbf{p}')$, equals the one in the frame in which the cosmic ray flux is isotropic,

²The differentials d^3x and d^3p transform opposite under Lorentz transformations, while the particle number dN is obviously a scalar.

$f(\mathbf{r}, \mathbf{p})$. Expanding in the small parameter $\mathbf{p} - \mathbf{p}' \approx -p \mathbf{u}$, it follows

$$f'(\mathbf{p}') = f(\mathbf{p}') - p \mathbf{u} \cdot \frac{\partial f(\mathbf{p}')}{\partial \mathbf{p}'} + \mathcal{O}(u^2) = f(\mathbf{p}') \left(1 - \frac{\mathbf{u} \cdot \mathbf{p}}{p} \frac{d \ln f}{d \ln p'} \right). \quad (3.19)$$

Since $u \equiv |\mathbf{u}| \ll 1$, the anisotropy induced by the Compton-Getting effect is dominated by the lowest moment, i.e. its dipole moment. Changing to the differential intensity $I(E) = p^2 f(p)$, one obtains

$$I'(E') \simeq I(E) \left[1 + \left(2 - \frac{d \ln I}{d \ln E'} \right) \frac{\mathbf{u} \cdot \mathbf{p}}{p} \right]. \quad (3.20)$$

Thus the dipole anisotropy due to the Compton-Getting effect has the amplitude

$$\delta_{\text{CG}} \equiv \frac{I_{\text{max}} - I_{\text{min}}}{I_{\text{max}} + I_{\text{min}}} = \left(2 - \frac{d \ln I}{d \ln E} \right) u. \quad (3.21)$$

The Sun moves with $u_{\odot} = 220 \text{ km/s}$ around the center of the Milky Way. Most likely, the local ‘‘cosmic ray rest frame’’ is co-rotating with the nearby stars and the relevant velocity u for the CG effect is therefore much smaller. Taking into account the observed spectrum $I(E) \propto E^{-2.7}$ of cosmic rays below the knee, the Compton-Getting effect should results in a dipole anisotropy which amplitude is bounded by $\delta_{\text{CG}} = (2 + 2.7) u \lesssim 0.4\%$.

3.2 Propagation of Galactic cosmic rays

Cascade equation We want to explain the large over-abundance of the group Li-Be-B in cosmic rays compared to the Solar system. We consider two species, primaries with number density n_p and secondaries with number density n_s . If the two species are coupled by the spallation process $p \rightarrow s + X$, then

$$\frac{dn_p}{dX} = -\frac{n_p}{\lambda_p}, \quad (3.22a)$$

$$\frac{dn_s}{dX} = -\frac{n_s}{\lambda_s} + \frac{p_{\text{sp}} n_p}{\lambda_p}, \quad (3.22b)$$

where $X = \int dl \rho(l)$ measures the amount of traversed matter, $\lambda_i = m/\sigma_i$ are the interaction lengths (in gr/cm^2), and $p_{\text{sp}} = \sigma_{\text{sp}}/\sigma_{\text{tot}}$ is the spallation probability.

The system Eqs. (3.22) can be easily solved (Exercise 3.1) and using as initial condition $n_s(0) = 0$ we obtain as ratio

$$\frac{n_s}{n_p} = \frac{p_{\text{sp}} \lambda_s}{\lambda_s - \lambda_p} \left[\exp \left(\frac{X}{\lambda_p} - \frac{X}{\lambda_s} \right) - 1 \right]. \quad (3.23)$$

If we consider as secondaries a group like Li-Be-B that has a much smaller abundance in the solar system than in cosmic rays, most of them have to be produced by spallation from heavier elements like the C-N-O group. With $\lambda_{\text{CNO}} \approx 6.7 \text{ g/cm}^2$, $\lambda_{\text{LiBeB}} \approx 10 \text{ g/cm}^2$, and $p_{\text{sp}} \approx 0.35$ measured at accelerators, the observed ratio 0.25 is reproduced for $X \approx 4.3 \text{ g/cm}^2$, see Fig. 3.6.

With $h = 300 \text{ pc} \approx 10^{21} \text{ cm}$ as thickness of the Galactic disc, $n_H \approx 1/\text{cm}^3$ as density of the interstellar medium, a cosmic ray following a straight line perpendicular the disc crosses only $X = m_H n_H h \approx 10^{-3} \text{ g/cm}^2$. The residence time of cosmic rays in the galaxy follows as $t \sim (4.3/10^{-3})(h/c) \sim 1.4 \times 10^{14} \text{ s} \sim 5 \times 10^6 \text{ yr}$. This result can only be explained, if the propagation of cosmic rays resembles a random-walk. Moreover, it suggests that acceleration and propagation can be treated separately.

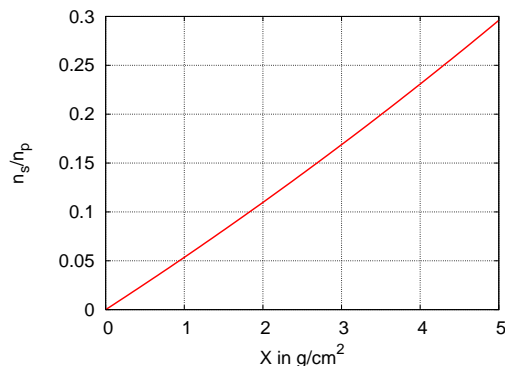


Figure 3.6: The ratio n_s/n_p as function of the traversed amount of matter X .

Random walks After N steps \mathbf{l}_i of the same size $|\mathbf{l}_i| = l$ a particle that started at zero is at the position $\mathbf{d} = \sum_{i=1}^N \mathbf{l}_i$. We assume that the direction of each step \mathbf{l}_i is chosen randomly. Then the scalar product of \mathbf{d} with itself is

$$\mathbf{d} \cdot \mathbf{d} = \sum_{i=1}^N \sum_{j=1}^N \mathbf{l}_i \cdot \mathbf{l}_j, \quad (3.24)$$

and splitting the sum into the diagonal and the off-diagonal terms, we obtain

$$d^2 = Nl^2 + 2l^2 \sum_{i=1}^N \sum_{j<i}^N \cos \vartheta_{ij} \approx Nl^2. \quad (3.25)$$

By assumption, the angles ϑ_{ij} between \mathbf{l}_i and \mathbf{l}_j are chosen randomly and thus the off-diagonal terms cancel against each other.

One might think of two different reasons behind the random walk: Scattering with isotropic re-emission as in the case of photons in the Sun or diffusion in turbulent magnetic fields. The first possibility is excluded by the small scattering probability $\tau = h\sigma n_H \sim 10^{21} \times 10^{-25} \times 1 \approx 10^{-4}$ and by the fact that at high energies scattered particle are concentrated in the forward direction within a cone of opening angle $\vartheta \sim 1/\Gamma$. Hence we are lead to examine the second possibility, the scattering of cosmic rays on turbulent magnetic fields in the Galactic disc.

Diffusion equation The continuity equation for the number density n and its current \mathbf{j} (that corresponds to \mathcal{F} in our usual notation),

$$\nabla \mathbf{j} + \frac{\partial n}{\partial t} = 0, \quad (3.26)$$

leads together with Fick's law for an isotropic medium,

$$\mathbf{j} = -D\nabla n, \quad (3.27)$$

to the diffusion equation

$$\frac{\partial n}{\partial t} - \nabla(D\nabla n) = Q, \quad (3.28)$$

where we added additionally a source term $Q = Q(E, \mathbf{x}, t)$. Note that the diffusion equation can be transformed for a diffusion coefficient D that is independent on \mathbf{x} into the free Schrödinger equation substituting $D \leftrightarrow \hbar^2/(2m)$ and $t \leftrightarrow -it$. Hence we can borrow the free propagator for a non-relativistic particle as Green's function $G(r)$ for the diffusion equation with $D = \text{const.}$ and obtain with the mentioned substitutions,

$$G(r) = \frac{1}{(4\pi Dt)^{3/2}} \exp[-r^2/(4Dt)]. \quad (3.29)$$

Thus the mean distance traveled outward is $\propto \sqrt{Dt}$, as in a random walk with $\langle r^2 \rangle \sim Nl_0^2$. Connecting the two pictures, we obtain $D \sim Nl_0^2/t \sim vl_0$ with $v = Nl_0/t$. Therefore, the diffusion coefficient D can be estimated as the product of the cosmic ray velocity $v \approx c$ and its mean free path l_0 . A more precise analysis gives $D = l_0v/3$, where the factor three reflects the number of spatial dimensions.

Diffusion coefficient We estimate now the energy-dependence of $D(E)$ and its numerical value for a cosmic ray propagating in the Galactic disc. We start picturing its propagation as a random-walk caused by scatterings on magnetic clouds of size r_0 . Then one can distinguish two different regimes:

- At low energies, i.e. when the Larmor radius $R_L = p/(ZeB)$ is smaller than the size r_0 of magnetic clouds with density n , the angles between the entrance and the exit directions are isotropically distributed. Since the direction is on average changed considerably in each scattering process, the mean free path l_0 is simply the distance between clouds, $l_0 = 1/(\sigma n) \sim 1/(r_0^2 n)$ and thus

$$D_0 = \frac{1}{3}l_0v \sim \frac{1}{3} \frac{c}{r_0^2 n} \sim \text{const.} \quad (3.30)$$

- At high energies, cosmic rays are deflected in each cloud only by a small angle $\delta \sim r_0/R_L$. The directions are uncorrelated and thus the mean deflection is zero, $\langle \delta \rangle = 0$, and the variance $\langle \delta^2 \rangle$ is given again by the result for a random-walk, $\langle \delta^2 \rangle \sim N(r_0/R_L)^2$. The effective free mean path l_0 is the distance after which $\langle \delta^2 \rangle \sim 1$. Hence the energy-dependence of the diffusion coefficient is

$$D(E) = \left(\frac{R_L}{r_0} \right)^2 D_0 \propto E^2. \quad (3.31)$$

- The transition between these two regimes happens when $R_L(E_{\text{cr}}) = r_0$. Numerically, this energy is given by $E_{\text{cr}} \approx 10^{15} \text{eV} (B/\mu\text{G})(r_0/\text{pc})$.

Obviously, the picture of magnetic clouds or domains with an unique size r_0 is an oversimplification. In a more realistic picture, there is a distribution of magnetic field fluctuations that can be easiest characterized by the spectrum of its Fourier components, $\langle B^2(k) \rangle \propto k^{-\alpha}$. Charged particles scatter mainly at field fluctuations which wave numbers k matches their Larmor radius, $k \sim 1/R_L$. If the amplitude of this resonant magnetic field fluctuation is δB_{res} , then $D \approx (\delta B_{\text{res}}/B)^{-2} v R_L/3$ instead of our over-simplified estimate (3.30). Thus the energy dependence of D below E_{cr} is determined by the power-spectrum of magnetic field fluctuations. The size r_0 of magnetic field domains is in this picture replaced by the correlation length l_c , i.e. the length scale below the field is smooth.

Diffusion and cosmic ray anisotropies In the diffusion picture, the resulting net cosmic ray flux is connected via Fick's law with the diffusion tensor. We assume a small, pure dipole anisotropy, $I = I_0 + I_1 \cos \vartheta$ and $I_1 \ll I_0$, and choose the z axis along the dipole axis. Only the dipole term contributes integrating $I(E, \vartheta)$,

$$\mathcal{F}_z(E) = 2\pi \int_0^\pi d\vartheta \sin \vartheta I(E, \vartheta) \cos \vartheta = \frac{4\pi}{3} I_1(E). \quad (3.32)$$

On the other hand, for diffusion Fick's law is valid,

$$\mathcal{F}_z(E) = -D_{zz} \partial n(E) / \partial z. \quad (3.33)$$

Comparing the two equations we obtain

$$I_1 = -\frac{3}{4\pi} D_{zz} \frac{\partial n}{\partial z}. \quad (3.34)$$

Then the anisotropy δ is

$$\delta = \frac{I_{\max} - I_{\min}}{I_{\max} + I_{\min}} = \frac{I_1}{I_0} = \frac{3\mathcal{F}_z}{4\pi I_0} = -3D_{zz} \frac{1}{cn} \frac{\partial n}{\partial z}. \quad (3.35)$$

The experimental results for δ provide thus information on D . For an estimate we set $\partial n / \partial z \approx n/h$ where h is the characteristic scale on which n changes. With $h \sim 500$ pc and using $\delta \sim 3 \times 10^{-4}$, it follows

$$D \approx \frac{1}{3} \delta ch \approx 5 \times 10^{27} \text{ cm}^2/\text{s}. \quad (3.36)$$

Next we can estimate the mean free path of cosmic rays from $D = cl_0/3$ and obtain $l_0 \sim 5 \times 10^{17}$ cm or 0.15 pc. Finally, we estimate the residence time of cosmic rays in the disc as

$$\tau = \frac{h^2}{2D} \approx 8 \times 10^6 \text{ yr}. \quad (3.37)$$

This means that the prediction for the residence time in our simple diffusion picture agrees in magnitude with observations. Since cosmic rays are confined in the Galactic plane, and the Sun is located somewhat above the plane, this diffusion flux should be directed towards the northern Galactic hemisphere.

Complete cascade equation A rather general set of equations describes the evolution of N species coupled by interactions $k \leftrightarrow i$ are the following transport or cascade equations,

$$\begin{aligned} \frac{\partial n_i(E, \mathbf{x}, t)}{\partial t} - \nabla(D\nabla n_i(E, \mathbf{x}, t)) &= Q(E, \mathbf{x}, t) \\ &- \left(c\rho\lambda_{i,\text{inel}}^{-1}(E) + \lambda_d^{-1} \right) n_i(E, \mathbf{x}, t) \\ &- \frac{\partial}{\partial E} (\beta_i n_i(E, \mathbf{x}, t)) \\ &+ \sum_k \int_E^\infty dE' \frac{d\sigma_{ki}(E', E)}{dE} n_k(E', \mathbf{x}, t). \end{aligned} \quad (3.38)$$

The first line describes diffusion, while the second line accounts for the loss of particles in the energy interval $[E : E + dE]$ because of interactions or decays with $\lambda_d = \Gamma\tau_{1/2}$. The third line describes continuous energy losses $\beta = dE/dt$ of a particle i : Two important examples are synchrotron radiation and adiabatic redshift losses due to the expansion of the Universe. Since βn is the particle flux in energy space (with ‘‘velocity’’ dE/dt), $\partial/\partial E(\beta_i n_i(E, \mathbf{x}))$ is the divergence of this flux. Hence it is the analogue in energy space to $\nabla_{\mathbf{x}} \cdot \mathbf{j}$ in coordinate space.

Leaky box model This model assumes that cosmic rays inside a confinement volume (e.g. the disc) have a constant escape probability per time, $\tau_{\text{esc}} \gg c/h$. Neglecting all other effects,

$$\frac{\partial n_i(E, \mathbf{x})}{\partial t} = -\frac{n_i(E, \mathbf{x})}{\tau_{\text{esc}}} = D\Delta n_i(E, \mathbf{x}), \quad (3.39)$$

and the distribution of cosmic ray path lengths in the disc is $n_i = n_0 \exp(-t/\tau_{\text{esc}}) = n_0 \exp(-z/\lambda_{\text{esc}})$. Hence one can replace

$$D\Delta n_i(E, \mathbf{x}) \rightarrow -\frac{n_i(E, \mathbf{x})}{\tau_{\text{esc}}} \quad (3.40)$$

in this model. Physically, the diffusion coefficient is a function of the distance to the disc, $D = D(z)$, and the escape probability increases and the cosmic ray density decreases for increasing $|z|$, while in the leaky box model both are constant inside the confinement volume. Therefore, the leaky box model can describe only average values of observables that depend in general on z and care has to be taken comparing quantities calculated within the two different models.

If we consider now the steady-state solution, $\partial n_i/\partial t = 0$, and replace the diffusion term by n_i/τ_{esc} , then

$$\frac{n_i(E)}{\tau_{\text{esc}}} = Q_i - \left(\frac{c\rho}{\lambda_i} + \frac{1}{\Gamma\tau_{1/2}} \right) n_i(E) + \sum_k \int_E^\infty dE' \frac{d\sigma_{ki}(E', E)}{dE} n_k(E'). \quad (3.41)$$

For primary types like protons or iron, the decay term vanishes and production via fragmentation can be neglected. Introducing $\lambda_{\text{esc}} = \beta c\rho\tau_{\text{esc}}$ as the amount of matter traversed by a particle with velocity βc before escaping, we obtain

$$n_i = \frac{Q_i\tau_{\text{esc}}}{1 + \lambda_{\text{esc}}/\lambda_i}. \quad (3.42)$$

The escape time τ_{esc} in the leaky-box model should be, similar to D in the diffusion model, energy dependent. For the simplest hypothesis that $\tau_{\text{esc}}(E)$ of different elements depends only on Z , one obtains from a fit to data

$$\lambda_{\text{esc}} \approx 11 \frac{\text{g}}{\text{cm}^2} \left(\frac{4Z\text{GeV}}{p} \right)^\delta \quad \text{for } p \geq 4Z\text{GeV} \quad (3.43)$$

with $\delta \approx 0.6$ and $\lambda_{\text{esc}} = \text{const.}$ at lower energies.

For protons, $\lambda_p = 55 \text{ g/cm}^2 \gg \lambda_{\text{esc}}$ for all energies, and thus

$$n_p = Q_p\tau_{\text{esc}} \propto Q_p E^{-\delta}. \quad (3.44)$$

Hence the generation spectrum of protons should be steeper than the one observed, $Q_p \propto E^{-2.7+\delta} = E^{-2.1}$.

For the other extreme case, iron, the interaction length is $\lambda_{\text{Fe}} = 2.6 \text{ g/cm}^2$. Hence at low energies, iron nuclei are destroyed by interactions before they escape, $\lambda_{\text{Fe}} \ll \lambda_{\text{esc}}$, and therefore the iron spectrum reflects the generation spectrum, $n_{\text{Fe}} \propto Q_{\text{Fe}}$. Starting from the energy where $\lambda_{\text{Fe}} \sim \lambda_{\text{esc}}$, the iron spectrum should become steeper. The observed iron spectrum is indeed flatter at low energies and steepens in the TeV range.

A main test for propagation models are radioactive isotopes with life-time $\tau_{1/2} \sim \tau_{\text{esc}}$. The abundance of such isotopes, e.g. ^{10}Be with $\tau_{1/2} = 3.9 \times 10^6 \text{ yr}$, can be used to deduce separately τ_{esc} and the density of gas. One finds as mean density of the traversed gas $n \sim 0.3/\text{cm}^3$, i.e. just one third of the value in the disc, supporting the idea that cosmic rays are confined not only within the disc but in an extended halo.

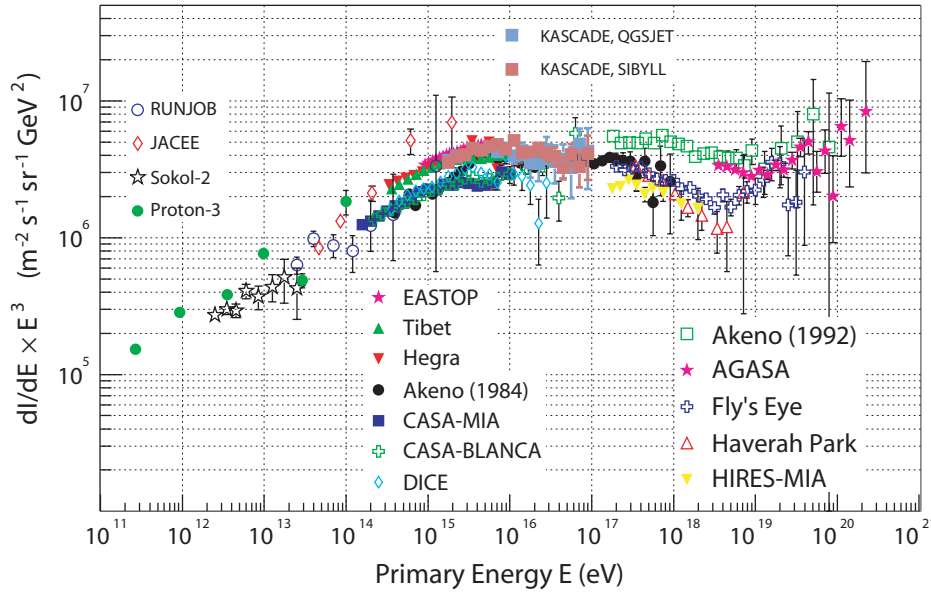


Figure 3.7: The cosmic ray intensity in the knee region [9].

Knee The knee marks a break in the cosmic ray spectrum at $E \sim 3 \times 10^{15}$ eV. There are three classes of explanations: (i) a break in the diffusion coefficient as function of energy, (ii) a signature of the E_{\max} distribution of sources, (iii) a change in the interactions of cosmic rays in the atmosphere at $\sqrt{s} \sim \text{few TeV}$. The possibilities (i) and (ii) produce both a rigidity-dependent knee, i.e. the position of the knee for different nuclei should be connected by $E_Z = ZE_p$, while for (iii) the position of the knee depends on A .

Experimentally, a rigidity-dependent knee is favored as it is visible from Fig. 3.8. The energy of the knee agrees roughly with the critical energy, when the Larmor radius of a proton becomes equal to the maximal length of magnetic field domains. Thus the knee might correspond to a transition from $D \propto E$ to $D \propto E^2$, or more generally to an increased leakage of cosmic rays out of the galaxy.

3.3 Exercises

1. Derive the solution of Eqs. (3.22) and that the observed ratio 0.25 is reproduced for $X \approx 4.3 \text{ g/cm}^2$.
2. Show that the diffusion equation with a point source at $r = 0$ and a space-independent diffusion coefficient has the solution $n(E, r) = 1/(4\pi r)[Q(E)/D(E)]$.

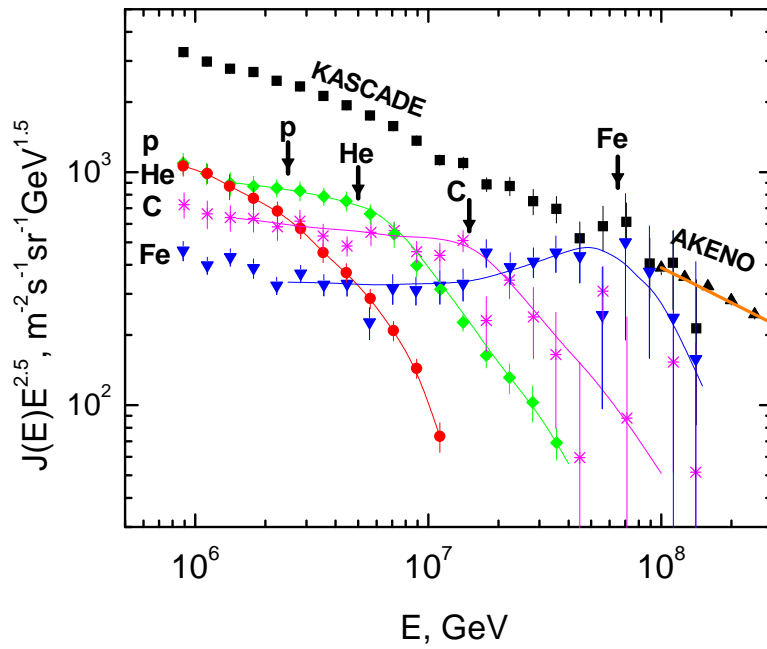


Figure 3.8: The chemical composition measured by the KASCADE experiment in the knee region. Additionally, the position of a rigidity-dependent knee is for p, He, C and Fe indicated [10].

4 Sources and acceleration of high energy cosmic rays

4.1 Sources of high energy cosmic rays

The changes in the slope of the energy spectrum and in the composition from protons to iron in the knee region suggest that there are at least two different kinds of cosmic ray sources. It is natural to associate the bulk of cosmic rays with Galactic sources, while the highest energy cosmic rays have an extragalactic origin, produced by more powerful galaxies than ours. A further argument favoring an extragalactic origin of cosmic rays with the highest energies is the observed isotropy of their arrival directions on large scales that suggests a cosmological distribution of their sources.

4.1.1 General arguments

Energy argument favoring supernova remnants (SNR) The luminosity L_{CR} of Galactic cosmic ray sources has to fit the observed energy density $\rho_{\text{CR}} \sim 1 \text{ eV/cm}^3$ of cosmic rays, taking into account their residence time $\tau_{\text{esc}} \sim 6 \times 10^6 \text{ yr}$ in the Galactic disk. With $V_D = \pi R^2 h \sim 4 \times 10^{66} \text{ cm}^3$ for $R = 15 \text{ kpc}$ and $h = 200 \text{ pc}$ as volume of the Galactic disc, the required luminosity is $L_{\text{CR}} = V_D \rho_{\text{CR}} / \tau_{\text{esc}} \sim 5 \times 10^{40} \text{ erg/s}$.

In a successful core-collapse supernova (SN) around $10 M_{\odot}$ are ejected with $v \sim 5 \times 10^8 \text{ cm/s}$. Assuming $1/(30 \text{ yr})$ as SN rate in the Milky Way, the average output in kinetic energy of Galactic SNe is $L_{\text{SN,kin}} \sim 3 \times 10^{42} \text{ erg/s}$. Hence, if the remnants of SNe can accelerate particle with efficiency $O(0.01)$, they could explain all galactic cosmic rays as it was suggested first by Ginzburg and Syrovatskii in the early 1960s.

Hillas argument The Larmor orbit $R_L = E/(ZeB)$ of accelerated particles has to fit inside the accelerator of size R_s , $R_L = E/(ZeB) \leq R_s$. For known magnetic fields and source sizes, one can constrain thus the maximal achievable energy as $E_{\text{max}} = \Gamma ZeBR_s$, as it is done in Fig. 4.1 for a compilation of potential cosmic ray sources. The Lorentz factor Γ introduced in E_{max} accounts for a possible relativistic bulk motion of the source and is probably only for gamma ray bursts a significant correction. In Fig. 4.1, a so-called ‘‘Hillas plot,’’ sources able to accelerate protons to $E > 10^{21} \text{ eV}$ should lie above the solid red line, while sources above the green line can accelerate iron up to 10^{20} eV . Few candidate sources for acceleration to $E = 10^{21} \text{ eV}$ seem to be compatible with Hillas’ argument.

On one hand, this constraint looks like a solid upper limit, because energy losses are neglected, the maximal acceleration time is finite and no accelerator is 100% efficient. On the other hand, nonlinear processes may lead to an amplification of magnetic fields inside the source. In general, sources neither too small (minimizing energy losses) nor too big (avoiding too long acceleration times) are favored.

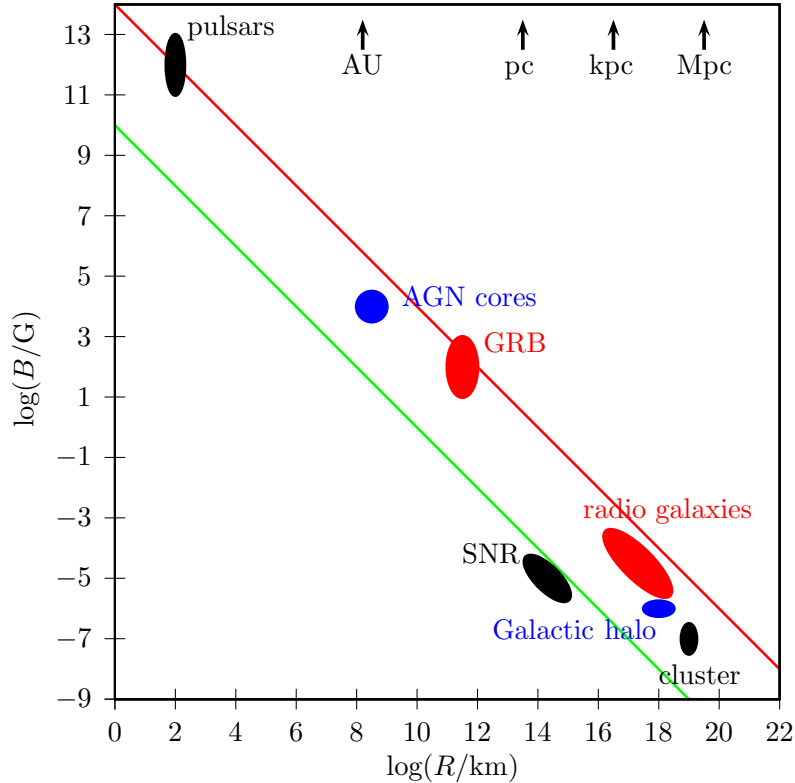


Figure 4.1: Magnetic field strength versus size of various suggested cosmic ray sources.

Blandford argument The acceleration of a proton to the energy $E = 10^{20}$ eV by regular electromagnetic fields requires the potential difference $U = 10^{20}$ V. What is the minimal power P dissipated by such an accelerator? In order to use the basic equation $P = UI = U^2/R$ known from high-school physics, we have to know the appropriate value of the resistance R . Since the acceleration region is in most cases nearly empty, we use $R \sim 1000 \Omega$ (lead by the “impedance of the vacuum”, $R = 4\pi k_0/c = 1/(\epsilon_0 c) \approx 377 \Omega$). Hence a source able to produce protons with $E = 10^{20}$ eV by regular acceleration in electromagnetic fields has the minimal luminosity [12]

$$L = U^2/R \gtrsim 10^{37} \text{ W} = 10^{44} \text{ erg/s}. \quad (4.1)$$

This can be transformed into an upper limit on the density n_s of ultrahigh energy cosmic rays (UHECR) sources, since the observed UHECR intensity fixes the required emissivity \mathcal{L} , i.e. the energy input per volume and time, as $\mathcal{L} \sim 3 \times 10^{46} \text{ erg}/(\text{Mpc}^3 \text{ yr})$. Hence, the density of UHECR sources able to accelerate protons to $E = 10^{20}$ eV should be smaller than $n_s = \mathcal{L}/L \sim 10^{-5}/\text{Mpc}^3$, if the acceleration is by regular electromagnetic fields. For comparison, the density of normal galaxies is $n_s \approx 10^{-2}/\text{Mpc}^3$, while the most common type of active galactic nuclei in the nearby Universe, Seyfert galaxies, has the density $n_s \approx (1 - 5) \times 10^{-5}/\text{Mpc}^3$ within redshift $z \lesssim 0.02$.

4.1.2 Specific sources

Most galactic astrophysical sources are connected with type II (or core-collapse) supernovae (SN) and their remnants (SNR): Examples are the direct acceleration in the magnetosphere of

young pulsars and shock acceleration in SNRs. Above $E \gtrsim 10^{18}$ eV, the signature of galactic sources would be an enhanced flux towards the galactic plane. Practically all extragalactic sources except gamma ray bursts are associated with active galactic nuclei (AGNs).

SNe II Type II or core collapse supernovae occur at the end of the fusion process in very massive stars, $M \gtrsim (5-8)M_{\odot}$. These stars develop an onion-like structure with a degenerate Fe core. After the core is completely fused to iron, no further processes releasing energy are possible. Instead, photo-disintegration destroys the heavy nuclei, e.g. via $\gamma + {}^{56}\text{Fe} \rightarrow {}^4\text{He} + 4n$, and removes the thermal energy necessary to provide pressure support. In the following collapse of the star, the density increases and the free electrons are forced together with protons to form neutrons via inverse beta decay, $e^- + p \rightarrow n + \nu_e$: A proto-neutron star forms. When the core density reaches nuclear density, the equation of state of nuclear matter stiffens and infalling material is “reflected,” a shock wave propagates outwards heated by neutrino emission from the proto-neutron star. If the SN is successful, a neutron star is left over; otherwise a black hole remains.

The released gravitational binding energy,

$$\Delta E = \left[-\frac{GM^2}{R} \right]_{\text{star}} - \left[-\frac{GM^2}{R} \right]_{\text{NS}} \sim 5 \times 10^{53} \text{erg} \left(\frac{10 \text{km}}{R} \right) \left(\frac{M_{\text{NS}}}{1.4M_{\odot}} \right) \quad (4.2)$$

is emitted mainly via neutrinos (99%). Only 1% is transferred into kinetic energy of the exploding star and only 0.01% goes into photons.

Pulsars are the left-over of the former iron core, now transformed into a neutron star with $R_{\text{NS}}/R_{\odot} \sim 10^{-5}$. They may be born fast rotating with a strong magnetic field, because of conservation of

- angular momentum, $L = I\omega = \text{const.}$, with $I \sim MR^2$: A star like the sun, rotating once per month, $P \approx 10^6$ s, would rotate with a ms period when contracted down to 10 km in size.
- magnetic flux, $\phi_B = BA = \text{const.}$, for an ideal conductor, where magnetic field lines are frozen in the plasma. As the core collapses, the magnetic field lines are pulled more closely together, intensifying the magnetic field by a factor $(R_{\odot}/R_{\text{NS}})^2 \sim 10^{10}$. Magnetic A stars have surface fields up to 10^4 G, while the maximal observed field strengths of neutron stars are of the order $B \approx 10^{12}$ G.

Rotating dipole model The energy of a rotating sphere is $E = I\omega^2/2$ and the energy change is

$$\dot{E} = I\omega\dot{\omega}. \quad (4.3)$$

The rotational kinetic energy of the Crab nebula, the remnant of a SN observed by Chinese astronomers in 1054, is $E = \frac{1}{2}I\omega^2 \approx 3 \times 10^{49}$ erg with $I = aMR^2$ and $a \approx 2/5$ for a homogeneous sphere; its energy-loss per time is the time-derivative $\dot{E} = I\omega\dot{\omega} \approx 7 \times 10^{38}$ erg/s, with $I = 1.5 \times 10^{45}$ g cm² and $\dot{\omega} = 4 \times 10^{-4}$ yr⁻¹.

If the energy is lost as electromagnetic dipole radiation, then

$$\dot{E} = -\frac{B^2 R^6 \omega^4 \sin^2 \alpha}{6c^3} \quad (4.4)$$

where α denotes the angle between rotation and dipole axis, and we obtain an estimate for Crab's magnetic field, $B \approx 7 \times 10^{12}$ G for $\sin \alpha = 1$. Thus pulsars have indeed extremely strong magnetic fields that, if they are fast rotating, may accelerate particles to high energies.

Direct acceleration of particles by pulsars The light-cylinder around a pulsar is the surface at $R_c = c/\omega$. If the magnetic field lines would rotate rigidly with the pulsar, then the linear velocity reaches the speed of light, $v = c$, at R_c .

If the magnetosphere is filled sufficiently with plasma, the electric conductivity $\sigma \rightarrow \infty$, and Ohm's law $J = \sigma(E + vB/c)$ implies

$$\mathbf{E} = -\mathbf{v} \times \mathbf{B}/c, \quad (4.5)$$

where $\mathbf{v} = \omega \times \mathbf{r}$.

For a magnetic dipole field pointing along $\vartheta = 0$,

$$\mathbf{B}(r) = \frac{B_0 R^3}{r^3} (2e_r \cos \vartheta + e_\vartheta \sin \vartheta), \quad (4.6)$$

the potential difference between the polar cap and infinity follows as

$$\Delta\phi = \int \mathbf{E} \cdot d\mathbf{s} = -\frac{1}{c} \int \mathbf{v} \times \mathbf{B} \cdot d\mathbf{s} = \frac{B_0 R^2 \omega}{c} \sin^2 \vartheta. \quad (4.7)$$

Open field lines that extend beyond the light cylinder c/ω start near the polar cap, within the cone $\vartheta_0 \sim \sqrt{\omega R/c}$. Inserting ϑ_0 into Eq. (4.7) we obtain as maximal acceleration energy achievable by a pulsar

$$E_{\max} \approx \frac{Z B_0 R^2 \omega \sin^2 \vartheta_0}{c} \approx \frac{Z B_0 R^3 \omega^2}{c^2} \approx 8 \times 10^{20} \text{ eV} \frac{Z B}{10^{13} \text{ G}} \left(\frac{\Omega}{3000 \text{ s}^{-1}} \right)^2. \quad (4.8)$$

Thus a young, fast rotating pulsar appears to be a very good particle accelerator. The main problems are that in realistic models the potential difference $\Delta\phi$ that can be used for particle acceleration is much smaller and the extreme energy losses due to, e.g. curvature radiation. The magnetosphere of a pulsar may be also filled by $\gamma \rightarrow e^+e^-$ with a plasma. Finally, pulsars as main source of UHECRs would predict a strong anisotropy of the UHECR intensity, because neutron stars are concentrated in the Galactic plane.

Shock acceleration in SN remnants is the standard paradigm for cosmic ray acceleration up to $E \sim 10^{15} - 10^{17}$ eV in our galaxy and is discussed in the next section.

Active galaxies is a common name for all galaxies with unusual emission that is not associated with stars. In contrast to normal galaxies whose total luminosity is the sum of the thermal emission from each of the stars found in the galaxy, a large fraction of the total luminosity of an active galaxy is non-thermal and is emitted by the nuclei of the galaxy. The modern view is that the common mechanism behind the energy generation in AGNs is accretion on the SMBH in their center.

Main reason for this view is the fast variability of their spectra, from time-scales of months for quasar spectra down to daily variations for blazars. Causality limits then the size of the emission region as $ct \lesssim 200$ AU. Secondly, the enormous energy output of AGNs requires

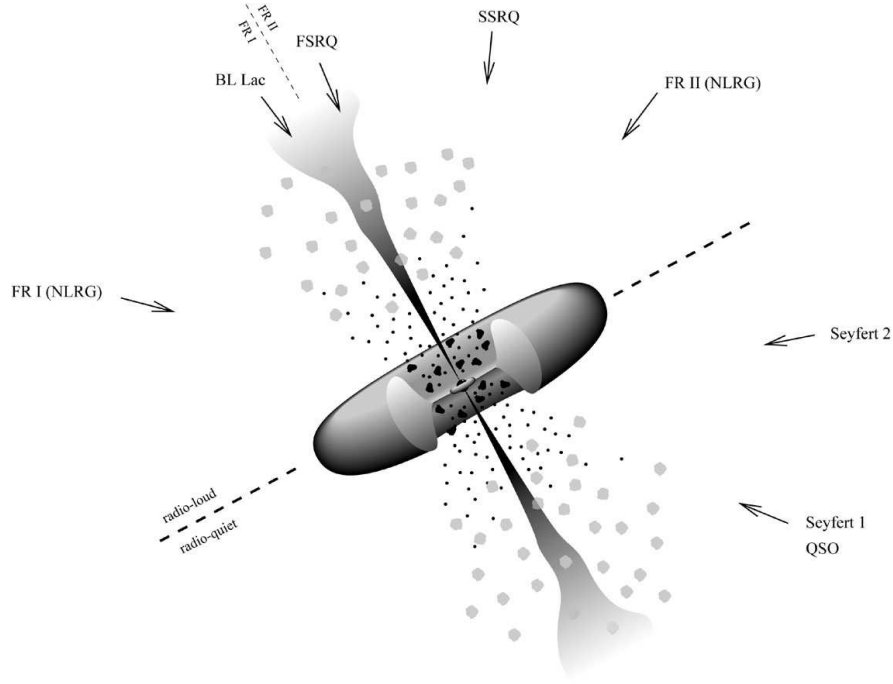


Figure 4.2: The unified scheme of AGN.

an extremely efficient energy generation mechanism. For accretion on a BH, the maximal energy gain is $E_{\max} \sim GmM/R_S$, where the Schwarzschild radius is $R_S = 2GM/c^2$, and thus $E_{\max} = mc^2/2$. A large part of this energy will be lost in the BH, while the remainder heats up via friction an accretion disc around the black hole. Modeling the accretion process gives an efficiency of $\epsilon = 10\%–20\%$. Thus the luminosity from accretion is

$$L = \frac{\epsilon c^2 dm}{2dt}. \quad (4.9)$$

For a rather modest mass consumption of the BH, $dm/dt = 1M_{\odot}/\text{yr}$, one obtains $6 \times 10^{45} \text{erg/s}$ or $L \sim 10^{12} L_{\odot}$.

The unified picture of AGNs is illustrated in Fig. 4.2. The different AGN types are only facets of the same phenomenon—accretion on a SMBH—viewed from different angles, at different stages of activity (small or large dm/dt) and evolution in time (e.g. from a quasar phase at redshift $z \sim 1–4$ towards a Seyfert galaxy at present). Blazars are AGN with a relativistic jet that is pointing in the direction of the Earth and are therefore often ranked among the most promising sources of ultrahigh energy cosmic rays. According Fig. 4.2, blazars are either Flat Spectrum Radio Quasars (FSRQ) or BL Lac objects.

Gamma Ray Bursts come in two (main) sub-varieties, depending on their duration that varies from fraction of a second to many minutes. While short duration GRBs are most likely the result of binary collisions between e.g. neutron stars, long duration GRBs which make up about 2/3 of all GRBs are associated with supernova events in extremely massive stars. GRBs are highly beamed sources of gamma-rays and perhaps also of high energy neutrinos and cosmic rays. A distinctive feature is the high Lorentz factor of shocks in GRBs.

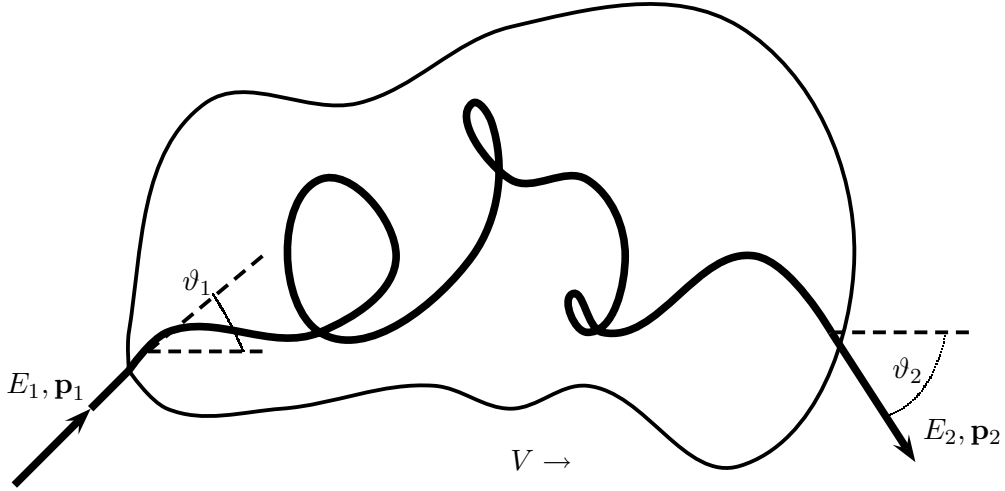


Figure 4.3: A cosmic ray “scattering” elastically at a magnetic cloud moving with velocity V .

4.2 Acceleration of cosmic rays

4.2.1 Second order Fermi acceleration

We consider a cosmic ray with initial energy E_1 “scattering” elastically on a magnetic cloud that moves with velocity $V \ll c$. We want to derive the energy gain $\xi \equiv (E_2 - E_1)/E_1$ per scattering. The variables (E_1, ϑ_1) and (E_2, ϑ_2) are shown in Fig. 4.3, which we label with a prime in the cloud system and without a prime in the lab system.

With a first Lorentz transformation between the lab and cloud system we connect the variables characterizing the cosmic ray entering the cloud,

$$E'_1 = \gamma E_1 (1 - \beta \cos \vartheta_1) \quad \text{where} \quad \beta = V/c \quad \text{and} \quad \gamma = 1/\sqrt{1 - \beta^2}, \quad (4.10)$$

and with a second Lorentz transformation the exit variables,

$$E_2 = \gamma E'_2 (1 + \beta \cos \vartheta'_2). \quad (4.11)$$

Since the scattering off magnetic irregularities is collisionless and the cloud is very massive, energy is conserved, $E'_2 = E'_1$. Hence we can eliminate E'_2 and obtain as relative energy gain

$$\xi = \frac{E_2 - E_1}{E_1} = \frac{1 - \beta \cos \vartheta_1 + \beta \cos \vartheta'_2 - \beta^2 \cos \vartheta_1 \cos \vartheta'_2}{1 - \beta^2} - 1. \quad (4.12)$$

To proceed, we need average values of $\cos \vartheta_1$ and $\cos \vartheta'_2$. Since the cosmic ray scatters off magnetic irregularities many times in the cloud, its exit direction is randomized, $\langle \cos \vartheta'_2 \rangle = 0$. The collision rate of the cosmic ray with the cloud is proportional to their relative velocity $(v - V \cos \vartheta_1)$. For ultrarelativistic particles, $v \rightarrow c$, and the collision rate is

$$\frac{dn}{d\Omega_1} \propto (1 - \beta \cos \vartheta_1). \quad (4.13)$$

We obtain $\langle \cos \vartheta_1 \rangle$ averaging $\cos \vartheta_1$ weighted by $dn/d\Omega_1$ over all angles,

$$\langle \cos \vartheta_1 \rangle = \int \cos \vartheta_1 \frac{dn}{d\Omega_1} d\Omega_1 / \int \frac{dn}{d\Omega_1} d\Omega_1 = -\frac{\beta}{3}. \quad (4.14)$$

Plugging $\langle \cos \vartheta_2 \rangle = 0$ and $\langle \cos \vartheta_1 \rangle = -\beta/3$ into Eq. (4.12) and taking into account that $\beta \ll 1$ gives as average gain

$$\langle \xi \rangle = \frac{1 + \beta^2/3}{1 - \beta^2} - 1 \simeq \frac{4}{3}\beta^2. \quad (4.15)$$

Thus $\langle \xi \rangle \propto \beta^2 > 0$ and we have shown that on average a cosmic ray gains energy scattering on “magnetic clouds” with an ordered bulk velocity V . The energy gain per scattering is however only of second order in the small parameter β , and acceleration is therefore rather inefficient. Moreover, one can show that the resulting energy spectrum would depend strongly on the cloud parameters, making thereby the observed feature-less power spectrum of cosmic rays difficult to understand. Acceleration at shocks that we consider next avoids both disadvantages.

4.2.2 Shock or first order Fermi acceleration

Ideal fluids and shocks As first step in gaining some understanding of shocks we recall the the ideal fluid equations. The three basic equations are the conservation equation for mass, for momentum, and the Poisson equation,

$$\partial_t \rho + \nabla \cdot (\rho \mathbf{v}) = 0, \quad (4.16a)$$

$$\rho \frac{\partial \mathbf{v}}{\partial t} + \rho \mathbf{v} \cdot (\nabla \mathbf{v}) = \mathbf{F} - \nabla P, \quad (4.16b)$$

$$\Delta \phi = 4\pi G \rho. \quad (4.16c)$$

The LHS of (4.16b), the Euler equation, measures the velocity change dv/dt of a fluid element, summing up the change at a fixed coordinate, $\partial_t v$, and the change due to the movement of the element, while the RHS consists of an external force \mathbf{F} and a force due to a pressure gradient ∇P . The Poisson equation connects the mass density ρ with the gravitational potential ϕ .

We consider now small perturbations x_1 around a static background, $\rho_0 = \text{const.}$, $P_0 = \text{const.}$ and $v_0 = 0$. Restricting us to small perturbations, $x_1 \ll x_0$, allows us to neglect all quantities quadratic in the perturbations. Sound waves propagate in most circumstances adiabatically, i.e. without production of entropy, $dS = 0$. Thus changes in P and ρ are connected via

$$P = P_0 + \left(\frac{\partial P}{\partial \rho} \right)_S d\rho + \left(\frac{\partial P}{\partial S} \right)_P dS = P_0 + c_s^2 d\rho. \quad (4.17)$$

Inserting $x = x_0 + x_1$ into the fluid equations and neglecting quadratic term gives

$$\partial_t \rho_1 + \rho_0 \nabla \cdot \mathbf{v}_1 = 0, \quad (4.18a)$$

$$\Delta \phi_1 = 4\pi G \rho_1, \quad (4.18b)$$

$$\partial_t \mathbf{v}_1 + \frac{c_s^2}{\rho_0} \nabla \rho_1 + \nabla \phi_1 = 0, \quad (4.18c)$$

where we used also $\partial_x P = \frac{\partial \rho_1}{\partial x} \frac{\partial}{\partial \rho_1} P_1 = \frac{\partial \rho_1}{\partial x} c_s^2$. These three equations can be combined into one second-order differential equation for ρ_1 . We multiply Eq. (4.18c) by ρ_0 and apply ∇ on it,

$$c_s^2 \Delta \rho_1 = -\rho_0 (\partial_t \nabla \cdot \mathbf{v}_1 + \Delta \phi_1). \quad (4.19)$$

Then we insert (4.18b) for $\Delta \phi_1$ and (4.18a) for $\nabla \cdot \mathbf{v}_1$, and obtain a linear, inhomogeneous wave equation

$$\partial_t^2 \rho_1 - \underbrace{c_s^2 \Delta \rho_1}_{\text{pressure}} = \underbrace{4\pi G \rho_1 \rho_0}_{\text{grav.force}} \quad (4.20)$$

for the density perturbation ρ_1 . The dispersion relation of plane waves $\exp(-i(\omega t - kx))$,

$$\omega^2 = c_s^2 k^2 - 4\pi G \rho_0, \quad (4.21)$$

confirms that $c_s = (\partial P / \partial \rho_1)^{1/2}$ is the sound speed.

For a mono-atomic gas, the equation of state is $P = K \rho^\gamma$ with $\gamma = 5/3$. Thus, the sound speed is $c_s = (\gamma P / \rho)^{1/2}$ and if an adiabatic compression with density $\rho_2 = \varepsilon \rho_1$ propagates, then $c_s \propto \varepsilon^{(\gamma-1)/2}$. Hence the sound speed increases for a compression, the dense region overruns uncompressed regions and becomes even denser: A discontinuity (=”shock”) develops in some hydrodynamical variables like the density.

Mach number of a (strong) shock Our main aim is to derive the Mach number $\mathcal{M} = v/c_s$ of a shock that as we will see determines the slope of the energy spectrum of accelerated particles. We will consider only the properties of an one-dimensional, steady shock in its rest frame and assume that magnetic or gravitational fields can be neglected. Then the continuity equation for mass, $\partial_t \rho + \nabla \cdot (\rho \mathbf{v}) = 0$, becomes simply

$$\frac{d}{dx} (\rho v) = 0. \quad (4.22)$$

The Euler equation simplifies using the same assumptions and taking into account Eq. (4.22) to

$$\frac{d}{dx} (P + \rho v^2) = 0. \quad (4.23)$$

Additionally to the conservation laws for mass (4.22) and momentum (4.23) we need the conservation law for energy,

$$\frac{\partial}{\partial t} \left(\frac{\rho v^2}{2} + \rho U + \rho \Phi \right) + \nabla \cdot \left[\rho \mathbf{v} \left(\frac{v^2}{2} + U + \frac{P}{\rho} + \Phi \right) \right] = 0. \quad (4.24)$$

Here, the first bracket accounts for the change of kinetic, internal and potential energy with time which has to be balanced by the energy flux through the boundary of the considered volume. Specializing again to the case of an one-dimensional, stationary flow with $\Phi = 0$ gives

$$\frac{d}{dx} \left(\frac{\rho v^3}{2} + (U + P)v \right) = 0. \quad (4.25)$$

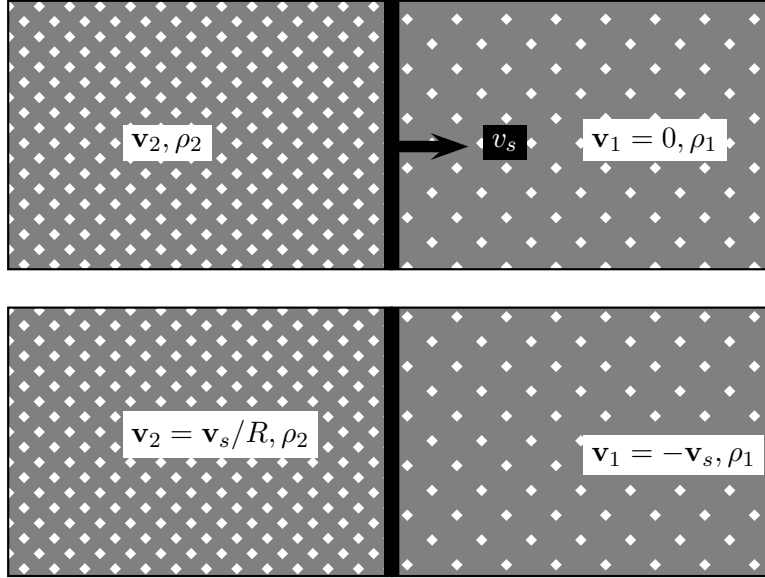


Figure 4.4: Conditions on the down-stream (left) and the up-stream (right) side of a shock in the lab system (top) and in the shock rest frame with $\mathbf{v}_1 = -\mathbf{v}_s$ (bottom).

Integrating these equations over the discontinuity of the shock results in the ‘‘Rankine-Hugoniot’’ jump conditions,

$$[\rho v]_1^2 = 0, \quad (4.26a)$$

$$[P + \rho v^2]_1^2 = 0, \quad (4.26b)$$

$$\left[\frac{\rho v^2}{2} + \frac{\gamma}{\gamma - 1} P v \right]_1^2 = 0, \quad (4.26c)$$

where we used also $U = P/(\gamma - 1)$. Since we assumed a steady flow, these jump conditions have to be evaluated in the shock rest frame, cf. Fig 4.4 – otherwise time-derivatives should be included.

Inserting first $\rho_2 = (v_1/v_2)\rho_1$ into (4.26b) gives $P_2 = P_1 + \rho_1 v_1(v_1 - v_2)$. Next we use these two expressions to eliminate ρ_2 and P_2 from Eq. (4.26c). Reordering the resulting equation according to powers of v_2 ,

$$\left(\frac{\gamma + 1}{\gamma - 1} \right) v_2^2 + \frac{2\gamma}{\gamma - 1} \left(\frac{P_1 + \rho_1 v_1^2}{\rho_1 v_1} \right) v_2 + v_1^2 \frac{2\gamma}{\gamma - 1} \frac{P_1}{\rho_1} = 0, \quad (4.27)$$

replacing P_1 by the sound speed and dividing by v_1^2 , we obtain finally a quadratic equation for $t = v_2/v_1$,

$$\left(\frac{\gamma + 1}{\gamma - 1} \right) t^2 + \frac{2\gamma}{\gamma - 1} \left(\frac{c_1^2}{v_1^2} + \gamma \right) t + \left(1 + \frac{2}{\gamma - 1} \frac{c_1^2}{v_1^2} \right) = 0. \quad (4.28)$$

Now we recognize v_1/c_1 as the Mach number \mathcal{M} . Since we are interested in fast flows, $v_1 \gg c_1$, we can neglect the two $1/\mathcal{M}^2$ terms and obtain as approximate solutions

$$t = 1 \quad \text{or} \quad v_1 = v_2, \quad (4.29a)$$

$$t = \frac{\gamma - 1}{\gamma + 1} \equiv R \quad \text{or} \quad Rv_2 = v_1. \quad (4.29b)$$

The first solution is obviously trivial, while the second one is the strong shock solution. The compression ratio R indicates how strong the density and the velocity in the up- and down stream regions differ. Since we are using as reference frame the shock frame, we have $v_s = v_1$ and thus for $\gamma = 5/3$ and $R = 4$,

$$v_2 = v_s/R = v_s/4, \quad (4.30a)$$

$$\rho_2 = R\rho_1 = 4\rho_1, \quad (4.30b)$$

$$P_2 = 3\rho_1 v_s^2/4. \quad (4.30c)$$

Hence no matter how strong a shock is, it can compress a mono-atomic gas only by a factor four. The same factor relates the velocity of the shock and of the matter after the passage of the shock. It is this universal ratio of the up- and down-stream velocities for any strong shock that results in the generic prediction of an $1/E^2$ spectrum produced by acceleration at shocks.

Acceleration at shocks We consider again a cosmic ray with initial energy E_1 “scattering” at magnetic irregularities that are now separated by a planar shock moving with velocity v_s . The only change to the previous discussion are the resulting different angular averages. The (normalized) crossing rate is given by the projection of an isotropic flux on the planar shock,

$$\frac{dn}{d \cos \vartheta_1} = \begin{cases} 2 \cos \vartheta_1 & \cos \vartheta_1 < 0 \\ 0 & \cos \vartheta_1 > 0 \end{cases}. \quad (4.31)$$

while the crossing rate $dn/d \cos \vartheta_2$ is non-zero for $\cos \vartheta_2 > 0$. Thus $\langle \cos \vartheta_1 \rangle = -\frac{2}{3}$ and $\langle \cos \vartheta_2 \rangle = \frac{2}{3}$ and hence

$$\langle \xi \rangle \approx \frac{4}{3}\beta = \frac{4}{3} \frac{v_1 - v_2}{c}. \quad (4.32)$$

The average gain $\langle \xi \rangle$ is now linear in β and justifies the name “first-order” Fermi (or shock) acceleration.

Energy spectrum produced by Fermi acceleration The energy E_n of a cosmic ray after n acceleration cycles is

$$E_n = E_0(1 + \xi)^n \quad (4.33)$$

and the number of cycles needed to reach E_n is thus

$$n = \ln \left(\frac{E_n}{E_0} \right) / \ln (1 + \xi). \quad (4.34)$$

If the escape probability p_{esc} per encounter is constant, then the probability to stay in the acceleration region after n encounters is $(1 - p_{\text{esc}})^n$. We obtain the fraction f of particles with energy $> E_n$ as

$$f(> E) = \sum_{m=n}^{\infty} (1 - p_{\text{esc}})^m = \frac{(1 - p_{\text{esc}})^n}{p_{\text{esc}}} \propto \frac{1}{p_{\text{esc}}} \left(\frac{E}{E_0} \right)^{\gamma}, \quad (4.35)$$

where

$$\gamma = \ln \left(\frac{1}{1 - p_{\text{esc}}} \right) / \ln(1 + \xi) \approx p_{\text{esc}}/\xi \quad (4.36)$$

with $\xi \ll 1$ and $p_{\text{esc}} \ll 1$. Hence, both first and second order Fermi acceleration produces a power-law energy spectrum.

The maximal energy achievable by a specific source is determined by several factors. First, the finite life-time limits the number of cycles n and thus E_n . Second, the escape probability is energy dependent and increases generally for increasing energy. Third, energy losses like synchrotron radiation increase with energy and balance at a certain point the energy gain.

Exponent γ for shock acceleration Since we know already that $\xi \approx \frac{4}{3}\beta = \frac{4}{3}\frac{v_1 - v_2}{c}$, we have to determine only the escape probability p_{esc} in order to estimate the exponent $\gamma \approx p_{\text{esc}}/\xi$ of the integral spectrum produced by shock acceleration. The particle flux \mathcal{F} through an infinite, planar shock front is (cf. Eq.(3.2))

$$\mathcal{F}(E) = \pi I(E) = \frac{cn(E)}{4}, \quad (4.37)$$

assuming $v_s \ll c$ and an efficient isotropization of cosmic rays up-stream.

In the shock rest frame, there is a particle flow $\mathcal{F}_{\text{esc}}(E) = v_2 n(E)$ downstream away from the shock front that will be lost for the acceleration process. Thus the escape probability p_{esc} as the ratio of the loss and the crossing flux is

$$p_{\text{esc}} = \frac{\mathcal{F}_{\text{esc}}}{\mathcal{F}} = \frac{v_2 n}{cn/4} = \frac{4v_2}{c} \quad (4.38)$$

and the spectral index of the integral energy spectrum follows as

$$\gamma \approx p_{\text{esc}}/\xi \approx \frac{3}{v_1/v_2 - 1}. \quad (4.39)$$

Typical values for the sound speed in the interstellar medium around a SNR are $c_1 \sim 10$ km/s, while the shock velocities are $v_1 \sim 10^4$ km/s. Thus the Mach number $\mathcal{M} = v_1/c_1 \gg 1$ and we can use the result $v_1 = 4v_2$ in the strong shock limit. The exponent predicted by Fermi acceleration at non-relativistic shock is therefore independent of the shock parameters and agrees with the value needed to explain the spectrum of Galactic cosmic rays. These are the two main reasons for the popularity of shock acceleration.

We can check that possible corrections are small by solving Eq. (4.28) for arbitrary \mathcal{M} . Then we obtain $R = 4\mathcal{M}^2/(3 + \mathcal{M}^2)$ and thus

$$\gamma \approx \frac{3 + \mathcal{M}^2}{\mathcal{M}^2 - 1} \approx 1 + \frac{1}{4\mathcal{M}^2} + \mathcal{O}(\mathcal{M}^{-4}). \quad (4.40)$$

Clearly, other effects like energy losses or an energy dependence of p_{esc} will have a larger impact on the resulting spectrum than the $\mathcal{O}(\mathcal{M}^{-2})$ corrections. Moreover, we worked within an extremely simplified picture and should expect therefore deviations from a power-law with $\gamma \sim 1$. For instance, we used the test particle approach that neglects the influence of cosmic rays on the plasma.

Finally we remark that the observed flux from extragalactic sources might require a steeper injection spectrum than $\gamma \sim 1$, and that the acceleration mechanism responsible for cosmic rays beyond $\sim 10^{18}$ eV is still open. A discussion of more recent developments in the understanding of cosmic ray acceleration can be found in Ref. [13].

5 Gamma-ray astronomy

5.1 Experiments and detection methods

The Earth's atmosphere is opaque to photons with energy above 10 eV, meaning that to observe gamma rays directly requires placement of a detector above the earth atmosphere. A major turning point in gamma-ray astronomy was therefore the launch of the first satellite-borne telescope, SAS-2, in 1972.

The heretofore most successful gamma-ray satellite was the Compton Gamma Ray Observatory, taking data from 1991–2000 with its four different experiments. Some of the main results were the proof that a large fraction of gamma ray bursts are isotropically distributed and thus extragalactic in origin, the detection of discrete sources of extragalactic γ -ray emission, and an upper limit on the diffuse extragalactic γ -ray background. A new satellite experiment, GLAST, will be launched 2008.

Main limitation of satellite experiments is their small collection area, which limits their use to energies $\lesssim 100$ GeV. On the other hand, 100 GeV is the limit where the electromagnetic cascade in the earth's atmosphere from the initial photon can be detected. While the cascade dies out high in the atmosphere below 10 TeV, showers are still detectable via the Cherenkov emission of relativistic electrons and muons. The main difficulty in ground-based gamma-ray astronomy is the presence of an almost overwhelming background of charged cosmic rays.

Discrimination The image of an air shower in an atmospheric Cherenkov telescope can be modeled as a two-dimensional ellipse. The two main parameters that distinguish an air shower initiated by a photon and a proton are the length and the width of this ellipse: While a photon shower is narrow with a long elongation, a proton shower of comparable energy is much wider and shorter, cf. Fig. 5.1. The resulting discrimination power would be not sufficient to separate photons from the cosmic ray background, if photon sources like e.g. blazars would not appear point-like.

5.2 Electromagnetic processes

5.2.1 Synchrotron radiation

The power P of emitted synchrotron radiation by a particle with mass m , charge e and momentum p_{\perp} perpendicular to the magnetic field is in the classical limit

$$P_{\text{cl}} = \frac{2}{3} \alpha m^2 \left(\frac{p_{\perp} e B}{m m^2} \right)^2 = \frac{2}{3} \alpha m^2 \left(\frac{p_{\perp} B}{m B_{\text{cr}}} \right)^2. \quad (5.1)$$

The energy loss per time is $\beta = dE/dt = -P \propto m^{-4}$ and hence is most severe for the lightest charged particle, the electron. The typical length-scale l_{syn} of synchrotron losses

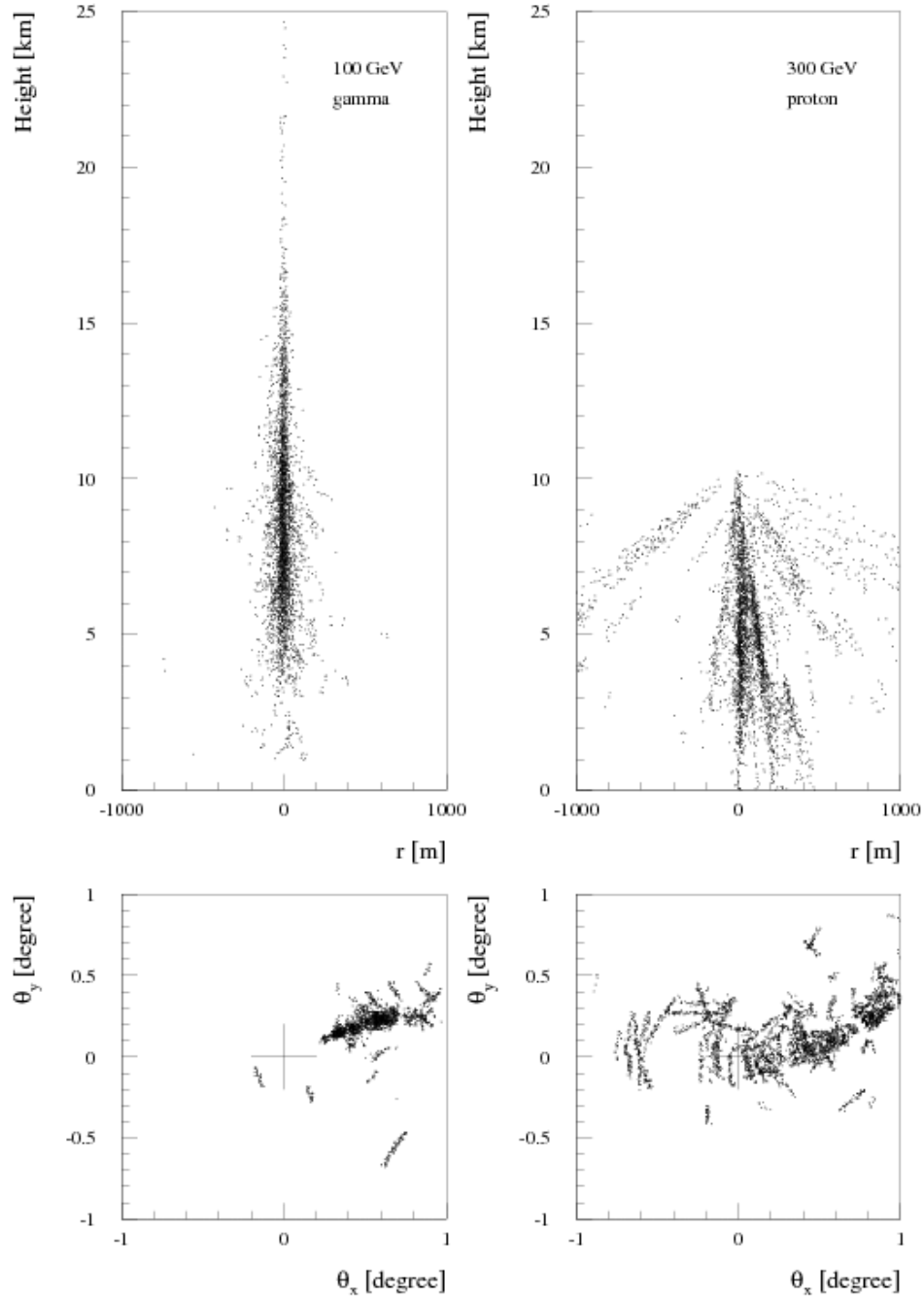


Figure 5.1: The longitudinal development (top) and the projection (bottom) of a shower initiated by a photon (left) and by a proton (right) [11].

($B_{\text{cr}} = m_e^2/e = 4.41 \times 10^{13}$ G is the critical field strength for an electron)

$$l_{\text{syn}} = \left(\frac{1}{E} \frac{dE}{dt} \right)^{-1} = \frac{3}{2\alpha m} \frac{1}{\gamma} \left(\frac{B_{\text{cr}}}{B} \right)^2. \quad (5.2)$$

For electrons with $E = 10^{15}$ eV in the Galactic disc, $B \sim 3\mu\text{G}$, we have $l_{\text{syn}} \sim 100$ pc. Thus one of the reasons why we have not discussed electrons as a major component of cosmic rays is that their energy losses are too severe. On the other side, synchrotron radiation of relativistic electrons is in the radio range and explains the strong radio emission of many AGNs: Synchrotron radiation peaks at $0.29\omega_c$ with

$$\omega_c = \frac{3\gamma^2 B}{2B_{\text{cr}}} m. \quad (5.3)$$

For $B \sim 0.1$ G close to a source and $\gamma = 10^9$, the peak of synchrotron radiation is at $10^{-10}m_e \sim 100$ GHz. Synchrotron radiation is the explanation of the first peak visible in Fig. 5.2, showing the observed spectrum from a Blazar.

5.2.2 (Inverse) Compton scattering

The cross section for Compton scattering $e^- + \gamma \rightarrow e^- + \gamma$ is with $\sigma_{\text{Th}} = 8\pi\alpha^2/(3m_e^2)$

$$\sigma = \sigma_{\text{Th}} \left(1 - s/m^2 + \dots \right) \quad \text{for } s/m^2 \ll 1 \quad (5.4)$$

$$\sigma = \frac{3m^2}{4s} \sigma_{\text{Th}} \left(\ln s/m^2 + \frac{1}{2} + \dots \right) \quad \text{for } s/m^2 \gg 1 \quad (5.5)$$

i.e. Compton scattering is suppressed for $s \gg m^2$.

While in the classical Compton experiment an energetic photon hits an electron at rest and transfers part of its energy, in astrophysics “Inverse Compton scattering” is more important: A fast electron hitting a low-energy photon transfers a large fraction y of its energy to the photon,

$$y \approx 1/\ln(s/m_e^2). \quad (5.6)$$

This is the explanation of the second peak visible in Fig. 5.2, showing the observed spectrum from a blazar.

5.3 Hadronic processes

Neutral pion decay $\pi^0 \rightarrow 2\gamma$ In the rest system of the π^0 , the two photons are emitted back-to-back, $\mathbf{p}_1 = -\mathbf{p}_2$ and $E_1 = E_2 = m_\pi/2$. How are the photon energies distributed, if the pion was moving with velocity v ?

Let us use the Lorentz transformation between energies in the rest and the lab system. In the lab system,

$$E = \gamma(E' + \beta p' \cos \vartheta) \quad (5.7)$$

where ϑ is the angle between the velocity β of the pion and the emitted photon. The maximal/minimal values of E follow directly as $E = \gamma(E' \pm \beta p')$ for $\cos \vartheta = \pm 1$, i.e. if the photons are emitted parallel and anti-parallel to the direction of flight of the pion.

Inserting $E' = p' = m_\pi/2$ gives

$$E_{\min}^{\max} = \frac{1}{2} (\gamma m_\pi \pm \beta \gamma m_\pi) = \frac{1}{2} E_\pi (1 \pm \beta) \quad (5.8)$$

or $E_{\max} \rightarrow E_\pi$ and $E_{\min} \rightarrow 0$ in the ultra-relativistic limit $\beta \rightarrow 1$.

What is the distribution of the emitted photons? Since the pion is a scalar particle, the photon distribution is isotropic in the lab system,

$$dN = \frac{1}{4\pi} d\Omega = \frac{1}{2} d|\cos \vartheta|. \quad (5.9)$$

Using (5.7), one can express dE as $\gamma\beta p' d|\cos \vartheta|$ and thus

$$dN = \frac{1}{4\pi} d\Omega = \frac{dE}{2\gamma p'}. \quad (5.10)$$

Hence $dN/dE = \text{const.}$, and the photon spectrum produced by a pion beam with uniform velocity is a box between E_{\min} and E_{\max} from Eq. (5.8). If we use $\log(E)$ as x coordinate, the boxes are symmetric with respect to $m_\pi/2$.

Photon spectrum from “many pion decays” Consider now the photon spectrum not from a single pion, but from a beam of pions with arbitrary energy spectrum. Each photon spectrum from a single decay is as we saw a box centered at $m_\pi/2$. Hence also the total photon spectrum from pions with an arbitrary energy distribution is symmetric with respect to $m_\pi/2$.

5.4 Source models

The energy spectrum observed from blazars, i.e. AGN which jets are pointing towards us, covers all the electromagnetic spectrum from radio frequencies up to TeV energies. It is characterized by two bumps, cf. Fig. 5.2, one peaking between the IR and the X-ray band, another one at gamma-ray energies. The first peak can be explained as synchrotron radiation from relativistic electron, while the second one is presumably due to inverse Compton scattering – between the same electrons and either soft photons or synchrotron photons.

Although sources like blazars should accelerate not only electrons but also protons, synchrotron radiation and inverse Compton scattering of electrons are sufficient to explain in most cases the observed spectra. There are only few exceptions where an additional photon component from pion decay at the highest energies might be needed.

The proof that a source accelerates indeed protons might be easier for Galactic sources, where the source region can be resolved by modern atmospheric Cherenkov telescopes. An example is the recent observation of the SNR RX J1713.7-3946 by the HESS array that has been interpreted as the first direct evidence that SNRs accelerate cosmic rays up to TeVs [14]. The image of this source shows an increase of TeV photons in the directions of known molecular clouds. This is in line with the expectation that, if photons are produced as secondaries in pp collisions, their flux is correlated with the matter density in the SNR.

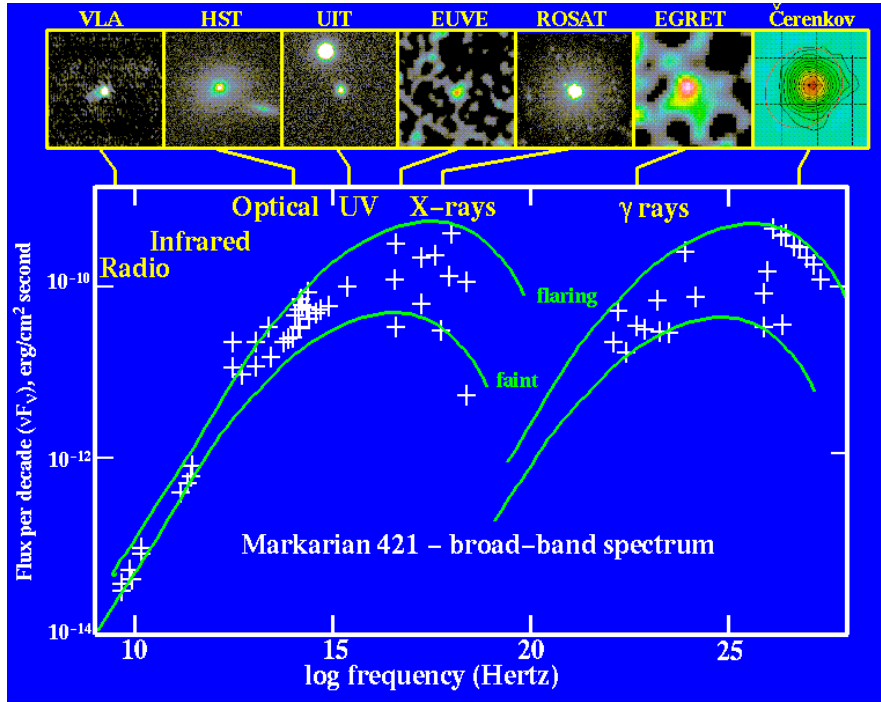


Figure 5.2: Spectrum from the blazar Markarian 421 in a flaring and a quiet state [15].

5.5 Electromagnetic cascades

A high energy particle interacts at the top of the atmosphere and initiates a cascade. In the 1930's, it was recognized that the observed cosmic rays on ground are only the secondaries produced in this cascade. Heitler introduced the following simple toy model of an electromagnetic cascade:

- In each interaction characterized by the constant interaction length λ , a parent particle splits into two daughter particles. Each particle takes half of the energy.
- After $n = X/\lambda$ generations, the cascade consists of $N(X) = 2^{X/\lambda}$ particles.
- The energy per particle is $E(X) = E_0/N$, where E_0 is the energy of the primary.
- Particle production stops, when $E(X) < E_{\text{cr}} \sim 0.1 \text{ GeV}$. Below this energy, photons lose energy mainly by ionization losses. Unstable particles decay and the number of particles in the shower decreases.

The number of particles at the shower maximum X_{max} is

$$N(X_{\text{max}}) = \frac{E_0}{E_{\text{cr}}} \quad \text{with} \quad X_{\text{max}} = \frac{\lambda}{\ln 2} \ln \frac{E_0}{E_{\text{cr}}}. \quad (5.11)$$

Thus the energy E_0 of the primary particle is connected via

$$N(X_{\text{max}}) \propto E_0 \quad \text{and} \quad X_{\text{max}} \propto \ln E_0 \quad (5.12)$$

to measurable quantities. Note that E_{cr} —the quantity that mainly controls $N(X_{\text{max}})$ —is determined by well-known low energy processes.

Cascade equations and scaling The cascade equation for electron ($= e^+, e^-$) and photons are

$$\frac{\partial N_i(E, r)}{\partial r} = -n\sigma_{i,\text{tot}}(E)N_i(E, r) + n \int_E^\infty dE' \frac{d\sigma_{ki}(E', E)}{dE} N_k(E', r) \quad (5.13)$$

where $i = e, \gamma$. Two possible boundary conditions are

$$N_i(E, 0) = \delta(E - E_0), \quad (5.14a)$$

$$N_i(E, 0) = KE^{-\alpha}, \quad (5.14b)$$

i.e. the study of a single shower or the general properties of electromagnetic cascades. We consider next only one species (i.e. we are not interested which particles are produced in the interactions) and the simpler second case for the boundary condition. Under which conditions may we hope for an analytical solution? The energy and depth dependence should factorize, $N(E, r) = g(E)f(r)$, i.e. the shower should have at each depth the same energy dependence. This happens, if (i) the cross sections are not energy dependent, and (ii) the differential cross sections scale,

$$f(z) = \frac{1}{\sigma} \frac{d\sigma}{dz} = \frac{E'}{\sigma} \frac{d\sigma(E', E)}{dE} \quad (5.15)$$

with $z = E/E'$. Then, we can rewrite $N(E', r) = KE'^{-\alpha} = Kz^\alpha E^{-\alpha}$ for boundary condition (b) and it follows

$$N(E, r) = N(E, 0) \exp[-n\sigma r(1 - Z(\alpha))] \quad (5.16)$$

with the spectrally averaged energy loss fraction

$$Z(\alpha) = \int_0^1 dz z^{\alpha-1} f(z). \quad (5.17)$$

Equation (5.16) is straightforward to interpret: For $z \rightarrow 0$, one obtains the limiting case of full absorption, while interactions without energy transfer do not change $N(E, r)$ at all. In the intermediate case, Eq. (5.17) weights the energy loss z properly not only with $f(z)$ but also with the spectral shape $N(E) \propto E^{-\alpha}$.

For a steeply falling spectra, $\alpha > 1$, the region $z \rightarrow 1$ gives the dominating contribution to the integral defining $Z(\alpha)$. This illustrates that for the modeling of air shower the knowledge of cross sections in the “forward” region $z \rightarrow 1$ is crucial.

5.5.1 Cascades in the atmosphere

Probabilities The differential probability $P(z)$ for an electron with energy E scattering on an atomic nucleus to emit a photon with energy zE traversing the depth $dt = dX/X_0$ is in the high energy limit

$$P_{e\gamma}(z) = z + \frac{1-z}{z} \left(\frac{4}{3} + 2b \right), \quad (5.18)$$

where $b = b(Z) \approx 0.012$ depends on the average charge Ze of air. This process is infrared-divergent, i.e. the probability to emit a soft photon diverges, $P_{e\gamma}(z) \rightarrow \infty$ for $z \rightarrow 0$. Only if we consider the energy loss rate,

$$\frac{dE}{dX} = -\frac{1}{X_0} \int_0^1 dz zE P_{e\gamma}(z) = -\frac{E(1+b)}{X_0} \approx -\frac{E}{X_0}, \quad (5.19)$$

we obtain a finite result. By contrast, the probability for the pair production of a massive e^+e^- pair in the Coulomb field of a nucleus is infrared-finite,

$$P_{\gamma e}(z) = \frac{2}{3} - \frac{1}{2}b + \left(\frac{4}{3} + 2b\right) \left(z - \frac{1}{2}\right)^2, \quad (5.20)$$

and can be integrated to

$$\frac{1}{\Lambda_{\text{pair}}} = \int_0^1 dz P_{\gamma e}(z) = \frac{7}{9} - \frac{b}{3} \approx \frac{7}{9}. \quad (5.21)$$

Both electrons and photons lose their energy exponentially, $E(X) = E_0 \exp(-X/X_0)$, with the radiation length $X_0 \approx 37.2\text{g/cm}^2$ (in air) and $7X_0/9$ as scales, respectively. Below the critical energy $E_{\text{cr}} \approx 84.2$ MeV, ionization losses become more important than pair production and the growth of the cascade stops.

Shower profile in the atmosphere The solution of the coupled cascade equations for electrons and photons in the high-energy limit, i.e. using Eq. (5.18) and (5.20) as splitting probabilities, and for a power-law boundary condition (5.14b) at the top of the atmosphere is lengthy but straightforward. Here we mention only the two essential steps, for details see the classic paper of Rossi and Greisen [16]: First, one obtains an infrared-finite expression writing the divergent total bremsstrahlung probability as an integral and combining it with the gain term. Second, in the scaling limit the functions Z are for a fixed α simple numbers and one has to solve therefore only two coupled first-order differential equations. Hence, the solutions are of the type $A \exp(\lambda_1(X)) + B \exp(\lambda_2(X))$.

The number of electrons $N_e(X)$ in an electromagnetic shower initiated by a photon as function of the shower age

$$s = \frac{3t}{t + 2\beta} \quad (5.22)$$

is approximately

$$N_e = \frac{0.31}{\sqrt{\beta}} \exp \left[t \left(1 - \frac{3}{2} \ln s \right) \right], \quad (5.23)$$

where $t = X/X_0$ and $\beta = \ln(E/E_{\text{cr}})$. This approximation takes into account also low-energy processes; $N_e(X)$ is shown for several shower energies in Fig. 5.3. A shower initiated by a primary with energy $E = 10^{20}$ eV requires about one atmospheric depth to develop fully and contains around 10^{11} particles at its maximum.

5.5.2 Cascades on diffuse photon backgrounds

A high energy photon scattering on a low energy background photon (e.g. from the cosmic microwave or infra-red background) can start an electromagnetic cascade, via the two main processes

$$\gamma + \gamma_b \rightarrow e^+ + e^- \quad (5.24)$$

$$e + \gamma_b \rightarrow e^+ \gamma. \quad (5.25)$$

Pair production stops for $s = 4E_\gamma \varepsilon_\gamma < 4m_e^2$, where ε_γ is the typical energy of the background photons. Electrons continue to scatter on cosmic microwave photons in the Thompson regime, producing photons with average energy

$$E_\gamma = \frac{4}{3} \frac{\varepsilon_\gamma E_e^2}{m_e^2} \approx 100 \text{ MeV} \left(\frac{E_e}{1\text{TeV}} \right)^2. \quad (5.26)$$

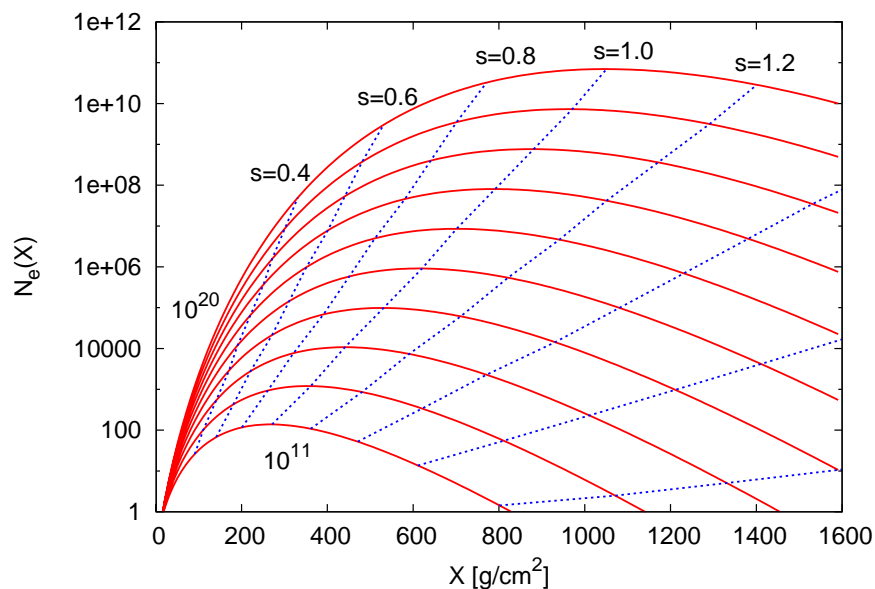


Figure 5.3: Number of electrons $N_e(X)$ in an electromagnetic shower initiated by a photon as function of the depth X for primary energies $10^{11}, 10^{12}, \dots, 10^{20}$ eV; the shower age s is also indicated.

Hence the Universe acts as a calorimeter for electromagnetic radiation, accumulating it in the MeV-GeV range. Moreover, it means that the Universe is opaque for high energy photons. Figure 5.4 show the absorption length of photons on various sources of background photons. Starting from energies in the TeV range, high-energy photon astronomy can study only the local (and therefore also recent) Universe. This is one of the main motivations to explore also high energy neutrinos, despite of the experimental challenges in neutrino detection.

5.6 Exercises

1. Show that P_{cl} for synchrotron radiation has the correct Lorentz transformation properties by expressing it as function of $F_{\mu\nu}$ and p_μ .
2. Rewrite the energy losses due to synchrotron radiation and Compton scattering as function of the energy density of the magnetic field and real photons and show that the two expressions agree in the classical limit.
3. Find the number of particles in the shower maximum, the corresponding shower age s and depth X_{max} from Eq. (5.23).

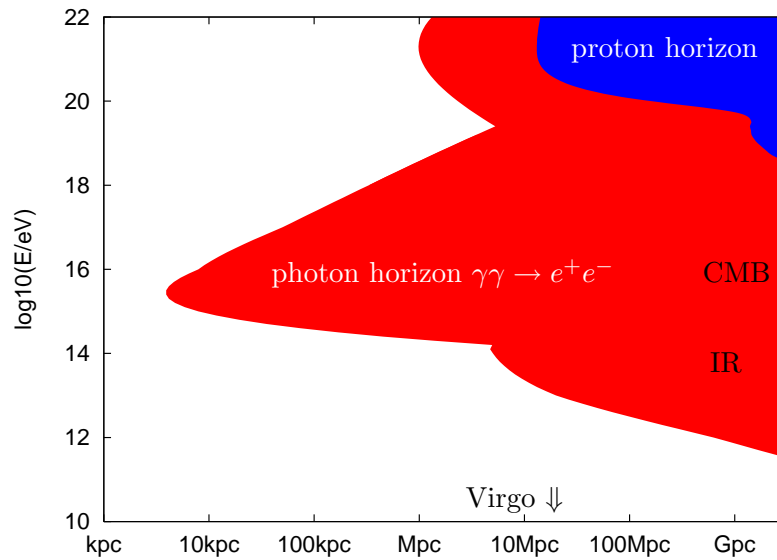


Figure 5.4: The gamma and the cosmic ray horizon, i.e. the free mean path of photons and cosmic rays as function of energy: The (red/blue) shaded area is inaccessible for photons/cosmic rays. The distance to the nearest galaxy cluster is also indicated.

6 Extragalactic cosmic rays

6.1 Propagation of extragalactic particles

6.1.1 Energy losses of protons and nuclei

There are three main energy loss processes for protons propagating over cosmological distances: Adiabatic energy losses due to the expansion of the universe, $-(dE/dt)/E = H_0$, e^+e^- pair-, and pion-production on photons of the cosmic microwave background (CMB).

The relative energy loss per time of a particle (due to interactions with the CMB) can be estimated as

$$\frac{1}{E} \frac{dE}{dt} = \langle y \sigma n_\gamma \rangle \quad (6.1)$$

where $y = (E - E')/E$ is the energy fraction lost per interaction, $n_\gamma \approx 410/\text{cm}^3$ is the density of CMB photons with temperature $T \approx 2.7\text{ K}$ and the brackets $\langle \dots \rangle$ remind us that we should perform an average of the differential cross section with the momentum distribution $n(\mathbf{p})$ of photons. In our estimates, we avoid this complication considering only reactions well above the threshold energy when essentially all photons participate in the reaction.

Electron-positron pair-production Since the produced e^+e^- pair in the process $p + \gamma \rightarrow p + e^+ + e^-$ is light, this energy loss process has a low threshold energy but leads in turn only to a small energy loss¹ per interaction, $y = 2m_e/m_p \approx 10^{-3}$. The threshold energy on CMB photons follows from $(k_p + k_\gamma)^2 \geq (m_p + 2m_e)^2$ as $E_p \geq m_e m_p / E_\gamma \sim 2 \times 10^{18}$ eV. The cross section of the reaction is $\sigma = \alpha/32\sigma_{\text{Th}}f(s)$, i.e. is a factor $\sim 2 \times 10^{-4}$ smaller than Compton scattering.

Pion-production and the GZK effect Greisen and Zatsepin and Kuzmin noticed that pion-production should introduce a “cutoff” in the cosmic ray spectrum. Since $y \approx m_\pi/m_p \approx 0.2$ close to threshold, but the cross-section is of similar size as the one of pair-production, the energy losses of protons suddenly increase around 5×10^{19} eV.

For an estimate of the cross section for pion production we use the Breit-Wigner formula with the lowest lying nucleon resonance Δ^+ as intermediate state,

$$\sigma_{\text{BW}}(E) = \frac{(2J+1)}{(2s_1+1)(2s_2+1)} \frac{\pi}{p_{\text{cms}}^2} \frac{b_{\text{in}}b_{\text{out}}\Gamma^2}{(E - M_R)^2 + \Gamma^2/4}, \quad (6.2)$$

where $p_{\text{cms}}^2 = (s - m_N^2)^2/(4s)$, $M_R = m_\Delta = 1.230\text{ GeV}$, $J = 3/2$, $\Gamma_{\text{tot}} = 0.118\text{ GeV}$, $b_{\text{in}} = 0.55\%$. At resonance, we obtain $\sigma_{\text{BW}} \sim 0.4\text{ mbarn}$ in good agreement with experimental data, cf. Fig. 6.1. We estimate the energy loss length well above threshold $E_{\text{th}} \sim 4 \times 10^{19}$ eV with

¹Close to the threshold, the energy fraction lost can be obtained considering the “decay” of the intermediate state at rest.

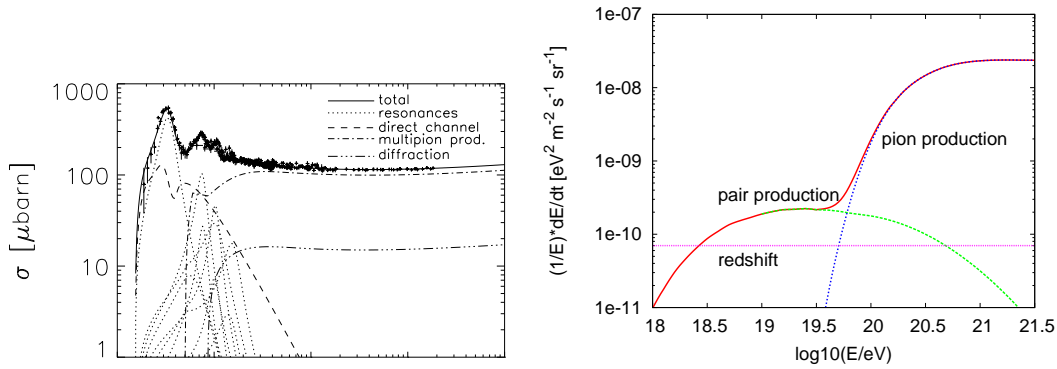


Figure 6.1: Left: Experimental data for the photo-nucleon cross-section together with a theoretical prediction for the contributions of various subprocesses, from Ref. [17]. Right: Comparison of the different contributions to the energy losses of a proton.

$\sigma \sim 0.1 \text{ mbarn}$ and $y = 0.5$ as

$$l_{\text{GZK}}^{-1} = \frac{1}{E} \frac{dE}{dt} \approx 0.5 \times 400 / \text{cm}^3 \times 10^{-28} \text{ cm}^2 \approx 2 \times 10^{-26} \text{ cm}^{-1} \quad (6.3)$$

or $l_{\text{GZK}} \sim 17 \text{ Mpc}$. Thus the energy loss length of a proton with $E \gtrsim 10^{20} \text{ eV}$ is comparable to the distance of the closest galaxy clusters and we should see only local sources at these energies. Note that it is this smallness of the “horizon scale” that makes the identification of UHECR sources feasible, despite the rather poor angular resolution of UHECR experiments, $\delta\vartheta \sim 1^\circ$, and deflections of charged particles in magnetic fields.

The right panel of Fig. 6.1 compares the relative energy losses of a proton due to redshift, e^+e^- pair- and pion-production on CMB photons. One clearly recognizes the increase of the energy losses by two orders of magnitude around $5 \times 10^{19} \text{ eV}$ and expects therefore a corresponding suppression (not a cutoff) of the cosmic ray flux above this energy. (Remember that each shell of thickness Δr contributes the same fraction to the total intensity, if energy losses and general relativistic effects can be neglected.) Thus the name GZK cutoff is somewhat misleading, and the exact strength of the suppression depends on various details as the number density of the sources.

The AGASA experiment detected in the 90’ies an excess of events above 10^{20} eV compared to predictions. There had been extensive discussions, if this result requires some kind of “new physics”, but meanwhile new data of the Hires and Pierre Auger Observatory (PAO) confirmed the UHECR flux expected in the presence of the GZK effect.

Attenuation of nuclei The dominant loss process for nuclei of energy $E \gtrsim 10^{19} \text{ eV}$ is photodisintegration $A + \gamma \rightarrow (A - 1) + N$ in the CMB and the infrared background due to the giant dipole resonance. The threshold for this reaction follows from the binding energy per nucleon, $\sim 10 \text{ MeV}$. Photodisintegration leads to a suppression of the flux of nuclei above an energy that varies between $3 \times 10^{19} \text{ eV}$ for He and $8 \times 10^{19} \text{ eV}$ for Fe.

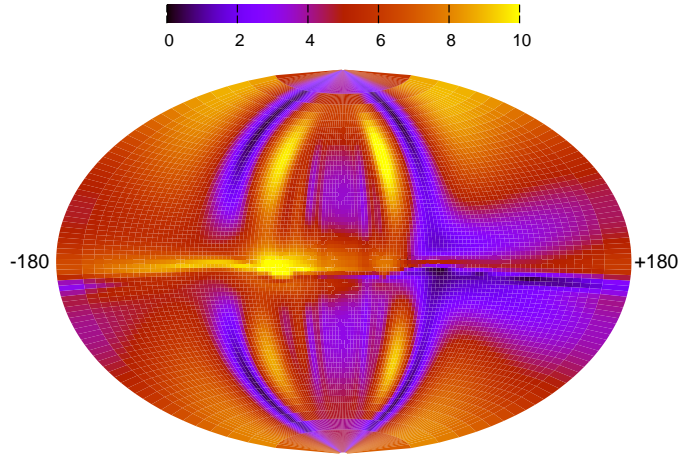


Figure 6.2: Deflection map of the GMF for a rigidity of 4×10^{19} V from Ref. [18]; The deflection scale at the top is in degree.

6.1.2 Galactic and extragalactic magnetic fields

Magnetic fields affect the propagation of charged particles deflecting them, leading in turn to synchrotron radiation. While even for ultrahigh energy protons synchrotron losses are negligible except in the relatively strong magnetic fields close to sources, the magnitude of deflections limits the possibility to perform charged particle astronomy. The deflection angle in a regular magnetic field after the distance d is

$$\vartheta \simeq \frac{d}{R_L} \simeq 0.52^\circ Z \left(\frac{p_\perp}{10^{20} \text{ eV}} \right)^{-1} \left(\frac{d}{1 \text{ kpc}} \right) \left(\frac{B}{\mu\text{G}} \right) \quad (6.4)$$

for a particle with momentum p_\perp perpendicular to B .

Figure 6.2 shows a deflection map for a specific model for the Galactic magnetic field and a rigidity of 4×10^{19} V; for details of the model see Ref. [18]. The map uses a Hammer-Aitoff projection of galactic coordinates with the Galactic center in the middle. The expected deflections depend strongly on the direction, but typically trajectories passing the Galactic center or plane suffer larger deflections.

Magnetic fields beyond the Galactic disk are poorly known and include possibly an extended regular and a turbulent field in the halo of our Galaxy and a large scale extragalactic magnetic field (EGMF). In the latter two cases, the magnetic field is simplest characterized by an r.m.s. strength B and a correlation length l_c , i.e. it is assumed that the field is smooth on scales below l_c in real space. If we neglect energy loss processes, then the r.m.s. deflection angle $\delta_{\text{rms}} = \langle \delta^2 \rangle^{1/2}$ over the distance $d \gg l_c$ is

$$\delta_{\text{rms}} \simeq \frac{(2dl_c/9)^{1/2}}{R_L} \simeq 0.8^\circ Z \left(\frac{E}{10^{20} \text{ eV}} \right)^{-1} \left(\frac{d}{10 \text{ Mpc}} \right)^{1/2} \left(\frac{l_c}{1 \text{ Mpc}} \right)^{1/2} \left(\frac{B}{10^{-9} \text{ G}} \right). \quad (6.5)$$

For a calculation of δ_{rms} one needs either observational data or reliable theoretical predictions both for the magnitude and the structure of EGMFs. At present, no single theory for the

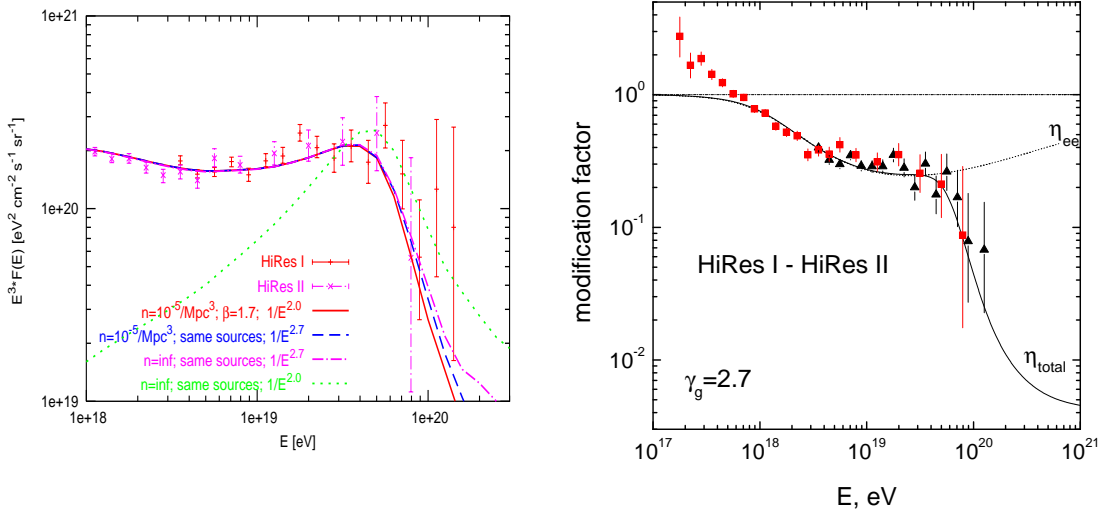


Figure 6.3: Left: Proton spectrum for different generation spectra [19]. Right: Modification factor for the proton spectrum from uniformly distributed sources [20].

generation of magnetic field has become widely accepted. Observational evidence for EGMFs has been found only in a few galaxy clusters observing their synchrotron radiation halos or performing Faraday rotation measurements. The two methods give somewhat different results for the field strength in clusters, with $B \sim 0.1\text{--}1 \mu\text{G}$ and $B \sim 1\text{--}10 \mu\text{G}$, respectively. Outside of clusters only upper limits exist for the EGMF. The combination of poor observational data and of a missing consistent theoretical picture prevents at present a reliable estimate of the influence of EGMFs on the propagation of UHECRs. It is likely that future UHECR data will provide the first information about EGMF outside the core of galaxy clusters.

Deflections also imply an average time delay of

$$\tau \simeq \delta_{\text{rms}}^2 d/4 \simeq 1.5 \times 10^3 Z^2 \left(\frac{E}{10^{20} \text{ eV}} \right)^{-2} \left(\frac{d}{10 \text{ Mpc}} \right)^2 \left(\frac{l_c}{1 \text{ Mpc}} \right) \left(\frac{B}{10^{-9} \text{ G}} \right)^2 \text{ yr} \quad (6.6)$$

relative to the rectilinear propagation of cosmic rays with the speed of light. As a result, even a bursting extragalactic source like a gamma ray burst is seen over time-scales that exceed vastly possible observation times.

6.2 The dip and the Galactic–extragalactic transition

Transition energy The traditional point of view of the transition between Galactic and extragalactic sources assumes that the generation spectrum of both Galactic and extragalactic cosmic rays is $dN/dE_g \propto 1/E^\alpha$ with $\alpha = 2.0\text{--}2.2$ as predicted by Fermi acceleration. In this picture, extragalactic sources dominate only above $E \sim 3 \times 10^{19} \text{ eV}$ the cosmic ray flux, cf. the green line in the left panel of Fig. 6.3. This scenario requires therefore the existence of new, isotropically distributed Galactic sources able to accelerate to $E \sim 10^{19} \text{ eV}$. In a more recent view, one uses as generation spectrum of extragalactic cosmic rays $dN/dE_g \propto 1/E^\alpha$ with $\alpha = 2.6\text{--}2.7$ and can then explain the shape of the cosmic ray spectrum down to a few $\times 10^{17} \text{ eV}$ with extragalactic sources [20]. How well the shape is described becomes clearer

plotting the “modification factor η ”, i.e. the ratio of the diffuse fluxes calculated taking into account all losses and including only redshift losses. In the right panel of Fig. 6.3, experimental data from the HiRes experiment are compared to the theoretically predicted modulation factor assuming a simple power-law as generation spectrum. Galactic sources dominate the spectrum, when $\eta > 1$: In this case, the observed cosmic ray intensity is larger than expected from extragalactic sources alone. Hence Fig. 6.3 motivates the view that Galactic sources dominate the spectrum only below a (few $\times 10^{17}$ – 10^{18}) eV.

There exist at least two different explanations for the steep generation spectrum with $\alpha = 2.6$ – 2.7 : Either it indicates that the acceleration to energies above $E \gtrsim 10^{17}$ eV is not mainly based on Fermi shock acceleration, or that the diffuse and the source spectra differ not only by propagation effects. In the latter case, it is sufficient that there is a distribution of maximal source energies as $dn/dE_{\max} \propto 1/E^{1.6}$. This assumption is plausible, since the number of sources able to accelerate to higher and higher maximal energies E_{\max} should decrease with E_{\max} .

Magnetic Horizon The transition between Galactic and extragalactic dominance in the cosmic ray spectrum may be caused by a magnetic horizon hiding extragalactic sources below $E \lesssim 10^{18}$ eV. The maximal distance a cosmic ray can travel is in the diffusion picture given by

$$r_{\text{hor}}^2 = \int_0^{t_0} dt D(E(t)) = \int_{E_0}^E \frac{dE'}{\beta} D(E'(t)), \quad (6.7)$$

where t_0 is the age of the Universe. If we consider cosmic rays with energy below $E_0 \lesssim 10^{18}$ eV, the energy losses are mainly due to the expansion of the Universe, $\beta = dE/dt = -H$. We use a “quasi-static” Universe, $H(t) = H_0$ and $t_0 H_0 = 1$. Then $E(t) = E_0 \exp(-H_0 t)$ and

$$r_{\text{hor}}^2 = \frac{cl_c}{6H_0} \left(\frac{E}{E_{\text{cr}}} \right)^2 (\exp(2) - 1), \quad (6.8)$$

using $D(E) = cl_c/3(E/E_{\text{cr}})^2$ valid for $R_L \gtrsim l_c$. (Remember that E_{cr} was defined by $R_L(E_{\text{cr}}) = l_c$.)

If we assume that a magnetic field with coherence length $l_c \sim \text{Mpc}$ and strength $B \sim 0.1$ nG exists in a significant fraction of the Universe, then the size of the magnetic horizon at $E = 10^{18}$ eV is $r_{\text{hor}} \sim 100$ Mpc. Hence, similar to the GZK suppression above 6×10^{19} eV, we see a smaller and smaller fraction of the Universe for lower and lower energies. As a consequence, the spectrum of extragalactic cosmic rays visible to us steepens below 10^{18} eV and the extragalactic component becomes sub-dominant.

Energetic reasons suggest that not only the observed diffuse spectrum but also the intrinsic spectrum of extragalactic UHECR steepens not far below 10^{17} eV: The total luminosity of a source depends on its minimal energy as $L \propto E_{\min}^{2-\alpha}$. The combination of large α and small E_{\min} cuts across the energy budget of even as powerful and numerous sources as AGNs. This problem is softened if there is a transition to an $1/E^2$ generation spectrum at low energies.

6.3 Extensive air showers initiated by hadrons

A proton or a nuclei interacting at the top of the atmosphere produces an air shower consisting of a core of high energy hadrons that transfer continuously part of their energy to new

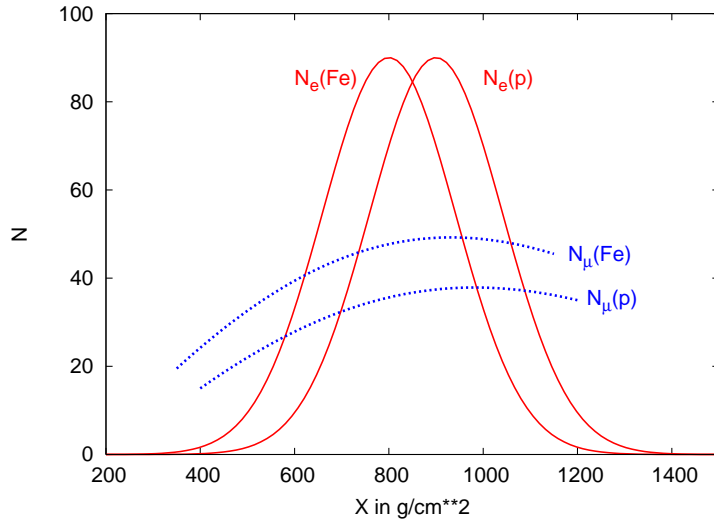


Figure 6.4: Electron number N_e and muon number N_μ (in arbitrary units) for two proton and iron showers as function of the depth X .

electromagnetic sub-cascades, mainly by the process $\pi^0 \rightarrow 2\gamma$. A smaller fraction of the energy is transferred by decays of charged pions to muons and neutrinos. We will not discuss these processes in detail, but refer instead only to the results of the simple model discussed in Sec. 5.5: The primary energy E_0 , the depth of the shower maximum X_{\max} and the number $N(X_{\max})$ of particles at the shower maximum are connected by

$$N(X_{\max}) \propto E_0 \quad \text{and} \quad X_{\max} \propto \ln E_0. \quad (6.9)$$

Differentiating between primaries According to the superposition model, a nuclei of mass number A and with energy E_0 interacts as A independent nucleons with energy E_0/A . Thus the number of particles at the shower maximum is unchanged but its position $X_{\max} \propto \ln E_0/A$ depends on A . As it is schematically shown in Fig. 6.4, an iron shower develops faster and reaches its maximum earlier than a proton shower. Moreover, the shower-to-shower fluctuations in the case of heavy nuclei as primaries are smaller compared to the ones for primary protons. This is very intuitive in the simple superposition picture where a shower initiated by a nuclei is described as a superposition of A independent showers. However, the simple superposition picture fails to describe quantitatively EAS fluctuations, because of the large fluctuations of elementary nucleus-nucleus interactions.

Figure 6.4 shows also the muon number N_μ for a proton and iron shower. First, because muons do not multiply through electromagnetic processes (for example, the cross section for the process $\gamma + A \rightarrow A + \mu^+ + \mu^-$ is strongly suppressed by the muon mass), their number is much smaller than the one of electrons and photons. As a result of the slower increase of N_μ and the large attenuation length, the muon number has a much weaker dependence on the depth. This reduces fluctuations and makes, at least in principle, the muon number a better estimator for the primary energy. However, this advantage is counterbalanced by the larger theoretical uncertainty of N_μ and the smaller number of muons. Figure 6.4 illustrates also

that observing both N_e and N_μ at a fixed depth X provides information about the chemical composition of cosmic rays.

Experimental techniques Present experiments use mainly two different techniques to detect ultrahigh energy cosmic rays. The traditional one uses an array of detectors on the ground to sample secondaries. Two commonly used detector types are scintillation detectors mainly sensitive to electrons and water tanks where the Cerenkov light emitted mainly by muons is recorded by photomultipliers. The array of detectors is built as sparse as possible, to achieve a large aperture within fixed time and money constraints. Therefore only a tiny fraction of all particles is measured. Timing information allows one to reconstruct the arrival direction and the core of the shower. Then a theoretical formula for the number density $\rho(r)$ of particles as function of the distance to the shower core and of the primary energy is fitted to the measurements. Empirically, it is found that $\rho(r)$ at rather large distance from the core is least sensitive to the primary type (i.e. the mass number A of nuclei) and has the smallest fluctuation from shower to shower. Depending on the detector type and the spacing of the array, this optimal distance varies and amounts e.g. to 1000 m in the case of the PAO. The conversion factor between, say $\rho(1000)$, and the primary energy has to be found either from Monte Carlo simulations or using different experimental techniques.

An example for a method that is calorimetric and therefore, at least in principle, allows one a model-independent determination of the primary energy is the fluorescence light method. As the shower passes through the air, electrons excite nitrogen molecules that emit isotropically fluorescence light. Optical cameras on the ground can trace therefore the shower evolution. If the excitation probability of nitrogen by a beam of electrons is known, the emitted light integrated over the shower trajectory can be used as a measure for the energy of the primary particle. Disadvantages of this method are the restriction to moonless nights, the need for a careful control of the atmospheric conditions, and the more difficult calculation of the aperture of the experiment.

6.4 Astronomy with charged particles

Possible anisotropies expected for extragalactic cosmic rays can be classified into four sub-classes:

- At such high energies that deflections in the Galactic and extragalactic magnetic fields are sufficiently small, point sources may reveal themselves as small-scale clusters of UHECR arrival directions. This requires additionally a rather low density of UHECR sources so that the probability to observe several events of at least a subset of especially bright sources is large enough. Even if one observes from most sources only one event, a correlation analysis with specific sources types may reveal the UHECR sources. This requires however to choose a very special class of astronomical sources and/or a high threshold energy, in order to keep the number of potential sources within the horizon sufficiently small.
- Moving to lower energies, the energy-loss horizon of UHECRs and thereby the number of sources visible increases. Moreover, deflections in magnetic fields become more important. As a result, the identification of single sources is not possible anymore. Instead, anisotropies on medium scales should reflect the inhomogeneous distribution of

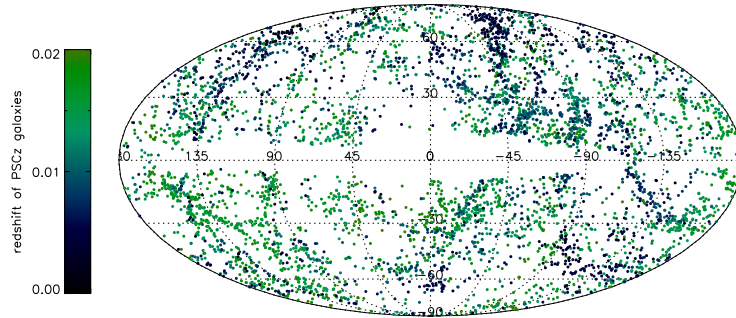


Figure 6.5: The distribution of normal galaxies color coded according their redshift, in galactic coordinates. The empty band along the Galactic plane is caused by extinction and does not reflect an intrinsic lack of objects [24].

UHECR sources that is induced by the observed large-scale structure (LSS) of matter, cf. Fig. 6.5. Since different source types have different clustering properties, this offers an alternative way to identify the sources of UHECRs.

- At even lower energies, also the LSS of sources disappears, both because the inhomogeneities in the source distribution will be averaged out due to the increased energy-loss horizon of UHECRs and because of deflections in the EGMF. Thus the cosmic ray sky would appear isotropic, if the Earth would be at rest with respect to the cosmological rest frame. As the observation of the CMB dipole shows, this is not case, and a dipole anisotropy is expected if the cosmic ray flux is dominated by sources at cosmological distance. This is the “cosmological variant” of the Compton-Getting effect discussed earlier.

Since the Sun moves with $u = 368 \pm 2$ km/s towards the great attractor, the predicted anisotropy is $\delta_{CG} = (2 + 2.7)u \simeq 0.6\%$ taking into account the observed spectrum $I(E) \propto E^{-2.7}$ of cosmic rays above the ankle. Deflections of UHECRs in the Galactic magnetic field should only displace the dipole axis, but not affect the magnitude of this effect. For instance, at energies $(2-3) \times 10^{19}$ eV and for proton primaries, the dipole position should be aligned to the one observed in the CMB within about 10° . Observing the Compton-Getting effect at only one energy provides combined information on the intervening Galactic magnetic field and the charge of the cosmic ray primaries. However, observations at two or more energies break this degeneracy. For example, the determination of the average primary charge is straightforward as long as cosmic rays propagate in the quasi-ballistic regime and given by the relative shift of the cosmic ray and CMB dipole axis at two different energies.

- Finally, analogous to the latitude effect in the geomagnetic field, the Galactic magnetic field (GMF) can induce anisotropies in the observed flux of extragalactic UHECRs, for rigidities low enough that blind regions exist. Anisotropies of this kind should be expected in models that invoke a dominating extragalactic proton component already at $E \simeq 4 \times 10^{17}$ eV or extragalactic iron nuclei at $E \lesssim 10^{19}$ eV [18].

It is not guaranteed that all these four anisotropies can be observed. If EGMFs are large, UHECR primaries are nuclei and/or the source density is large, the integrated flux above

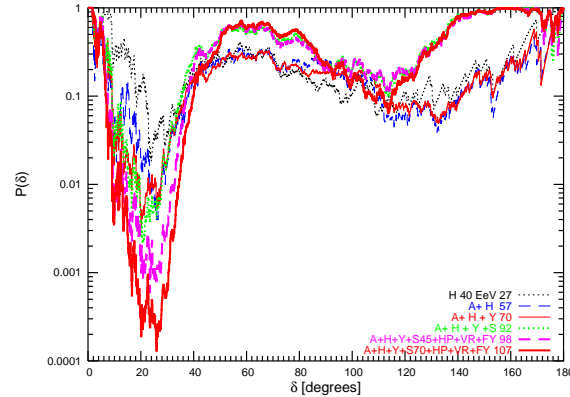


Figure 6.6: Chance probability $P(\delta)$ to observe a larger value of the autocorrelation function as function of the angular scale δ for different combinations of all publicly available experimental data; from Ref. [22].

the energy where point sources become visible may be for the present generation of UHECR experiments too small. Similarly, a transition from galactic to extragalactic sources at a relatively high energy reduces the chances to observe the cosmological Compton-Getting effect.

6.4.1 Clustering on medium and small scales

The cosmological Compton-Getting effect requires that inhomogeneities in the source distribution of cosmic rays are averaged out. As the free mean path of cosmic rays decreases for increasing energy, anisotropies connected to the large-scale structure (LSS) of cosmic ray sources become more prominent and replace the cosmological Compton-Getting effect. The exact value of this transition energy E_* depends both on the amount of clustering in the source distribution and the free mean path λ_{CR} of cosmic rays, i.e. also the primary type. For the specific case of proton primaries and a source distribution proportional to the density of baryons, Ref. [21] found $E_* \approx 5 \times 10^{19}$ eV and a minimal number of order 100 events for a detection.

The first strong evidence for medium-scale clustering was found combining all available data sets of UHECR events with energy $E \geq 5 \times 10^{19}$ eV and published arrival directions until 2005 in [22]. The most convenient tool to search for deviations from anisotropy is in this case the cumulative auto-correlation function,

$$W(\vartheta) = \frac{N(< \vartheta)}{N'(< \vartheta)} - 1, \quad (6.10)$$

where N and N' denote the number of pairs with separation angle $< \vartheta$ in the observed data and in a randomly generated data set, respectively. Figure 6.6 shows the chance probability P_{ch} to observe a larger number of pairs the random data than in the observed data. Clearly, the observed arrival directions show a surplus of clustering that is most significant on a typical scale of $\sim 25^\circ$. Similar findings have emerged recently from an analysis of the preliminary data from the Pierre Auger Observatory (PAO) [23]. For 64 events with $E > 4 \times 10^{19}$ eV the data presented in Ref. [23] show a surplus of clustering in the broad range from 7 to 30 degrees. Thus the LSS of matter, probably modified by extragalactic magnetic field, is

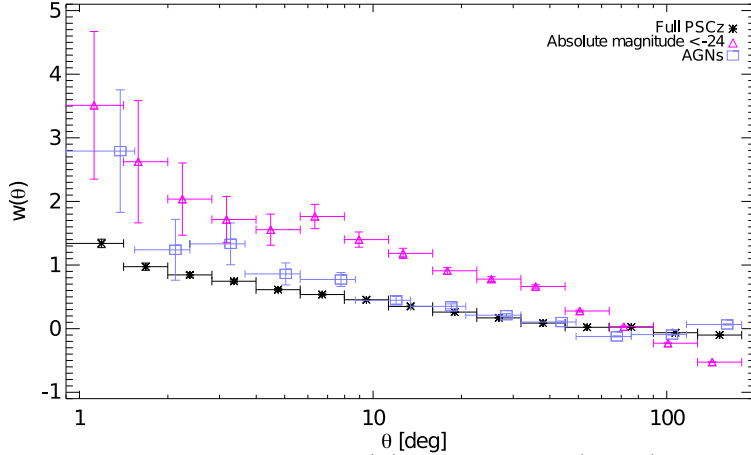


Figure 6.7: The auto-correlation function $w(\vartheta)$ for galaxies (black), galaxies with $M < 24$ (magenta), and AGNs (blue) as function of ϑ with 1σ error bars, from Ref. [24].

reflected in the arrival directions of UHECRs. The obvious question is how one can extract the information contained in a plot like Figure 6.6.

In order to address this issue, we compare the non-cumulative auto-correlation $w(\vartheta)$, i.e. considering the number of pairs N and N' per bin $[\vartheta - \Delta\vartheta : \vartheta + \Delta\vartheta]$, of galaxies and AGNs in Fig. 6.7. By construction, $w(\vartheta) > 0$ indicates overdense regions and one recognizes that the clustering at smaller angular scales increases for normal galaxies much slower than for AGNs. Tightening the cut in absolute magnitude to $M < 24$ makes the clustering of normal galaxies on the smallest scales comparable in strength to the one of AGNs. Both effects are easily understandable: More massive objects are stronger clustered, and the overlap of the brightest (optical) galaxies and AGN is large so that these two sets should have quite similar properties. A comparison of the auto-correlation function of UHECR arrival directions with the one from proposed source catalogues seems to be most promising on intermediate angular scales: First, the statistical errors both in cases of sources and cosmic rays become sufficiently small above $\sim 10^\circ$. Second, the effect of systematic errors like experimental errors and deflections in magnetic fields decreases on larger scales. Turning the second argument around, one can use the scale below which deviations between the measured and the expected autocorrelation functions appear as measure for the combined effect of deflections in extragalactic and Galactic magnetic fields.

A study of the auto-correlation function of UHECR arrival directions should allow one with a rather small event sample to distinguish between GRBs and AGNs as sources. Mainly long duration GRBs are discussed as sites for the UHECR acceleration. They occur in star forming galaxies that are less clustered as average galaxies. Thus GRBs should be distinguishable from AGNs by their clustering properties.

The strong clustering of AGNs as the paradigm source of UHECRs requires a re-interpretation of the traditional view of small-scale clustering. Often, one considered for simplicity uniformly distributed sources and distinguished between chance coincidences and true clusters, i.e. events from the same source. For clustered sources, the probability to observe multiplets from several sources in an overdense region is much increased and this might be the main source of small-scale clusters.

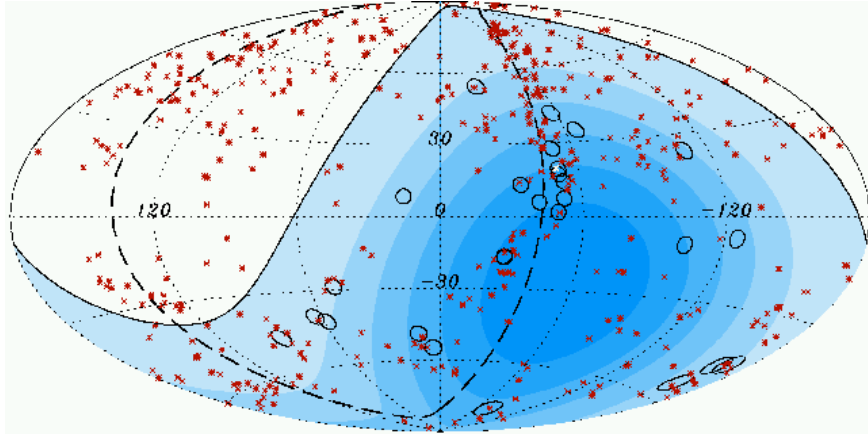


Figure 6.8: Skymap in galactic coordinates showing the arrival directions of the 27 highest energy cosmic rays with $E > 5.7 \times 10^{19}$ eV (black circles) detected by Auger and 472 AGN within 75 Mpc (red stars). The blue region indicates the field of view of Auger, from Ref. [25].

6.4.2 Correlations with astrophysical sources

The angular resolution of modern cosmic ray experiments reaches ~ 1 degree, and thus even for the UHECRs with the highest energies observed, $E \sim 10^{20}$ eV, deflections in magnetic fields are likely to be more important. In order to avoid a too large number of potential sources per angular search bin, one has thus to choose either a very specific test sample, e.g. a small subset of all AGNs, or a very high energy cut such that the cosmic ray horizon scale is sufficiently small, say of the order 100 Mpc. Thus we see that the GZK effect is a crucial ingredient for a successful correlation analysis.

Until now, all claims for correlations of UHECR arrival directions with specific source classes have remained controversial. It was anticipated that the increased aperture of the PAO should improve this situation. The recent analysis of the Auger experiment [25] claims indeed correlations between the arrival directions of the highest energy cosmic rays with $E > 5.7 \times 10^{19}$ eV and nearby AGNs. The red stars in Fig. 6.8 mark the positions of AGNs with distances ≤ 75 Mpc, while the open circles show the search bin with opening angle 3.1° around the CR arrival directions used in this analysis. An overdense region of AGNs along the supergalactic plane (dashed line) is clearly visible, where the angular distance between AGNs is considerably smaller than the size of the search bin used. The observation of a larger number of correlations between UHECR arrival directions and AGNs than expected from a random distribution, as in Ref. [25], should be therefore interpreted only as evidence that the UHECR sources have a similar distribution as AGNs. The differentiation among different sources (e.g. AGNs vs. GRBs or among different subtypes of AGNs) would require a comparison of the correlation (and/or auto-correlation) signal for different source types.

7 High energy neutrino astrophysics

7.1 Connecting neutrino, γ -ray and cosmic ray fluxes

Neutrinos are copiously produced by nuclear reactions in stars and SNe, and as secondaries in cosmic ray interactions. Because of the small distance to the production site, solar and atmospheric neutrinos are experimentally easiest accessible and the only ones regularly detected at present. The smallness of their interactions that makes neutrino detection experimentally so challenging turns neutrinos into ideal messengers to study the interiors of stars, the surroundings of supermassive black holes in AGNs or the edge of the universe.

As we noted in the introduction, any process involving hadronization, i.e. the formation of colorless hadrons out of quarks and gluons, leads mainly to the production of pions. Isospin symmetry fixes then the ratio of charged and neutral pions. For instance, close to the threshold, the two possible channels of photo-meson production, $p + \gamma \rightarrow p + \pi^0$ and $p + \gamma \rightarrow n + \pi^+$ have a ratio that is close to 2:1. While the π^0 decay produces two photons, the final state of the second channel contains after the decays $n \rightarrow p + e^- + \nu_e$ and $\pi^+ \rightarrow \mu^+ + \nu_\mu \rightarrow e^+ + \nu_e + \bar{\nu}_\mu + \nu_e$ two electrons and four neutrinos. Clearly, the production of neutrinos is thus intimately tied to the one of photons and electrons, and both depend in turn on the flux of primary cosmic rays.

While photons and electrons start electromagnetic cascades, either on photons in the source or from the CMB, neutrinos reach us suffering only from redshift losses. As a result, the measurement of X- and γ -rays fluxes can be used to limit possible high energy neutrino fluxes. The connection between the observed cosmic rays and neutrinos is more model-dependent. A popular set of assumptions is the following one: Protons are accelerated in a source region, confined by magnetic fields. They interact on background photons (say in the UV range) in the source, neutrons from $p + \gamma_{\text{UV}} \rightarrow n + \pi^+$ escape and provide the observed cosmic rays, while the π^+ decays produce neutrinos. This argument does not exclude that (a subset of) sources exists with sufficiently large interaction depth τ such that also neutrons interact frequently inside the source. The cosmic ray flux from these sources would be strongly suppressed and therefore this type of sources has been coined “hidden sources.” Before we discuss the connection of neutrinos, cosmic rays, and γ -ray fluxes, we consider the yield of neutrinos and photons for a single source.

Photon and neutrino yields at the source The yield $Y_i(E)$ of secondaries is defined as the dimensionless ratio of the secondary flux $\phi_i(E)$, $i = \gamma, \nu$, and the product of the initial proton flux $\phi_p(E)$ and the interaction depth τ ,

$$Y_i(E) = \frac{\phi_i(E)}{\tau \phi_p(E)}. \quad (7.1)$$

We consider only in detail the simpler case of photons as secondaries. Generalizing Eq. (5.10), the total photon flux from neutral pion decays that are in turn produced as secondaries in pp

or $p\gamma$ scatterings is

$$\phi_\gamma(E_\gamma) = 2 \int_{E_\gamma}^{\infty} \frac{dE_\pi}{E_\pi} \int_{E_\pi}^{\infty} dE_p N_{\pi^0}(E_p) \frac{d\sigma(E_p, E_\pi)}{dE_\pi} \tau(E_p) \phi_p(E_p), \quad (7.2)$$

where N_{π^0} denotes the multiplicity of neutral pions and τ the interaction depth. For the same assumptions as used in the derivation of Eq. (5.17), we obtain as approximation for the photon yields

$$Y_\gamma(E) = \frac{\phi_\gamma(E)}{\tau \phi_p(E)} = \frac{2}{\alpha} Z_{p\pi^0}(\alpha), \quad (7.3)$$

where now in the definition of $Z_{p\pi^0}(\alpha)$ the neutral pion multiplicity is included. The calculation of the neutrino yields proceeds along the same lines. However, the resulting expressions are rather lengthy, because the decays are non-isotropic, the decay chains are more complex and the final-state particles massive. The relevant expressions can be found in Refs. [E1,E2].

In Fig. 7.1, the neutrino yields $Y_\nu(E)$ from various subprocesses (pion, kaon and charm decays) are shown for a thermal distribution of photons with temperature $T = 10^4$ K and three different interaction depths. As long as $\tau \lesssim 1$, i.e. multiple scatterings can be neglected, the yields are by construction independent from τ . The yields are also independent from T , if one uses instead of the energy E the parameter $x = E\omega/m_p^2$, where $\omega = 1.6T$ is the maximum of the Planck distribution, Therefore they are a convenient tool to estimate photon or neutrino yields as long as $\tau \lesssim 1$. Tabulated values of Y for different α can be found in Ref. [E1,E2].

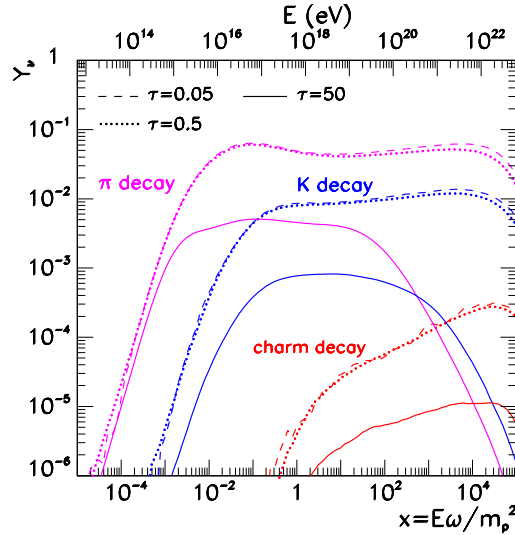


Figure 7.1: Neutrino yield Y as function of $x = E\omega/m_p^2$ for $T = 10^4$ K from pion, charged and neutral kaon, and charm decays for $\tau = 0.05, 0.5$ and 50 ; from Ref. [26].

Cascade limit The general concept of electromagnetic cascades discussed in Sec. 5.5 has several important applications. Firstly, we can use it to derive a simple bound on the UHE neutrino flux. Using the branching ratio 2:1 for $p + \gamma \rightarrow p + \pi^0$ and $p + \gamma \rightarrow n + \pi^+$, the approximation that the four leptons produced in muon decay share equally the energy as well

as the fact that in neutron decay almost all energy is taken by the proton, the ratio of energy transferred to neutrinos and the electromagnetic channel follows as 1:3, $\omega_\nu = 3\omega_\gamma$.

If we approximate the neutrino intensity in the range $[E, E_{\max}]$ by a power-law, $I_\nu(E) = AE^{-\alpha}$, then the integral neutrino intensity is connected to ω_ν via

$$I_\nu(> E) = \frac{\alpha}{\alpha + 1} \left[1 - \left(\frac{E_{\max}}{E} \right)^{-\alpha} \right]^{-1} \frac{c}{4\pi} \frac{\omega_\nu}{E}, \quad (7.4)$$

where ω_ν is the energy density in neutrinos in the same energy range $[E, E_{\max}]$. The first two terms are bounded by one, provided that the energy range considered is large enough, $\alpha \ln(E/E_{\max}) > 1$. With $\omega_\nu \leq 3\omega_\gamma$, we obtain thus as bound for the integrated neutrino flux

$$I_\nu(> E) \leq \frac{c}{12\pi} \frac{\omega_\gamma}{E}. \quad (7.5)$$

In order to apply this bound, we have to distinguish between different possible photon backgrounds on which cascades can develop. The only universal one is the CMB leading to a guaranteed flux¹ of UHE neutrinos via the GZK reaction of UHECRs as well as to a contribution to the diffuse photon flux in the 100 MeV–10 GeV range. This energy range has been observed by the EGRET experiment and thus a bound on the diffuse extragalactic gamma-ray flux can be derived. Integrating this maximal flux, the limit on ω_γ follows as

$$\omega_\gamma \leq 2 \times 10^{-6} \text{ eV/cm}^3. \quad (7.6)$$

If we assume that $I_\nu(E_\nu) = AE_\nu^{-2}$, we can combine Eqs. (7.5) and (7.6) into a limit on the differential neutrino intensity,

$$E_\nu^2 I_\nu(E_\nu) \leq 2 \times 10^{-6} \text{ GeV cm}^{-2} \text{ s}^{-1} \text{ sr}^{-1}. \quad (7.7)$$

Electromagnetic cascades may happen also inside many sources. Since the Thomson cross section is a factor 3000 larger than the cross section for photo-meson production, $\sigma_{\text{Th}}/\sigma_{p\gamma} \sim 3000$, sources where photo-meson reactions are relevant are likely optically thick. To be specific, let us assume that the source of opacity are UV photons, $\varepsilon_\gamma \sim 10 \text{ eV}$, as it is the case for many AGNs. Hence the critical energy for pair production is reduced to $E_{\text{cr}} \sim 25 \text{ GeV}$ compared to $E_{\text{cr}} \sim 400 \text{ TeV}$ for cascades on CMB photons. Thus the picture of the escaping photon radiation is as follows:

- Photons with $E \gg E_{\text{cr}}$ escape from the source only from an outer layer of such a thickness l that the interaction depth $\tau_{\gamma\gamma} = l\sigma_{\gamma\gamma}n_\gamma$ for pair-production is small, $\tau_{\gamma\gamma} \sim 1$.
- The source is bright in the $\sim 10 - 100 \text{ GeV}$ range, where the last generation of photons generated in the cascade can escape.
- Electrons with energy below E_{cr} continue to scatter in the source in the Thomson regime, producing photons in the X-ray range with average energy

$$E_\gamma = \frac{4}{3} \frac{\varepsilon_\gamma E_e^2}{m_e^2} \sim 100 \text{ eV} - 0.1 \text{ MeV} \quad (7.8)$$

for $E_e = 1 \text{ GeV}$ and 25 GeV , respectively.

¹If UHECRs are dominantly nuclei, a neutrino flux at lower energies from neutron decays (via $A + \gamma_{3K} \rightarrow (A - 1) + n$) results.

Cosmic ray limits The total energy density in neutrinos can be directly bounded by the energy density injected in cosmic rays by extragalactic sources, if neutrinos are produced only in transparent sources. If one assumes further that only neutrons can leave the sources, this bound becomes a prediction. To proceed, one has to specify the generation spectrum of extragalactic cosmic ray, i.e. one has to choose essentially between the traditional point of view (injection spectrum $dE/dN \propto E^{-2}$ and transition energy around 3×10^{19} eV) or the dip scenario [(effective) injection spectrum $dE/dN \propto E^{-2.6}$ and transition energy around 10^{18} eV]. Using the first choice, several authors advocated bounds or expectations for the neutrino flux of order

$$E_\nu^2 I_\nu(E_\nu) \sim \text{few} \times 10^{-8} \text{GeV cm}^{-2} \text{s}^{-1} \text{sr}^{-1}. \quad (7.9)$$

Thus the cosmic ray limit is about a factor 100 stronger than the cascade limit. However, one should be aware that even within the framework of transparent sources cosmic ray bounds obtained for a fixed set of parameters can only be indicative, because the sensitivity of the cosmic ray and the neutrino fluxes on several free parameters like the redshift evolution of their sources differs strongly.

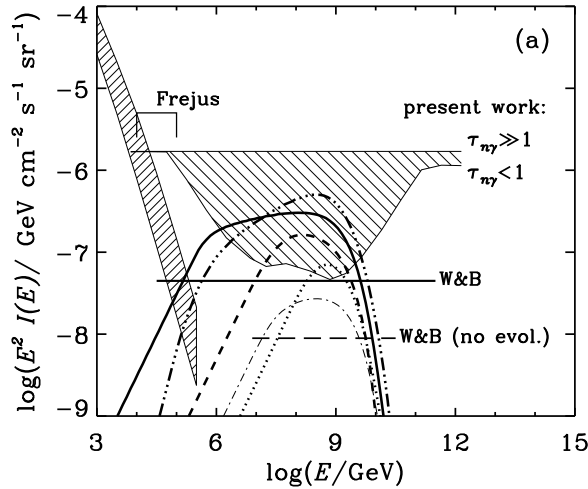


Figure 7.2: A collection of various bounds on neutrino fluxes: The solid line at the top corresponds to the cascade limit (7.7), the lower dashed horizontal line to the cosmic ray limit (7.9), while the lines in-between correspond to varying assumptions used for the cosmic ray limit, from Ref. [27].

7.2 Neutrino interactions, masses and mixing

One of the most surprising properties of the weak interactions is that only left-chiral fermions ($P_- \psi$) and right-chiral anti-fermions ($\bar{\psi} P_+$) participate in charged-current (CC) weak interactions,

$$\mathcal{L}_{CC} = -\frac{g}{\sqrt{2}} \sum_{\alpha} \bar{l}_{L,\alpha} \gamma^{\mu} \nu_{L,\alpha} W_{\mu}^{-} + \text{h.c.} . \quad (7.10)$$

Thus weak interaction violate parity P leading to a doublet/singlet structure of fermions,

$$\begin{pmatrix} \nu_e \\ e^- \end{pmatrix}_L, \begin{pmatrix} \nu_\mu \\ \mu^- \end{pmatrix}_L, \begin{pmatrix} \nu_\tau \\ \tau^- \end{pmatrix}_L \quad e_R, \mu_R, \tau_R. \quad (7.11)$$

The current (7.10) defines what we mean with electron neutrino: It is the neutrino created together with an electron in a CC interaction.

Since ordinary Dirac mass terms

$$m_f \bar{\psi}_f \psi_f = m_f (\bar{\psi}_f^L \psi_f^R + \bar{\psi}_f^R \psi_f^L) \quad (7.12)$$

are not gauge invariant, one introduces fermion masses in the standard model by gauge-invariant Yukawa interactions. These interactions need not to know about weak interactions and are thus not diagonal in flavor space,

$$\mathcal{L}_{\text{mass}} = - \sum_{\alpha, \beta} \bar{\nu}_{L, \alpha} M_{\alpha\beta}^{(\nu)} \nu_{R, \beta} - \sum_{\alpha, \beta} \bar{l}_{L, \alpha} M_{\alpha\beta}^{(\text{ch})} l_{R, \beta} + \text{h.c.}, \quad (7.13)$$

i.e. the mass matrices $M_{\alpha\beta}$ are not hermitian or even diagonal in the basis of the weak eigenstates. (We denote the weak eigenstates $\nu_\alpha = \{\nu_e, \nu_\mu, \nu_\tau\}$ and $l_\alpha = \{e, \mu, \tau\}$ by Greek indices $\alpha, \beta \dots$, and the mass eigenstates by Latin indices i, j, \dots . Furthermore, we have assumed that the neutrinos have only Dirac mass terms to simplify the formulas). Since the mass matrices are not hermitian, they cannot be diagonalized by a simple unitary transformation. However, arbitrary mass matrices can be diagonalized by a biunitary transformation,

$$M_{\text{diag}}^{(\nu)} = U^{(\nu)\dagger} M^{(\nu)} T^{(\nu)}, \quad (7.14)$$

where $U^{(\nu)} U^{(\nu)\dagger} = T^{(\nu)} T^{(\nu)\dagger} = \mathbf{1}$. Then, the connection between weak and mass eigenstates is given by

$$\nu_{R, \alpha} = \sum_i T_{\alpha i}^{(\nu)} \nu_{R, i}, \quad \nu_{L, \alpha} = \sum_i U_{\alpha i}^{(\nu)} \nu_{L, i}, \quad (7.15)$$

and similar equations hold for the charged leptons.

Inserting the transformations of Eq. (7.15) into the charged current Lagrangian (7.10) of the SM, results in

$$\mathcal{L}_{CC} = - \frac{g}{\sqrt{2}} \sum_{i, j} \bar{l}_{L, i} \gamma^\mu V_{ij} \nu_{L, j} W_\mu^- + \text{h.c.}, \quad (7.16)$$

where $V = U^{(\text{ch})\dagger} U^{(\nu)}$ is the analogue of the CKM matrix in the lepton sector. Since the charged current interaction involves only left-chiral fields of both charged leptons and neutrinos, the product of the two mixing matrices of the right-handed leptons, $T^{(\text{ch})\dagger} T^{(\nu)}$, is unobservable. The mixing $V = U^{(\text{ch})\dagger} U^{(\nu)}$ between charged leptons and neutrinos has two different sources: It could be ascribed either completely to mixing in the neutrino ($V = U^{(\nu)}$) or in the charged lepton sector ($V = U^{(\text{ch})\dagger}$), or most probably to some superposition of both. Only the combination V is observable and, by convention, we set $U^{(l)} = \mathbf{1}$.

In the case of massless neutrinos we can choose the neutrino mass eigenstates arbitrarily. In particular, we can set $U^{(\nu)} = U^{(\text{ch})}$ for any given $U^{(\text{ch})}$, hereby rotating away the mixing. This shows that neutrino masses are a necessary condition for non-trivial consequences of mixing in the lepton sector.

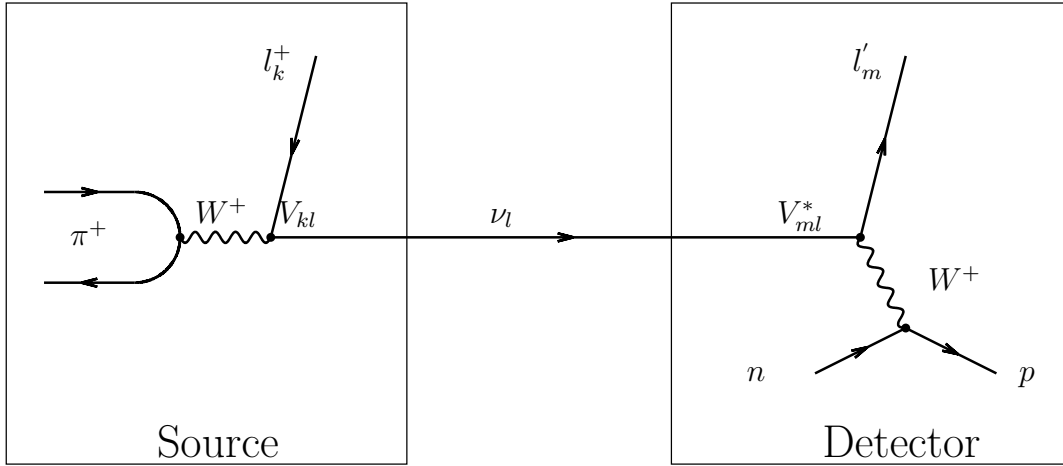


Figure 7.3: Production of a superposition of neutrino mass eigenstates ν_l in pion decay and subsequent detection of the neutrino flavour via the secondary lepton l'_m .

Neutrino oscillations in vacuum

Let us consider e.g. neutrinos produced in charged pion decay. The ratio R of $\pi \rightarrow e\nu_e$ and $\pi \rightarrow \mu\nu_\mu$ decay rates is

$$R = \frac{\Gamma(\pi \rightarrow e\nu_e)}{\Gamma(\pi \rightarrow \mu\nu_\mu)} = \frac{m_e^2}{m_\mu^2} \frac{(m_\pi^2 - m_e^2)^2}{(m_\pi^2 - m_\mu^2)^2} \approx 1.28 \times 10^{-4}, \quad (7.17)$$

since angular momentum conservation in the pion rest frame requires a helicity flip of the lepton. Similar, in neutron decay and in fusion reactions in stars only ν_e 's are emitted, because of energetic reasons. Hence, in many occasions we start with a (nearly) pure flavor state.

The time-evolution between creation of an arbitrary state at $t = 0$ and detection at t becomes simplest, if we decompose the weak interaction eigenstate ν_α into mass eigenstates ν_i ,

$$|\nu(t)\rangle = \sum_i U_{\alpha i}^{(\nu)} |\nu_i\rangle e^{-iEt}. \quad (7.18)$$

Neutrinos are in all applications ultra-relativistic,

$$E_i = (p^2 + m_i^2)^{1/2} \approx p + m_i^2/(2p), \quad (7.19)$$

where we have assigned also a definite momentum to the states $|\nu_i\rangle$.

$$|\nu(t)\rangle = e^{-ipt} \sum_i U_{\alpha i}^{(\nu)} |\nu_i\rangle e^{-im_i^2/(2p)t}. \quad (7.20)$$

The probability for a transition from the flavor ν_α to ν_β after the distance $L = ct$ is

$$P_{\alpha \rightarrow \beta}(t) = \left| \sum_{k=1}^n U_{\beta k}^* \exp(-iEt) U_{\alpha k} \right|^2, \quad (7.21)$$

where we introduced also $\Delta m_{ij}^2 = |m_i^2 - m_j^2|$.

To be specific, we consider the simple case of two-flavor neutrino oscillations. Then the survival probability is

$$P_{\nu_e \rightarrow \nu_e} = 1 - \sin^2 \left(\pi \frac{L}{l_{\text{osc}}} \right) \sin^2 2\vartheta \quad (7.22)$$

with the vacuum oscillation length

$$l_{\text{osc}} = 4\pi \frac{E}{\Delta m^2} \approx 2.5 \text{ m} \left(\frac{E}{\text{MeV}} \right) \left(\frac{\text{eV}^2}{\Delta m^2} \right) \quad (7.23)$$

Thus the survival probability depends only on L/E , the mass squared difference of the two neutrinos, and one mixing matrix element. Most strikingly, the smallness of the neutrino masses makes it possible to observe the interference of quantum states on macroscopic length scales.

7.3 Atmospheric neutrino oscillations

The principle production modes for neutrinos produced by cosmic rays in the atmosphere are pion, kaon and muon decays. With $\pi^\pm \rightarrow \mu^\pm + \nu_\mu(\bar{\nu}_\mu)$ and $\mu^\pm \rightarrow e^\pm + \nu_e(\bar{\nu}_e) + \bar{\nu}_\mu(\nu_\mu)$, one expects the ratio

$$\frac{\nu_e + \bar{\nu}_e}{\bar{\nu}_\mu + \nu_\mu} = \frac{N_e}{N_\mu} \sim \frac{1}{2}, \quad (7.24)$$

if all particles can decay. Muon decays become suppressed for $E \gtrsim 2.5 \text{ GeV}$ ($\lambda_d > \lambda_{\text{atm}}$) and thus the ratio should decrease for higher energies. Since most neutrinos are produced by low energy cosmic rays, geomagnetic effect must be included in the flux calculations. On the experimental side, the connection of the visible energy and direction (of the secondary electron or muon) to the one of the neutrino can be made only on a statistical basis and requires good knowledge of detector response and acceptance.

Part of these problems can be avoided by looking at the double ratio

$$R = \frac{(N_e/N_\mu)_{\text{data}}}{(N_e/N_\mu)_{\text{MC}}}. \quad (7.25)$$

If in the Monte Carlo no oscillations are included, one expect $R \sim 1$ if neutrinos are massless. The first conclusive deviation from $R = 1$ was found by the Superkamiokande experiment in 1998 with $R = 0.69 \pm 0.06$.

Ratio of up- and down-going muons A decisive test for the oscillation hypothesis is the ratio of up- and down-going muons: The oscillation length varies between 20km and 12800km, and as function of the zenith angle the ratio should show the form predicted by the neutrino oscillation formula. By fitting the experimental data to the free parameters Δm^2 and $\sin^2 \vartheta$ of the neutrino oscillation formula, one derived $\Delta m^2 \sim 2.2 \times 10^{-3} \text{ eV}^2$ and $\sin^2 \vartheta \sim 1$.

The atmospheric anomaly was later confirmed by sending a ν_μ beam from KEK to Kamioka. The distance KEK-Kamioka is $L = 250 \text{ km}$, while the mean neutrino energy was $E \sim 1.3 \text{ GeV}$. The combined result of the two experiments is shown in Fig. 7.4, yielding the surprising result that the atmospheric neutrino mixing angle is – in contrast to the quark sector – close to maximal.

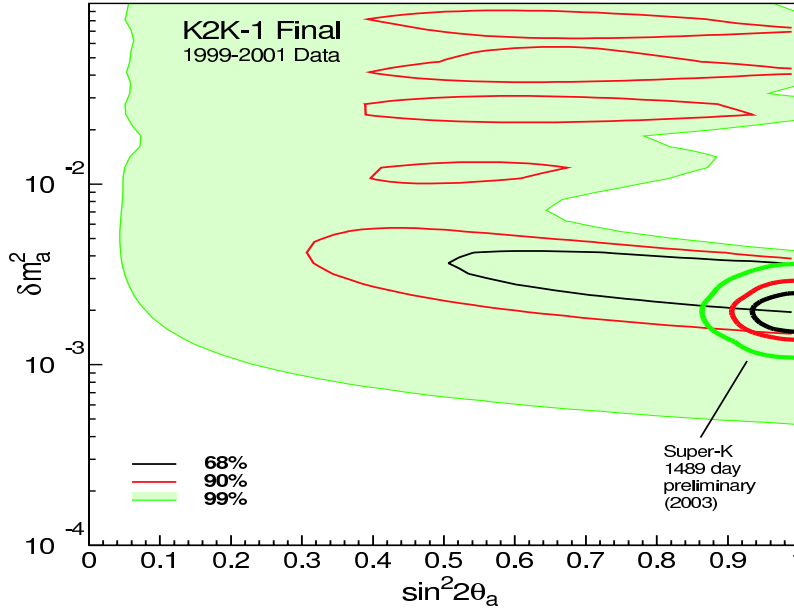


Figure 7.4: Overlay of the Superkamiokande and the K2K result.

7.4 High energy neutrino scattering

Parton model and scaling violation Neutrino-nucleon scattering can be described in the parton model. This model assumes that a nucleon probed at sufficiently high $Q^2 \gtrsim Q_{\min}^2 \sim 1 \text{ GeV}^2$ behaves as a collection of independently interacting partons, i.e. quarks and gluons. If the function $f_i(x)$ denotes the probability to find a parton of type i with momentum fraction $p_i = xp_N$ and $\sigma(\hat{s})$ the corresponding parton cross section, then the neutrino-nucleon cross section follows as

$$\sigma(s) = \sum_i \int_{x_{\min}}^1 dx f_i(x) \hat{\sigma}(\hat{s}). \quad (7.26)$$

In its original formulation, the parton model assumed that the parton distribution functions $f_i(x)$ depend only on x . We can convince ourselves that $f_i(x)$ should depend also on Q^2 by looking at a Bremsstrahlung process. Consider a quark as an external line of a Feynman diagram with momentum p and arbitrary mass m emitting a gluon of momentum q ,

$$\frac{1}{(p+q)^2 - m^2} = \frac{\pm 1}{2pq} = \frac{\pm 1}{2\omega E(1 - \cos \vartheta)}, \quad (7.27)$$

where ω is the energy of the gluon, E and v the velocity of the parton and ϑ the emission angle. There is a soft divergence for all m , if the energy of the emitted gluon goes to zero, $\omega \rightarrow 0$. Additionally, there is a collinear singularity for light partons, $v \rightarrow 1$, when $\vartheta \rightarrow 0$.

These singularities generate logarithmic divergences integrating over the final phase space,

$$d\sigma_{n+1} = \frac{\alpha_s(Q^2)}{2\pi} \ln^2(Q^2/Q_{\min}^2) d\sigma_n, \quad (7.28)$$

that can compensate the strong coupling although α_s is small for large Q^2 . As a result, parton cascades or jets develop in fragmentation processes. Similarly, the parton number inside a

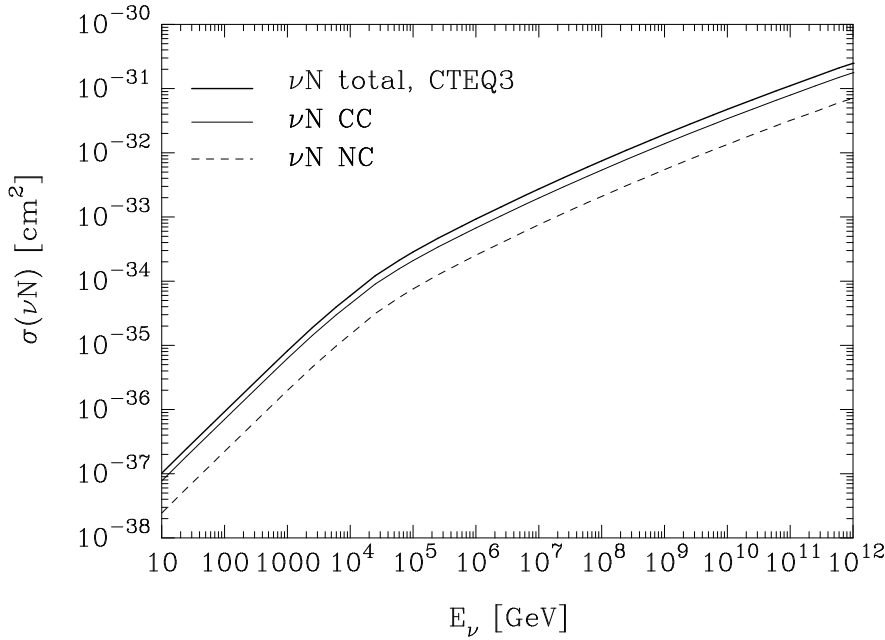


Figure 7.5: Cross sections for νN interactions at high energies: dotted line, $\sigma(\nu N \rightarrow \nu + \text{anything})$; thin line, $\sigma(\nu N \rightarrow \mu^- + \text{anything})$; thick line, total (charged-current plus neutral-current) cross section, from Ref. [28].

nucleon increases with increasing Q^2 . Although the neutrino-quark cross section is constant above $s \gg m_W^2$, the neutrino-nucleon cross section continues to grow as $\sigma \propto E^{0.4}$, because the number of accessible partons with $x \geq x_{\min} \sim Q_{\min}^2/s$ increases as $xq(x, Q^2) \sim x^{-0.33}$.

DGLAP equations The Q^2 -dependence of the parton distribution functions is described in perturbative QCD by the Dokshitzer-Gribov-Lipatov-Altarelli-Parisi (DGLAP) equations

$$\frac{dq_i(x, Q^2)}{dt} = \frac{\alpha_s(Q^2)}{2\pi} \int_x^1 \frac{dy}{y} \left[q_i(y, Q^2) P_{qq} \left(\frac{x}{y} \right) + g(y, Q^2) P_{qg} \left(\frac{x}{y} \right) \right] \quad (7.29)$$

$$\frac{dg_i(x, Q^2)}{dt} = \frac{\alpha_s(Q^2)}{2\pi} \int_x^1 \frac{dy}{y} \left[q_s(y, Q^2) P_{gq} \left(\frac{x}{y} \right) + g(y, Q^2) P_{gg} \left(\frac{x}{y} \right) \right]. \quad (7.30)$$

with $t = \ln(Q^2/Q_0^2)$ and $q_s = \sum_{j=1}^{n_f} [q_j + \bar{q}_j]$. The splitting functions $P_{ij}(\frac{x}{y})$, with $i, j = q, g$ give the probability that parton j with momentum y radiates a quark or gluon and becomes a parton of type i with fraction $(\frac{x}{y})$ of the momentum of parton j .

If we compare this equation to the production term of the transport equation for cosmic rays, Eq. (3.38), we see that the structure of the two equations is the same. The reason for this formal agreement (or the simplicity of the DGLAP equations) is that interference terms can be neglected in the QCD cascade, since it corresponds to a semi-classical evolution.

7.5 Astrophysical sources of high energy neutrinos

Experiments and techniques Main problem of high energy neutrinos physics is the atmospheric neutrino background and the expected low fluxes from astrophysical neutrino sources.

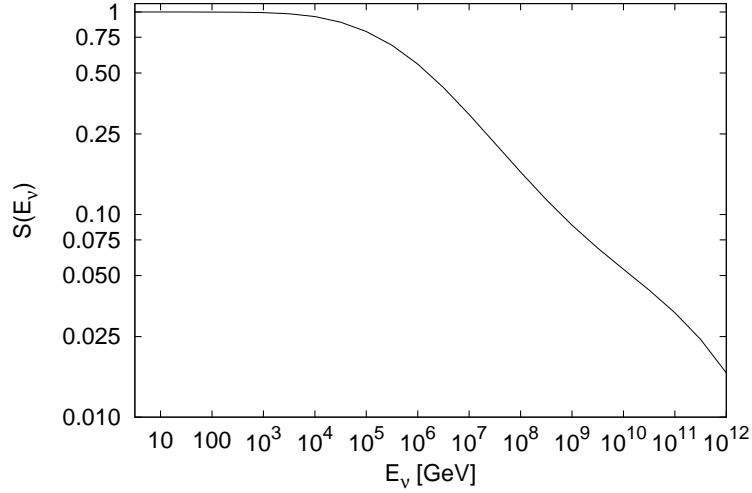


Figure 7.6: Averaged shadow factor $S(E)$ as function of the neutrino energy.

The search for neutrino sources is most promising at high energies, because the atmospheric neutrino flux is very steep: At high energies, pions scatter and muons do not decay. Main detection methods are at present Cherenkov light (in ice or water) emitted e.g. by a relativistic muon produced in the reaction $\nu_\mu + N \rightarrow \mu + X$. In the future, the radio or acoustic signal produced by a horizontal shower initiated by a neutrino reaction may allow one the supervision of even larger detector volumes.

The event rate of muons with energy $E > E_{\min}$ in a detector of area A is

$$\text{Rate} = A \int dE d\Omega P_\mu(E; E_\mu^{\min}) S(E) I_\nu(E_\nu). \quad (7.31)$$

Here, the shadow factor S takes the attenuation in the Earth into account, and $P_\mu(E; E_\mu^{\min})$ is the probability that a muon is created and reaches the detector with $> E_{\min}$.

Attenuation and Shadow factor The growth of the neutrino-nucleon cross section with energy means that above $E_\nu \sim 40$ TeV the Earth becomes opaque even for neutrinos. If we neglect any regeneration effects and assume that the flux is isotropic, this attenuation can be represented by a shadow factor. The shadow factor averaged over the upward-going hemisphere is

$$S(E) = \frac{1}{2\pi} \int_{-1}^0 d \cos \vartheta \int d\phi \exp[-X(\vartheta)/\lambda_{\text{int}}(E)] \quad (7.32)$$

and is shown in Fig. 7.6.

Average range of muons The second ingredient in the rate calculation is the probability that the neutrino creates a muon that is energetic enough to arrive at the detector with an energy E_μ larger than the detector's threshold energy E_μ^{\min} . The probability that a muon can

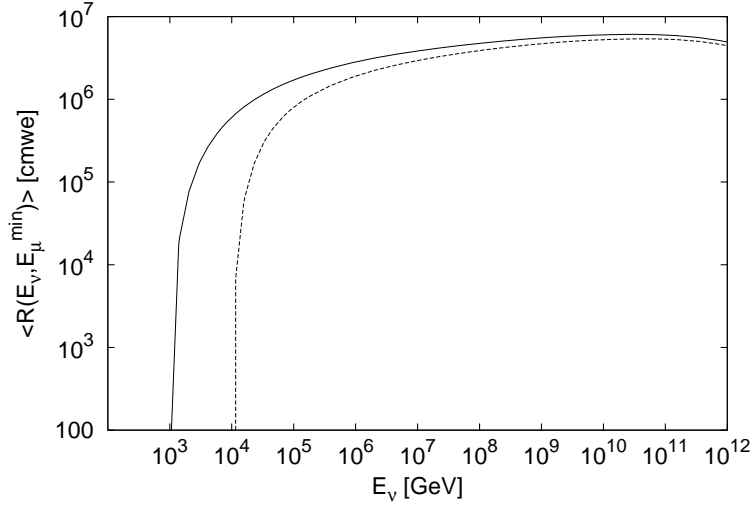


Figure 7.7: Average ranges (in rock) for muons produced in charged-current interactions of neutrinos with energy E_ν , at threshold energies $E_\mu^{\min} = 1$ and 10 TeV.

be recorded in a detector depends on the average range $\langle R \rangle$ of a muon in rock

$$\langle R(E_\nu; E_\mu^{\min}) \rangle = \frac{1}{\sigma_{CC}(E_\nu)} \int_0^{1-E_\mu^{\min}/E_\nu} dy R(E_\mu, E_\mu^{\min}) \frac{d\sigma_{CC}(E_\nu, y)}{dy}, \quad (7.33)$$

where the energy of muons produced in a charged-current interaction of neutrinos with matter is $E_\mu = (1 - y)E_\nu$. After a high energy muon is produced, it undergoes a continuous energy loss as it propagates. The range R of an energetic muon follows from the energy-loss relation

$$-dE_\mu/dX = \alpha(E_\mu) + \beta(E_\mu)E_\mu, \quad (7.34)$$

where X is the thickness of matter traversed by the muon in g/cm^2 . The first term represents ionization losses, while the second term represents bremsstrahlung, e^+e^- pair production and nuclear interactions. If the coefficients α and β are independent of energy, we can approximate their values to be $\alpha = 2.0 \times 10^{-3} \text{ GeV cmwe}^{-1}$ ($\text{cmwe} = \text{g}/\text{cm}^3$) and $\beta = 3.9 \times 10^{-6} \text{ cmwe}^{-1}$. Integrating Eq. (7.34), the muon range is

$$R(E_\mu, E_\mu^{\min}) \equiv X(E_\mu^{\min}) - X(E_\mu) = \frac{1}{b} \ln \frac{a + bE_\mu}{a + bE_\mu^{\min}}. \quad (7.35)$$

The average range of muons from charged current neutrino interactions is shown in Fig. 7.7 for threshold energies 1 TeV and 10 TeV. A muon produced with $E_\mu = 10$ TeV will travel on average a few kilometers until its energy is degraded to 1 TeV.

The probability that a muon neutrino of energy E produces an observable muon is then

$$P_\mu(E, E_\mu^{\min}) = N_A \sigma(E) \langle R(E; E_\mu^{\min}) \rangle \quad (7.36)$$

and is shown in Fig. 7.8. A useful approximation for energies $E \gtrsim \text{TeV}$ is $P_\mu(E, E_\mu^{\min}) \sim 2 \times 10^{-6} (E_\nu/\text{TeV})^{0.8}$.

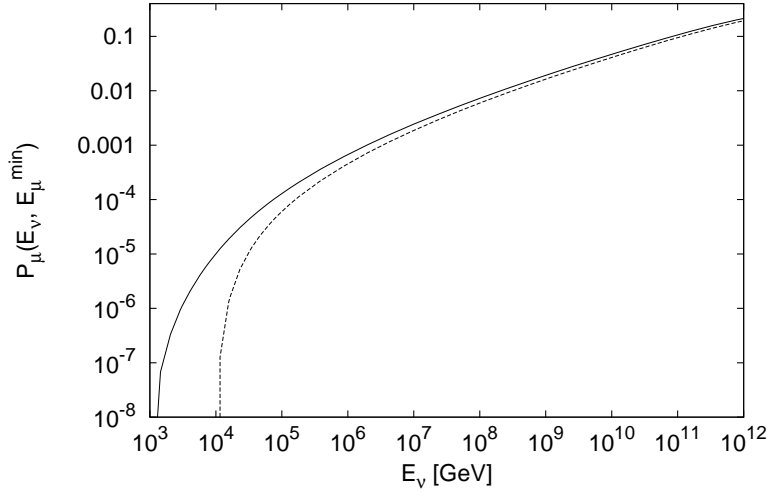


Figure 7.8: Probability that a neutrino of energy E_ν produces an observable muon with energy exceeding $E_\mu^{\min} = 1$ TeV and 10 TeV.

Sensitivity and event rates We derive now a rough estimate of the event rate expected in a neutrino telescope. We assume $E_{\min} = 10^6$ GeV as minimal energy in order to avoid the background of atmospheric neutrinos and a neutrino intensity equal to the cascade limit (7.7). Then we approximate the remaining ingredients of the integrand in Eq. (7.31) as $P_\mu \sim 10^{-3}(E/E_{\min})^{0.8}$ and $S \sim (E/E_{\min})^{-0.2}$. Choosing as area $A = (0.1 \text{ km})^2$, i.e. the area covered by the current ICECUBE prototype AMANDA, we obtain of order 1 event/year. Thus the sensitivity of this experiment corresponds roughly to the maximal flux allowed by the cascade limit, while an 1 km^3 neutrino telescope like ICECUBE will probe fluxes down to the ones compatible with the cosmic ray limit.

7.6 Exercises

1. Derive from Fig. 6.3 the energy density of (extragalactic) cosmic rays above 10^{18} eV for $\alpha = 2$ and 2.7. Estimate from Fig. 6.1 the “life-time” of a cosmic ray and thus the required emissivity \mathcal{L} .
2. Derive for two neutrino the oscillation probability, $P_{\nu_e \rightarrow \nu_\mu}$, starting from the mixing matrix

$$U = \begin{pmatrix} \cos \vartheta & \sin \vartheta e^{i\phi} \\ -\sin \vartheta & \cos \vartheta e^{i\phi} \end{pmatrix}. \quad (7.37)$$

Show that that the Majorana phase ϕ does not enter the oscillation probability. Convince yourself that probability is conserved.

8 Cosmic rays as tool for particle physics

8.1 Air shower and new particle physics

At present accelerator data from the Tevatron constrain new physics directly only up to 1 TeV, while in the near future LHC extends this range up to 14 TeV. Therefore one might wonder if cosmic ray data can be used to constrain new particle physics at energy scales that are not accessible to human accelerators. However we know from the discussion in Sec. 2.2 that a significant change of hadronic cross sections requires the modification of scattering with small four-momentum transfer t – while new physics is most often connected to the regime of large masses and therefore large t . More promising is neutrino scattering where at high energies the whole range $0 \leq |t| \lesssim m_W^2$ contributes uniformly to the neutrino-nucleon cross section on the parton level.

New resonances In secs. 2.2 and 7.5 we considered mainly the t -channel contribution to cross sections. To complement this discussion, we assume now that a new particle with mass m and decay width Γ acts as a s -channel resonance in νN scattering. (Concrete examples are models containing lepto-quarks or a sneutrino in R -parity violating supersymmetry.) In the narrow-width approximation, $\Gamma \ll m$, for the Breit-Wigner denominator

$$\frac{1}{(\hat{s} - m^2)^2 + m^2\Gamma^2} \rightarrow \frac{\pi}{m\Gamma} \delta(\hat{s} - m^2) \quad (8.1)$$

in the partonic cross section, the integration over x just picks out partons with $\hat{s} = xs = m^2$. The total cross section is

$$\sigma_{\nu N}(s) \sim \sum_i \frac{g^2}{m^2} xq_i(x = m^2/s, Q^2 = s), \quad (8.2)$$

and hence is suppressed for large m . Experimental limits require either a small coupling g , a large mass m , $m^2 \gtrsim M_W^2$ or a suitable combination. This simple example illustrates that it is difficult to increase the interactions of neutrinos by a large factor. An exception may be models with large extra dimensions. An important ingredient for the large increase of the νN cross section in these models is that the neutrino couples not only to quarks but also to gluons.

Neutrinos as the particles with the smallest cross section are the most sensitive tool to search with cosmic ray data for deviations from the standard model predictions caused by unknown physics. They produce mostly showers close above or below the horizon. Looking at the zenith angle dependence of the event rate, one can disentangle the cross section and flux, and thus test for deviations from the standard model prediction.

Understanding strong interactions We have seen that several aspects of strong interaction cannot be calculated within QCD but are described by phenomenological models. Moreover,

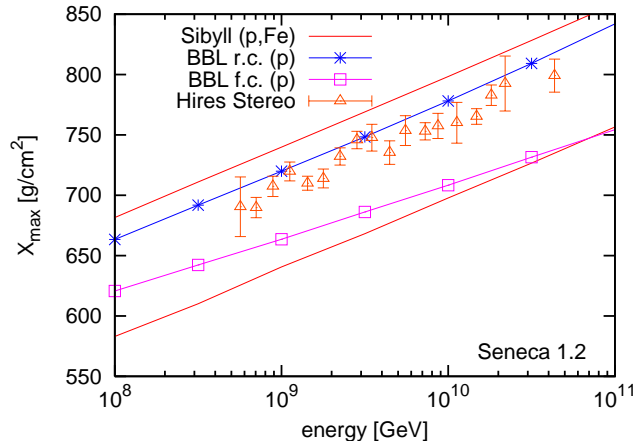


Figure 8.1: Experimental data (red, with errorbars) and model predictions for X_{\max} distribution as function of energy, from Ref. [29].

even usual methods and results from perturbative QCD may become unreliable at ultrahigh energies. A simple example are the DGLAP equation and the parton distribution functions: In the standard picture, only splittings $X \rightarrow YZ$ are taken into account, and for decreasing x the number of partons in nucleons increases monotonically. As a result, the neutrino nucleon cross section increase like a power, while for $s \rightarrow \infty$ only a logarithmic growth is allowed. Physically, the density of partons cannot become infinite and at some point recombinations, $YZ \rightarrow X$, will balance splittings.

Although the physical picture seems to be rather simple, its formalization is highly non-trivial and has led e.g. to ideas like the “color glass condensate.” A test of one of these proposals against experimental cosmic ray data is shown in Fig. 8.1. The two red curves are the prediction of an often used model for hadronic interaction in cosmic ray physics for protons (upper) and iron (lower line). These two curves enclose the experimental data (red, with errorbars) and thus this model predicts that the cosmic ray flux is a mixture of protons and heavier nuclei. The other two lines are models where the growth of the parton density is slower than in perturbative QCD. Both lines are for protons and the corresponding lines for iron would be even lower. Hence the model producing the magenta line is already excluded by cosmic ray data, while the other one predicts a pure proton flux.

In summary, cosmic ray data can be used at present only to exclude extreme model predictions, since the chemical composition of cosmic rays is not independently fixed. The discovery of cosmic ray sources and the subsequent study of cosmic ray deflections in magnetic fields offers an alternative way to measure the chemical composition, providing in turn the possibility to test QCD models more precisely at ultrahigh energies.

8.2 Relics from the early universe as cosmic rays sources

Evidence for dark matter comes from flat rotation curves of galaxies, the virial mass of galaxy clusters, big-bang nucleosynthesis, structure formation and the CMB: Combining all these pieces of evidence, one concludes that there exists around six times as much cold dark matter (CDM) than baryons. Many well-motivated dark matter candidates that can have the

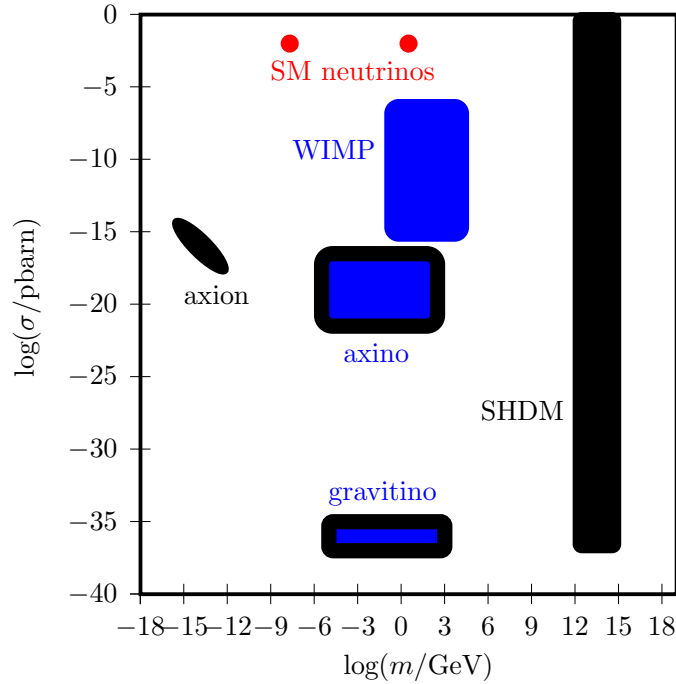


Figure 8.2: A selection of dark matter candidates in the plane cross section versus mass; blue and black corresponds to thermal and non-thermal as main production channel.

correct abundance have been proposed, with a rather big variety in their properties as shown in Fig. 8.2. Therefore most of them have to be searched for by some specialized methods. We shall discuss only two candidates in more detail that can serve also a source of cosmic rays. One of them are “WIMPs,” i.e. particles with masses and interactions similar to the weak scale. The second one are superheavy DM particles (SHDM) with masses around 10^{13} GeV. Before, we comment briefly on the other candidates shown in Fig. 8.2: Neutrinos with interactions as predicted by the standard model would have either with $\sum_{i=1}^3 m_i \approx 10$ eV or few GeV the correct abundances as thermal relics. Both possibilities are excluded by various reasons. Axions were proposed as solution to the strong CP problem. They are pseudo Goldstone bosons that mix with pions, and therefore their masses and decay constants are connected by $m_a = m_\pi f_\pi / f_a$. Gravitinos and axinos are supersymmetric partners of the axion and the graviton, respectively. They can be the lightest supersymmetric particle that is protected in many models by a symmetry and thus stable. Last but not least, the lightest neutralino, a mixture of the supersymmetric partners of higgses, Z and photon, is a typical example for a WIMP.

8.2.1 WIMPs as thermal relics

When the number $N = nV$ of a particle species is not changed by interactions, then the expansion of the Universe dilutes their number density as $n \propto R^{-3}$. The corresponding change in time is connected with the expansion rate of the universe, the Hubble parameter

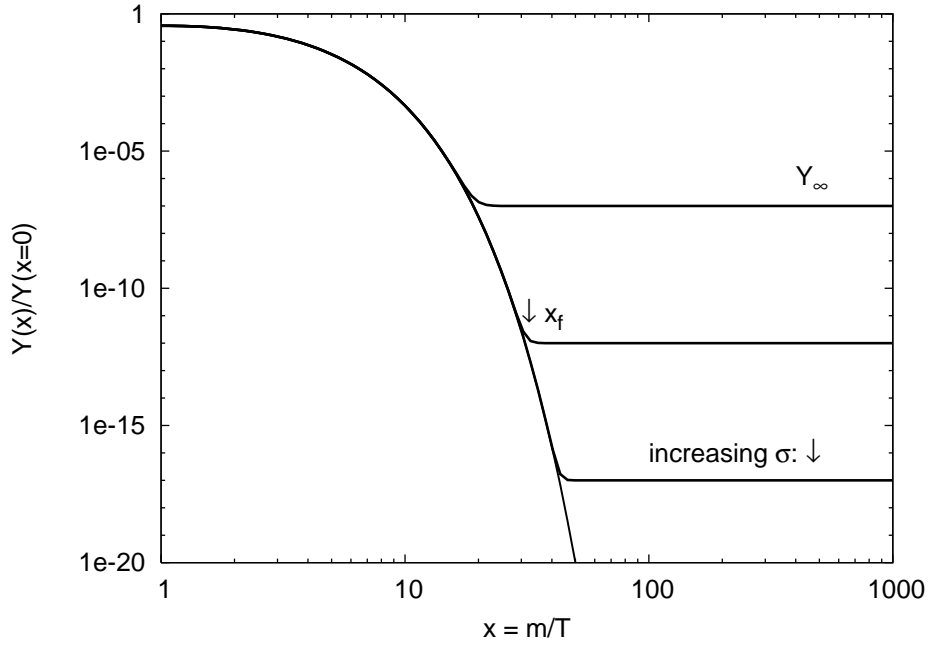


Figure 8.3: Illustration of the freeze-out process. The quantity $Y = n_X/s$ is n_X divided by the entropy density $s \propto R^{-3}$ to scale out the trivial effect of expansion.

$H = \dot{R}/R$, as

$$\frac{dn}{dt} = \frac{dn}{dR} \frac{dR}{dt} = -3n \frac{\dot{R}}{R} = -3Hn. \quad (8.3)$$

Additionally, there might be production and annihilation processes. While the annihilation rate $\beta n^2 = \langle \sigma_{\text{ann}} v \rangle n^2$ has to be proportional to n^2 , we allow for an arbitrary function as production rate ψ ,

$$\frac{dn}{dt} = -3Hn - \beta n^2 + \psi. \quad (8.4)$$

In a static Universe, $dn/dt = 0$ defines equilibrium distributions n_{eq} . Moreover, detailed balance requires $\beta n_{\text{eq}}^2 = \psi$ and thus we can eliminate the unknown function ψ ,

$$\frac{dn}{dt} = -3Hn - \langle \sigma_{\text{ann}} v \rangle (n^2 - n_{\text{eq}}^2). \quad (8.5)$$

This equation together with the initial condition $n \approx n_{\text{eq}}$ for $T \rightarrow \infty$ determines $n(t)$ for a given annihilation cross section σ_{ann} . The evolution of n_X (divided by the entropy density $s \propto 1/R^3$ to scale out the trivial effect of expansion) is shown schematically in Fig. 8.3: As the universe expands and cools down, n_X decreases at least as R^{-3} . Therefore, the annihilation rate $\propto n^2$ quenches and the abundance “freezes-out:” The reaction rates are no longer sufficient to keep the particle in equilibrium and the ratio n_X/s stays constant.

Numerically, one obtains for the relative abundance $\Omega_X = \rho_X/\rho_{\text{cr}}$ of CDM

$$\Omega_X h^2 = \frac{m_X n_X}{\rho_{\text{cr}}} \approx \frac{2 \times 10^{-28} \text{cm}^3/\text{s}}{\langle \sigma_{\text{ann}} v \rangle} x_f, \quad (8.6)$$

where x_f is the ratio of the mass and the freeze-out temperature, $x_f = M/T_f$. Thus the abundance Ω_X is inverse proportionally to the thermally averaged annihilation cross section $\langle\sigma v_{\text{ann}}\rangle$, since a more strongly interacting particle stays longer in equilibrium. The abundance depends only logarithmically on the mass m via the freeze-out temperature x_f . Typical values of x_f found numerically are $x_f \sim 20$. From the observed value $\Omega_{\text{CDM}} \approx 0.20$ one obtains the annihilation cross section in the early universe—that controls also the annihilation rate important for indirect searches today. The size of the cross section corresponds roughly to weak interactions and has led to the paradigm of “WIMPs”, weakly interacting massive dark matter.

Unitarity bounds each partial-wave l of the thermally averaged annihilation cross section as $\langle\sigma_{\text{ann}}v\rangle^{(l)} \leq \text{const.}/(vm^2)$. Requiring $\Omega < 0.3$ leads to $m < (20\text{--}50)$ TeV. This bounds the mass of any stable particle that was once in thermal equilibrium.

8.2.2 SHDM as inflationary relic

The energy density of non-relativistic particles decreases only as $\rho_X \propto 1/R^3$, while the one of radiation decreases as $\rho \propto 1/R^4$. Therefore particles that never came in chemical equilibrium with radiation should be created only in tiny amounts in the early universe. Already the production by gravitational interactions at the end of inflation is sufficient to ensure an abundance $\Omega_X \sim 1$ for stable particles with masses $m_X \sim 10^{13}$ GeV.

As an illustration, we consider the Klein-Gordon equation for the field modes ϕ_k of a scalar field in the Friedman-Robertson-Walker metric,

$$\ddot{\phi}_k(\eta) + m_{\text{eff}}^2(\eta)\phi_k(\eta) = 0, \quad (8.7)$$

where the effective mass depends on an unknown parameter ξ and is

$$m_{\text{eff}}^2(\eta) = k^2 + M_X^2 R^2 + (6\xi - 1)\frac{\ddot{R}}{R}. \quad (8.8)$$

Since m_{eff} is time dependent, vacuum fluctuations will be transformed into real particles. Thus, the expansion of the Universe leads to particle production.

The predicted abundance of X particles today from inflationary cosmology is

$$\Omega_X h^2 \sim \left(\frac{m_X}{10^{11} \text{ GeV}}\right)^2 \frac{T_{RH}}{10^9 \text{ GeV}}, \quad (8.9)$$

where T_{RH} is the temperature at reheating. Since the production is gravitational, the result is model-dependent only through the dependence on cosmological parameters like the value of Hubble parameter at the end of inflation and the reheating temperature T_{RH} .

8.3 Indirect detection of dark matter

8.3.1 Dark matter in the Galactic halo

The average density of DM in the Galaxy is strongly increased compared to the extragalactic space, $n_{\text{MW}}/n_{\text{ex}} \sim 10^5$. Therefore the annihilation rate of DM can become again appreciable inside the Milky Way, and in particular, in objects where DM is strongly accumulated.

DM distribution and clumps Typical results from N -body simulations are for the smooth DM mass density profile ρ_{sm}

$$\rho_{\text{sm}}(r) = \rho_{\odot} \left(\frac{r_{\odot}}{r} \right) \left(\frac{r_{\odot} + a}{r + a} \right)^2, \quad (8.10)$$

with $\rho_{\odot} = 0.3 \text{ GeV/cm}^3$ as the dark matter density at the solar distance from the Galactic center, and $a \sim 25 \text{ kpc}$ as the characteristic scale where the slope changes from r^{-3} to r^{-1} (“Navarro-Frenk-White profile”). At small radii $r \lesssim 1 \text{ kpc}$, the missing resolution of N -body simulations, the influence of baryonic matter and of the galactic SMBH make a reliable estimate of the DM density difficult.

According to the model of hierarchical structure formation, the first objects to form were the smallest structures. For the case of WIMPs, 10^{15} Earth-mass DM halos about as large as the Solar System might be in the Milky Way. An important contribution to the total annihilation signal can be given by small clumps that have a denser core and may be at small distance.

Photons, neutrinos and antiprotons from DM annihilation in the halo The secondaries of DM annihilations will be the stable particle of the standard model, i.e. photons, neutrinos, electrons and protons. For the latter two, only the anti-particles may provide some useful information.

The differential flux of the final state i at the Earth from DM annihilations is

$$I_{\text{sm}}(E, \psi) = \frac{dN_i}{dE} \frac{\langle \sigma v \rangle}{2 m_X^2} \int_{\text{l.o.s.}} ds \frac{\rho_{\text{sm}}^2[r(s, \psi)]}{4\pi}, \quad (8.11)$$

where $r(s, \psi) = (r_{\odot}^2 + s^2 - 2 r_{\odot} s \cos \psi)^{1/2}$, ψ is the angle between the direction in the sky and the galactic center (GC), $r_{\odot} \approx 8.0 \text{ kpc}$ is the solar distance from the GC, and s the distance from the Sun along the line-of-sight (l.o.s.). In terms of galactic latitude b and longitude l , one has $\cos \psi = \cos b \cos l$. The energy spectrum dN_i/dE can be calculated only within a specific model for the DM particle.

SHDM as UHECR source The original motivation to introduce SHDM was the “AGASA excess”, i.e. a surprisingly large number of cosmic ray events with energy $\gtrsim 10^{20} \text{ eV}$ and thus above the GZK cutoff. Since SHDM behaves by definition as CDM, its abundance in the galactic halo is strongly enhanced. As a result the cosmic flux is dominated by the halo component and the GZK cutoff is absent in this model.

The hadronization spectra of superheavy particles can be reliably calculated using standard QCD methods. The predicted spectrum in the SHDM model, $dN/dE \propto E^{-1.9}$, cannot fit the observed UHECR spectrum at energies $E \leq (6-8) \times 10^{19} \text{ eV}$. Thus mainly events at $E \geq (6-8) \times 10^{19} \text{ eV}$, and most notably any excess at energies beyond the GZK cutoff, could be produced by SHDM decays. As for all hadronization processes, the main component of the UHE flux are neutrinos and photons from pion decay. As additional signature, one expects a Galactic anisotropy, because the Sun is not in the center of the Galaxy. The degree of this anisotropy depends on how strong the CDM is concentrated near the Galactic center – a question under debate. First results from the PAO find neither the predicted Galactic anisotropy nor the dominance of photon primaries at the highest energies. If confirmed, SHDM can play only a sub-dominant role as source of UHECRs.

8.3.2 Neutrinos from dark matter annihilations in the Sun and the Earth

Dark matter particles X scatter on matter in the Sun or Earth, lose energy, and may become gravitationally bound. They continue to scatter, gaining or losing energy. If energy losses dominate, they sink down to the center where they eventually annihilate. The directed signal of high energy neutrino would provide a rather clear evidence of DM. In the following, we illustrate the basic steps in the calculation of the resulting neutrino flux, following rather closely Ref. [30].

The total number N_X of dark matter particles in a celestial body is determined by three processes: The capture rate R_C , the evaporation rate R_E , and the annihilation rate R_A ,

$$\dot{N}_X = R_C - R_E N_X - R_A N_X^2 = R_C - \Gamma_E - \Gamma_A. \quad (8.12)$$

If the DM particles are self-conjugated, $X = \bar{X}$, each annihilation reduces their number by two and thus one should replace $R_A N_X^2$ by $2R_A N_X^2$. The evaporation rate takes into account that an already captured dark matter particle might be “kicked out” in a scattering process and is only important for particles not much heavier than nucleons, say $m_X \lesssim \text{few GeV}$. Therefore we will set $R_E = 0$ and obtain as solution of Eq. (8.12)

$$N_X(t) = N_{\text{eq}} \tanh(t/\tau) \quad (8.13)$$

with $\tau = (R_C R_A)^{-1/2}$ as time-scale to reach the equilibrium number $N_{\text{eq}} = (R_C/R_A)^{1/2}$.

We estimate first the capture rate R_C of WIMPs, using where needed the numerical values appropriate for the Sun: The total number of interactions is proportional to the number N_i of scatters of type i in the celestial body, to the elastic cross section σ_{iX} , the relative velocity v_{rel} and the density of WIMPs n_X : Hence R_C should be of the form $R_C \propto n_X \sum_i N_i \sigma_{iX} v_{\text{rel}}$. Additionally, a factor $f = f(v_{\text{esc}}, v_{\text{rel}})$ should count if the scattering was successful, i.e. if the WIMP velocity after the scattering is smaller than the escape velocity v_{esc} from the Sun. The function f should be dimensionless, increase for increasing v_{esc} and can depend only on the square of the velocities. Hence $f = f(v_{\text{esc}}^2/v_{\text{rel}}^2)$, and a more careful analysis shows that indeed $f \propto v_{\text{esc}}^2/v_{\text{rel}}^2$. Combining all factors, the capture rate follows as

$$R_C = A n_X \frac{v_{\text{esc}}^2}{v_{\text{rel}}} \sum_i N_i \sigma_{iX} \quad (8.14)$$

with $A \approx 2$ for the Sun. To obtain a numerical estimate, we neglect helium and metals and set $N = M_{\odot}/m_H$. Using the rotation velocity of the Sun around the Galactic center as relative velocity $v_{\text{rel}} \approx 220 \text{ km/h}$, $v_{\text{esc}} = (GM_{\odot}/R_{\odot})^{1/2} \approx 617 \text{ km/s}$ and $n_X = \rho_{\text{loc}}/m_X$ with $\rho_{\text{loc}} \approx 0.3 \text{ GeV/cm}^3$, it follows

$$R_C \approx 10^{21} \text{ s}^{-1} \left(\frac{\sigma_{iX}}{10^{-42} \text{ cm}^2} \right) \left(\frac{100 \text{ GeV}}{m_X} \right). \quad (8.15)$$

Next we estimate the annihilation rate Γ_A . Generically, the assumption that the WIMP is a thermal relic fixes also the annihilation cross section at present to $\langle \sigma_{\text{ann}} v \rangle \sim 3 \times 10^{-26} \text{ cm}^3/\text{s}$. (This could be avoided if s-wave annihilation is suppressed by symmetry reasons.) Since the captured WIMPs orbit many times in-between interactions, they can be characterized by a global temperature T and their density follows a barometric formula,

$$n_X(r) = n_0 \exp(-m_X \phi(r)/T) \quad (8.16)$$

determined by the local gravitational potential $\phi(r)$. Hence

$$\Gamma_A = \langle \sigma_{\text{ann}} v \rangle 4\pi \int dr r^2 n_X^2(r). \quad (8.17)$$

Determining first $R_A = \Gamma_A/N_X^2$, we see that this rate is fixed by $\langle \sigma_{\text{ann}} v \rangle$ and the ratio V_2/V_1^2 of “effective volumes” defined as

$$V_\alpha = 4\pi \int_0^{R_\odot} dr r^2 \exp(-\alpha m_X \phi(r)/T). \quad (8.18)$$

To obtain a numerical estimate, we use that WIMPs for $m_X \gg m_H$ are concentrated in the center of the Sun. Thus we approximate the density by $\rho(r) \approx \rho(0) \approx 150 \text{ g/cm}^3$, set T equal to the central temperature of the Sun, $T = T_c \approx 1.4 \times 10^7 \text{ K}$, and use $R_\odot \rightarrow \infty$. Then the integrals (8.18) can be performed and one obtains

$$V_\alpha = 6.5 \times 10^{28} \text{ cm}^3 \left(\frac{100 \text{ GeV}}{\alpha m_X} \right)^{3/2} \quad (8.19)$$

and thus

$$R_A = \langle \sigma_{\text{ann}} v \rangle \frac{V_2}{V_1^2} = 6.5 \times 10^{28} \left(\frac{100 \text{ GeV}}{m_X} \right)^{3/2}. \quad (8.20)$$

Now we can determine the equilibration time as $\tau = (R_C R_A)^{-1/2} \approx 1.4 \times 10^{16} \text{ s}$. Since τ is much smaller than the age of the Sun, we can use $\Gamma_A = R_C$. Denoting with f_ν the number of neutrinos produced per annihilation, we obtain as our final result for the neutrino flux ϕ_ν from WIMP annihilations in the Sun

$$\phi = \frac{f_\nu R_C}{4\pi d^2} \sim 5 \times 10^{-8} \text{ cm}^{-2} \text{ s}^{-1} \text{ sr}^{-1} \quad (8.21)$$

at the Earth distance $d = 1 \text{ AU}$. Comparing this flux with expected neutrino intensities and the sensitivity of neutrino telescopes discussed in Sec. 5.5 makes it clear that the detection of WIMP annihilations is as challenging as the one of astrophysical neutrinos. The chances for success depend strongly on the WIMP mass and its annihilation spectrum. Only if the energy of the neutrinos is sufficiently high, $E_\nu \gtrsim 100 \text{ GeV}$, the direction of the produced muon provides a reasonable signature.

8.4 Summary of possible and suggested signals for DM

The different annihilation channels and the DM distribution offers several different possible signals to detect DM annihilations:

- All particles from DM annihilations in the Sun or the Earth are absorbed except neutrinos. Apart from a small flux of neutrinos produced by cosmic ray interactions in the solar atmosphere, no other neutrinos with energy $E \gtrsim \text{GeV}$ are expected from the Sun. The direction provides however only for $E_\nu \gtrsim 100 \text{ GeV}$ a reasonable signature.
- Cold DM has small velocities and thus $XX \rightarrow 2\gamma$ produces a sharp photon line at $E_\gamma = m_X$. This is a smoking-gun for DM, but since the DM particle is most likely electrically neutral, the lowest order contributions to these processes are box diagrams, and the branching ratio is therefore very small.

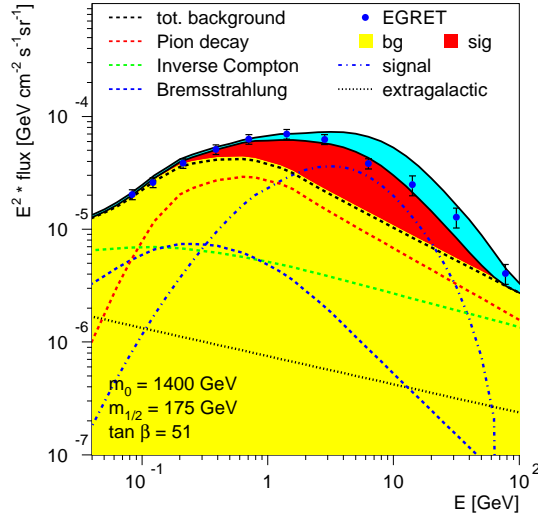


Figure 8.4: EGRET data on diffuse photon background together photons expected from CR interactions (yellow) and a putative DM signal (red) according Ref. [31].

- The main production channel for photons are decays of neutral pions. The main problem here is to separate a potential DM contribution from diffuse astrophysical Galactic and extragalactic backgrounds, cf. Fig. 8.4. More promising might be to look at nearby dwarf galaxies that have with a larger DM fraction.
- Antiprotons could become visible below ~ 1 GeV, but without any specific signatures. Thus the identification of DM as source of these antiprotons requires again a precise modeling of antiproton flux produced by cosmic rays.

Various astrophysical observations have been suggested as signals for DM annihilations:

- The Integral satellite sees a strong positron annihilation line from the Galactic bulge. An explanation by DM annihilations into electron-positron pairs, $\bar{X}X \rightarrow e^+e^-$, requires that the electron-positron pair gets only little kinetic energy. Hence the DM particle should be very light, $m_e < m_X \lesssim 10\text{MeV}$ – which is not excluded but difficult to achieve.
- The “EGRET excess”, i.e. the red region in Fig. 8.4, is a possible surplus of diffuse gamma-rays compared to the predictions in the simplest models for the propagation of cosmic rays. This potential excess has been explained both by DM annihilations in the Milky Way and as the sum of DM annihilation in other galaxies.
- The “WMAP haze”, a potential excess of synchrotron radiation from the Galactic center in the WMAP data has been explained as synchrotron radiation of electron produced in DM annihilations.
- HESS, an atmospheric Cherenkov telescope, has observed TeV γ -rays from the Galactic center. The flux extends however power-law like up to the sensitivity limit (~ 30 TeV) and is thus difficult to combine with the upper limit on M for a thermal relic.

For references to the original literature and a brief critical review see Ref. [32].

Epilogue

Congratulation to the readers who worked through these notes until the end. Certainly many questions have been left unanswered and some new ones have popped up. Still I hope that these notes could provide a first introduction into high energy cosmic ray physics. For further studies I recommend the following two excellent references,

- [E1] V. S. Berezinsky, S. V. Bulanov, V. A. Dogiel, V. L. Ginzburg, V. S. Ptuskin, *Astrophysics of Cosmic Rays* (North-Holland, Amsterdam 1990),
- [E2] T. K. Gaisser, *Cosmic Rays and Particle Physics* (Cambridge University Press, Cambridge 1990).

As the titles indicate, the focus of the first book is on astrophysical aspects of cosmic rays, while the second discusses additionally the interactions of cosmic rays in the atmosphere and the formation of extensive air showers. The presentation of several topics I have given was heavily influenced by these books. I omitted generally references to the original literature, apart from references to the sources of the reproduced figures, and refer also in this respect to the books of Berezinsky *et al.* and Gaisser. Additionally, the following review articles may be helpful:

1. V. Berezinsky, “Ultra high energy neutrino astronomy,” Nucl. Phys. Proc. Suppl. **151**, 260 (2006) [arXiv:astro-ph/0505220].
2. P. Lipari, “Perspectives of high energy neutrino astronomy,” Nucl. Instrum. Meth. A **567**, 405 (2006) [arXiv:astro-ph/0605535].
3. V. Berezinsky, “Transition from galactic to extragalactic cosmic rays,” to appear in the proceedings of 30th ICRC 2007, arXiv:0710.2750 [astro-ph].
4. M. Kachelrieß, “Status of particle physics solutions to the UHECR puzzle,” Comptes Rendus Physique **5**, 441 (2004) [arXiv:hep-ph/0406174].
5. G. Jungman, M. Kamionkowski and K. Griest, “Supersymmetric dark matter,” Phys. Rept. **267**, 195 (1996) [arXiv:hep-ph/9506380].

It is a pleasure to thank all my collaborators in the field of cosmic ray physics, but in particular Roberto Aloisio, Venya Berezinsky, Sergey Ostapchenko, Dima Semikoz, Pasquale Serpico, and Ricard Tomàs, as well as Günter Sigl for many illuminating discussions. I am grateful to Sergey Ostapchenko and Pasquale Serpico for reading (parts of) the manuscript and pointing out several errors and misunderstandings contained in the text.

Last but not least, I would like to thank Kimmo Kainulainen for inviting me to lecture at the Jyväskylä Summer School and for the excellent working conditions provided there.

Bibliography

- [1] E. S. Seo *et al.*, “Measurement of cosmic-ray proton and helium spectra during the 1987 solar minimum,” *Astrophys. J.* **378**, 763 (1991); M. Nagano *et al.*, “Energy spectrum of primary cosmic rays between $10^{14.5}$ and 10^{18} eV,” *J. Phys.* **G10**, 1295 (1984); M. Nagano *et al.*, “Energy spectrum of primary cosmic rays above 10^{17} eV determined from extensive air shower experiments at Akeno,” *J. Phys.* **G18**, 423 (1992); N. L. Grigorov *et al.*, “Energy spectrum of primary cosmic rays in the $10^{11} - 10^{15}$ eV according to the data of Proton-4 measurements,” *Proceedings 12th ICRC*, **1**, 1760 (1971).
- [2] V. Hess, “Über die Beobachtung der durchdringenden Strahlung bei sieben Freiballonfahrten,” *Phys. Z.* **13**, 1084 (1912).
- [3] P. Desgrolard, M. Giffon, E. Martynov and E. Predazzi, “Exchange-degenerate Regge trajectories: A fresh look from resonance and forward scattering regions,” *Eur. Phys. J. C* **18**, 555 (2001) [arXiv:hep-ph/0006244].
- [4] W.-M. Yao *et al.*, *J. Phys.* **G 33**, 1 (2006).
- [5] M. H. Israel *et al.* [ACE collaboration], “Isotopic Composition of Cosmic Rays: Results from the Cosmic Ray Isotope Spectrometer on the ACE Spacecraft,” *Nucl. Phys.* **A758**, 201 (2005).
- [6] M. E. Wiedenbeck *et al.* [ACE collaboration], “The level of solar modulation of Galactic cosmic rays from 1997 to 2005 as derived from ACE measurements of elemental energy spectra,” *Proc. “19th International Cosmic Ray Conference”, Pune, India, 2005*, **2**, p. 277 (2005).
- [7] T. Antoni *et al.* [The KASCADE Collaboration], “Large scale cosmic-ray anisotropy with KASCADE,” *Astrophys. J.* **604**, 687 (2004) [arXiv:astro-ph/0312375].
- [8] Figure from <http://hep.bu.edu/~superk/ew-effect.html>.
- [9] K. H. Kampert, “Cosmic rays from the knee to the ankle: Status and prospects,” *Nucl. Phys. Proc. Suppl.* **165**, 294 (2007) [arXiv:astro-ph/0611884].
- [10] V. S. Berezhinsky, S. I. Grigorieva and B. I. Hnatyk, “Extragalactic UHE proton spectrum and prediction for iron-nuclei flux at $10^{*}8$ -GeV to $10^{*}9$ -GeV,” *Astropart. Phys.* **21**, 617 (2004) [arXiv:astro-ph/0403477].
- [11] F. A. Aharonian, W. Hofmann, A. K. Konopelko, and H. J. Völk, “The potential of the ground based arrays of imaging atmospheric Cherenkov telescopes,” *Astropart. Phys.* **6**, 369 (1997).
- [12] R. D. Blandford, “Acceleration of ultrahigh-energy cosmic rays,” *Phys. Scripta* **T85**, 191 (2000) [arXiv:astro-ph/9906026].

-
- [13] P. Blasi, “On the origin of very high energy cosmic rays,” *Mod. Phys. Lett. A* **20**, 3055 (2005) [arXiv:astro-ph/0511235]; M. Ostrowski, “Cosmic ray acceleration at relativistic shocks, shear layers, . . .,” to appear in *New Astron. Rev.*, arXiv:0801.1339 [astro-ph].
- [14] F. A. Aharonian *et al.* [The HESS Collaboration], “High-energy particle acceleration in the shell of a supernova remnant,” *Nature* **432**, 75 (2004) [arXiv:astro-ph/0411533].
- [15] Figure from William Keel, University of Alabama, <http://www.astr.ua.edu/keel/agn/mkn421.html>.
- [16] B. Rossi and K. Greisen, “Cosmic-ray theory,” *Rev. Mod. Phys.* **13**, 240 (1941).
- [17] A. Mücke *et al.*, “Monte Carlo simulations of photohadronic processes in astrophysics,” *Comput. Phys. Commun.* **124**, 290 (2000) [astro-ph/9903478].
- [18] M. Kachelrieß, P. D. Serpico and M. Teshima, “The galactic magnetic field as spectrograph for ultra-high energy cosmic rays,” *Astropart. Phys.* **26**, 378 (2006) [arXiv:astro-ph/0510444].
- [19] M. Kachelrieß and D. V. Semikoz, “Reconciling the ultra-high energy cosmic ray spectrum with Fermi shock acceleration,” *Phys. Lett. B* **634**, 143 (2006) [arXiv:astro-ph/0510188].
- [20] V. Berezhinsky, A. Z. Gazizov and S. I. Grigorieva, “On astrophysical solution to ultra high energy cosmic rays,” *Phys. Rev. D* **74**, 043005 (2006) [arXiv:hep-ph/0204357].
- [21] A. Cuoco *et al.*, “The footprint of large scale cosmic structure on the ultrahigh energy cosmic ray distribution,” *JCAP* **0601**, 009 (2006) [arXiv:astro-ph/0510765].
- [22] M. Kachelrieß and D. V. Semikoz, “Clustering of ultra-high energy cosmic ray arrival directions on medium scales,” *Astropart. Phys.* **26**, 10 (2006) [arXiv:astro-ph/0512498].
- [23] S. Mollerach *et al.* [PAO Collaboration], “Studies of clustering in the arrival directions of cosmic rays detected at the Pierre Auger Observatory above 10 EeV,” to appear in *Proc. “30th International Cosmic Ray Conference”, Mérida, Mexico, 2007*, arXiv:0706.1749 [astro-ph].
- [24] A. Cuoco *et al.*, “Clustering properties of ultrahigh energy cosmic rays and the search for their astrophysical sources,” to appear in the *Astrophys. J.*, arXiv:0709.2712 [astro-ph].
- [25] J. Abraham *et al.* [PAO Collaboration], “Correlation of the highest energy cosmic rays with nearby extragalactic objects,” *Science* **318**, 939 (2007), arXiv:0711.2256 [astro-ph].
- [26] M. Kachelrieß and R. Tomàs, “High energy neutrino yields from astrophysical sources. I: Weakly magnetized sources,” *Phys. Rev. D* **74**, 063009 (2006) [arXiv:astro-ph/0606406].
- [27] K. Mannheim, R. J. Protheroe and J. P. Rachen, “On the cosmic ray bound for models of extragalactic neutrino production,” *Phys. Rev. D* **63**, 023003 (2001) [arXiv:astro-ph/9812398].
- [28] R. Gandhi, C. Quigg, M. H. Reno and I. Sarcevic, “Neutrino interactions at ultrahigh energies,” *Phys. Rev. D* **58**, 093009 (1998) [arXiv:hep-ph/9807264].

- [29] H. J. Drescher, A. Dumitru and M. Strikman, “High-density QCD and cosmic ray air showers,” *Phys. Rev. Lett.* **94**, 231801 (2005) [arXiv:hep-ph/0408073].
- [30] K. Griest and D. Seckel, “Cosmic Asymmetry, Neutrinos and the Sun,” *Nucl. Phys. B* **283**, 681 (1987) [Erratum-*ibid.* B **296**, 1034 (1988)].
- [31] W. de Boer, “Indirect evidence for WIMP annihilation from diffuse galactic gamma rays,” arXiv:astro-ph/0412620.
- [32] D. Hooper, “Indirect Searches For Dark Matter: Signals, Hints and Otherwise,” to appear in the proceedings of SUSY07, arXiv:0710.2062 [hep-ph].